Charles University in Prague

Faculty of Mathematics and Physics

DOCTORAL THESIS

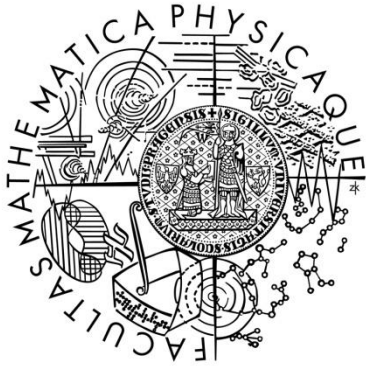

Ahmed Youssef

Critical state response in hard type II superconductors (comparison of transverse and longitudinal geometries)

Department of Low Temperature Physics,
Faculty of Mathematics and Physics,
Charles University

Supervisor of the doctoral thesis: RNDr. Zdeněk Janů, CSc.

Study programme: Physics
Specialization: Physics of Condensed Matter and Materials Research

Prague, 2011

Dedicated to the souls of the martyrs of the revolution of 25 January, who sacrificed themselves for Egypt.

"I do not know what I may appear to the world, but to myself I seem to have been only like a boy playing on the seashore, and diverting myself in now and then finding a smoother pebble or a prettier shell than ordinary, whilst the great ocean of truth lay all undiscovered before me."

Isaac Newton, 1642-1726

Acknowledgments

Without the help and understanding from the people around me, the way to this thesis would be impassable. Using your brain and hands to explore the unknown and to be around smart people in a stimulating environment is indeed privilege.

I am especially grateful to my supervisor Dr. Zdeněk Janů, for introducing the ideas and essential points of this work. I am indebted to his wealth of information, suggestions, directions and support which will be always remembered. He has allowed me much freedom during this work and devoted many hours to its fruitful discussion.

I would like to express my sincere gratitude to Ing. František Soukup, Ing. Rudolf Tichý, Dr. Jan Hadač and Mgr. Zdeněk Švindrych for their generous help.

I would like to thank the faculty of mathematics and physics and staff of the low temperature department, Charles University for their help and support.

Finally, I wish to extend a heartfelt appreciation to all of my family members who were the utmost confidence in my endeavour and I would like to take this opportunity to thank my mother, my wife and my uncle Mr. Saad Youssef.

I declare that I carried out this doctoral thesis independently, and only with the cited sources, literature and other professional sources.

I understand that my work relates to the rights and obligations under the Act No. 121/2000 Coll., the Copyright Act, as amended, in particular the fact that the Charles University in Prague has the right to conclude a license agreement on the use of this work as a school work pursuant to Section 60 paragraph 1 of the Copyright Act.

In *Prague* date *24.8.2011* signature

Ahmed Youssef

Název práce: Odezva kritického stavu v tvrdých supravodičích II. typu (srovnání příčné a podélné geometrie).

Autor: Ahmed Youssef

Katedra / Ústav: Katedra fyziky nízkých teplot, Matematicko-fyzikální fakulta, Univerzita Karlova v Praze.

Vedoucí doktorské práce: RNDr. Zdeněk Janů, CSc., Katedra fyziky nízkých teplot.

Abstrakt: V této práci jsem studoval Beanův model kritického stavu (BCMS) v tvrdých supravodičích II typu. Cílem práce bylo zjistit kritickou proudovou hustotu J_c a její teplotní závislost pomocí analýzy teplotní závislosti magnetické susceptibility χ_{ac} naměřené bezkontaktní metodou pomocí skvidového magnetometru. Srovnával jsem výsledky BCSM pro čtyři geometrie vzorku: desku a dlouhý válec v podélném poli a disk a pásek v příčném poli. Tato práce se soustředí na χ_{ac} tenkých supravodivých filmů (disk a pásek). Měřil jsem magnetickou odezvu tenkých Nb filmů a drátů vysokoteplotního supravodiče $YBa_2Cu_3O_x$ v příčném poli jako funkci teploty, dále objemový vzorek NEG-123 v podélném poli. Prezentuji zde metodu propojení modelu a experimentální susceptibility. Dobrý souhlas naměřené susceptibility s modelem 2D disku umožňuje bezkontaktně určit kritickou proudovou hustotu a její teplotní závislost. Harmonická analýza teplotní závislosti nelineární χ_{ac} výborně souhlasí se susceptibilitou vypočtenou na základě 2D modelu disku.

Klíčová slova: Střídavá susceptibilita, kritický stav v supravodičích II. typu, kritická proudová hustota, vyšší harmonické, tenký film.

Title: Critical state response in hard type II superconductors (comparison of transverse and longitudinal geometries)

Author: Ahmed Youssef

Department / Institute: Department of Low Temperature Physics, Faculty of Mathematics and Physics, Charles University

Supervisor of the doctoral thesis: RNDr. Zdeněk Janů, CSc., Department of Low Temperature Physics, Faculty of Mathematics And Physics, Charles University.

Abstract: In this work we have studied the Bean critical state model (BCSM) in hard type II superconductors. The study has been aimed towards the determination of the critical current density J_c and its temperature dependence using analyses of a temperature dependence of a magnetic susceptibility χ_{ac} measured by a contactless method using SQUID magnetometer. We have compared the predictions of the BCSM for the four geometries: slab in a parallel field, long cylinder in an axial field, and disk and strip in a transverse field. The main interest of the present study is the χ_{ac} of the superconducting thin films (disk and strip). We have measured the magnetic response of Nb thin films and second-generation high temperature superconductor $YBa_2Cu_3O_x$ wire in a perpendicular AC field as a function of temperature as well as bulk NEG-123 sample in parallel magnetic field. We have presented a method of linking model and experimental susceptibility. The good agreement of experimental susceptibility with model of 2D disk allows noncontact estimation of the critical depinning current density and its temperature dependence. Harmonic analysis of the temperature dependence of the nonlinear χ_{ac} gives excellent agreement with the susceptibility calculated on basis of 2D BCSM to disk.

Keywords: AC susceptibility, critical state in type II superconductors, critical current density, harmonics, thin film.

Contents

List of symbols

Λ	2D screening length
B_0	amplitude of the applied magnetic field
ω	angular frequency
$\mathbf{B_a}$	applied magnetic field
A	area of the sample
k_B	Boltzmann constant
B_d	characteristic field for disk and strip geometry
q_s	charge of Cooper pair
e	charge of electron
μ	chemical potential
ξ	coherence length
L_c	correlation length
I_c	critical current
J_c	critical depinning current density
T_c	critical temperature
$\mathbf{J}$	current density
n_s	density of superconducting electrons
J_0	depairing critical current density
$\mathbf{E}$	electric field
ρ_F	flux flow resistivity
F_S *and* F_n	free energy density in a superconducting and normal state.
f	frequency
B_p	full penetration field in cylinder and slab geometries
f_0	fundamental frequency
$\alpha(T)$ *and* $\beta(T)$	Ginzburg-Landau coefficients
κ	Ginzburg-Landau parameter
a	half width of strip and radius of disk
χ''_{1p}	height of the peak in the imaginary part of the susceptibility
B_{c2}	higher critical field
B_{irr}	irreversibility field
L	length of the sample
$\mathbf{F}_\mathrm{L}$	Lorentz force
$\Gamma(h)$	loss factor
B_{c1}	lower critical field
$\mathbf{H}$	magnetic field strength
$\mathbf{B}$	magnetic flux density

$\mathbf{m}$	magnetic moment
χ	magnetic susceptibility
$\mathbf{A}$	magnetic vector potential
$\mathbf{M}$	Magnetization
m_s	mass of Cooper pair
m_e	mass of electron
ψ	order parameter
J_k	parameter associated with the critical current density
B_k	parameter associated with the internal field
λ	penetration depth of magnetic field
μ_0	permittivity of vacuum
φ	phase of the order parameter
$\mathbf{F}_\mathrm{p}$	pinning force
U	pinning potential barrier
h	Planck's constant
$f_F(E)$ and $f_B(E)$	probabilities of occupation of an energy level E, for fermions and bosons respectively.
Φ_0	quantum of a magnetic flux
χ_5' and χ_5''	real and imaginary part of the fifth harmonic of the magnetic susceptibility
χ_1' and χ_1''	real and imaginary part of the fundamental magnetic susceptibility
χ_3' and χ_3''	real and imaginary part of the third harmonic of the magnetic susceptibility
h_0	reduced field
ρ_n	resistivity of the normal state
B_d	special critical field for the strip and disk geometry
B_{c3}	surface nucleation field
T	temperature
T_p	temperature corresponds to the maximum height of the peak in the imaginary part of the fundamental susceptibility
B_c	thermodynamic critical field
d	thickness of the sample
t	time
η	viscous drag coefficient
$\boldsymbol{F}_v$	viscous drag force
V	voltage
V	volume of the sample
$\boldsymbol{v}_L$	vortex drift velocity
J_{c0}	zero-temperature critical current density

1. Introduction

1.1. Motivation

This thesis was devoted to study the Bean critical state model (BCSM) in hard type II superconductors. Fundamentally, this study was aimed towards the determination of the critical current density and its temperature dependence using analyses of a temperature dependence of a magnetic susceptibility χ_{ac} of samples and hence determine the critical current density by contactless method using SQUID magnetometer. Contactless measurements are based on measuring the magnetic flux of the current induced in the sample by applied magnetic field. On the other hand contact measurements of electronic transport commonly require the measurement of a voltage and current. Many factors contribute to the accuracy of the final measurement, including the voltage and current measurement accuracies and noise. Testing of low resistance samples requires higher currents and very sensitive voltage measuring instruments. When such a high current produces local field and Joule heating the pulse measurements are preferred, which may make an interpretation more difficult. The measuring system must minimize voltage noise, drifts, and thermal EMFs to obtain accurate low-voltage measurements. In addition attachment of the electrical leads may introduce impurities or strains into the sample. The contacts must be of high quality and low resistivity. Also, one should avoid local modification of the material such as diffusion of solder, temperature degradation, etc.

The thesis compared the predictions of the BCSM for the four geometries: the slab in a parallel field, the long cylinder in an axial field, and disk and strip in transverse field. The main interest of the present study is the χ_{ac} of the superconducting thin film (disk and strip) due to its important applications.

This thesis is organized as follows: Chapter 2 is devoted to study the general basic concepts which are important for understanding the critical state in superconductors, Chapter 3 focuses on the study of the Bean critical state model, Chapter 4 is dedicated to the experimental work and model calculations and Chapter 5 demonstrates the experimental results and the discussions.

1.2. Superconducting state

When an electric current flows in a normal conductor, there is some resistance to the motion of electrons through the conductor. It is necessary to apply a voltage to keep the current going on, to replace the energy dissipated by the resistance. However at low temperatures some materials have the ability to conduct electricity without energy dissipation, theses materials are said to be in the superconducting state.

The superconducting state literally means that, charge transport is frictionless. It is an anomalous phenomenon. In some metals, the superconducting state occurs due to the presence of a 0.01% fraction of abnormal (superconducting) electrons, while the other 99.99% free (conduction) electrons remain normal. The correlated behaviour of this abnormal small fraction predominates the rest and the metal loses its resistivity. The presence of the normal conduction electrons is completely masked by the abnormal electrons. The superconducting state is a quantum state occurring in the macroscopic scale.

To understand why superconductivity occurs, it is better to consider quantum statistics. According to the quantum statistics, there are two types of elementary particles: bosons and fermions. Bosons have an integer spin, while fermions possess a half integer spin. Electrons have spin 1/2 (in units of $\hbar = h/2\pi$, where h is the Planck's constant) so they are fermions and follow the Pauli exclusion principle i.e. no two electrons can occupy the same energy state. At the same time, many bosons can occupy the same state. This is the main difference between fermions and bosons. Thus, they belong to different quantum statistics. Fermions follow Fermi-Dirac distribution function, Eq. (1), while bosons obey Bose-Einstein distribution function Eq. (2).

$$f_F(E) = \frac{1}{\exp\left[(E-\mu)/k_B T\right]+1}, \tag{1}$$

$$f_B(E) = \frac{1}{\exp\left[(E-\mu)/k_B T\right]-1}, \tag{2}$$

where $f_F(E)$ and $f_B(E)$ are the probabilities of occupation of an energy level E, for fermions and bosons, respectively, T is temperature, μ is the chemical potential, and k_B is Boltzmann constant. Below some critical temperature, electrons can form pairs with

opposite spins and momentum. These pairs, called Cooper pairs, are bosons. They appear due to a net attractive force between electrons mediated by an exchange of phonons. In fact, many experimental and theoretical studies of superconductivity are devoted to find an origin of the attractive force between the Cooper pairs constituents. The electron energy in the superconducting state is lower than that in the normal state. The difference in the energy per electron between the two states is the energy gap below the Fermi energy level. The energy gap provides a barrier against the transition of electrons from the superconducting state to the normal state, even when the electrons are scattered by lattice defects, impurities, or thermally oscillating ions and the electric resistivity may not appear.

Superconductivity is by its nature a quantum effect. It originates from quantum coherence in macroscopically large sample, where all electrons carrying the current in a sample of macroscopic size can be described by a single wavefunction. This leads to a number of observable macroscopic quantum effects such as the flux quantization. If a superconducting ring carries a supercurrent, magnetic flux inside the ring can have only values which are integer multiples of a flux quantum Φ_0 [1, 2].

The superconducting state is a state of matter. It is not a property of isolated atoms but is a collective effect determined by the structure of the whole sample. One of the features of superconductivity is that the electrical resistance of a material suddenly drops to zero as the temperature decreases through a transition point, the critical temperature T_c, see Fig. 1. The superconductor is not only a perfect conductor but also a perfectly diamagnetic material which excludes a magnetic field from its interior. This effect is called Meissner effect. The perfect diamagnetism is broken at sufficiently high applied magnetic field. This break down can take place in two ways depending on whether the superconductor is type I or type II. The magnetic field enters to a type I at a specific critical field B_c and the material completely converts to the normal state. In type II, the magnetic field starts to penetrate into the sample in microscopic filaments called vortices at lower critical field B_{c1}, while the sample is converted to the normal state at a higher critical field called B_{c2}. The region between B_{c1} and B_{c2} is called the mixed state.

An important characteristic of a superconductor is the maximum transport current, which can flow without dissipation, i.e. the critical current, I_c. The value of the critical current depends on the sample geometry and quality. According to Silsbee's criterion [3], a superconductor loses its zero resistance when at any point on the surface the total

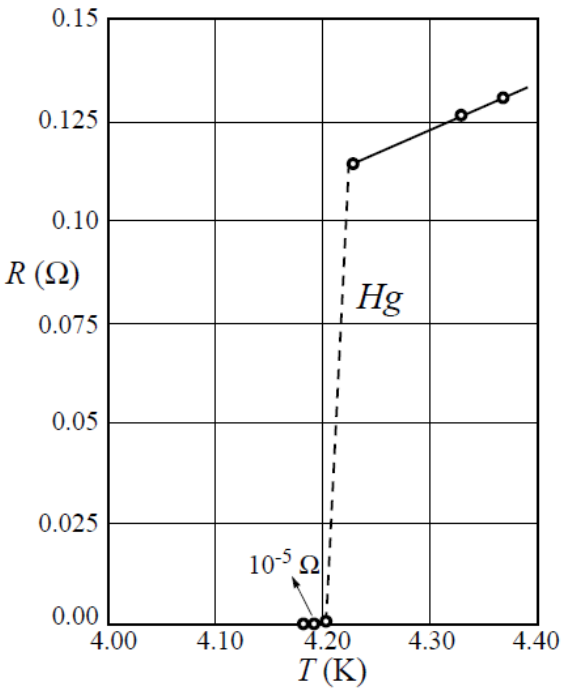

Fig. 1: *The resistance versus temperature curve of mercury shows the vanishing of the electrical resistivity ρ as discovered by Heike Kamerling Onnes in 1911.*

magnetic field strength, due to the transport current and applied magnetic field, exceeds the critical field strength, B_c. The I_c is called the thermodynamic critical current or the depairing current and depends on the external magnetic field and temperature.

Another manifestation of the quantum nature of superconductivity is the Josephson effect [4]. This phenomenon has a large number of applications in microelectronics, the best known examples being *SQUIDs* (superconducting quantum interference devices). Josephson effect predicts the tunnelling of Cooper pairs through a thin insulating barrier (in the order of a few nanometres thick). In a junction composed of two superconductors separated by thin insulating layer, a zero voltage current flow resulting from the tunnelling of Cooper pairs is known as DC Josephson effect. If a nonzero voltage V is maintained across the tunnel barrier, an alternating supercurrent will flow through the barrier in addition to the DC current produced by the tunnelling of normal electrons. The angular frequency of the AC supercurrent is $\omega = 2eV/\hbar$ and $\hbar = h/2\pi$, where h is Plank's constant. This oscillating current is known as the AC Josephson effect.

2. Two types of superconductors

In practical applications, a major use of superconductors is to produce high magnetic fields. Therefore hard superconductors (type II superconductors with a strong flux pinning) are used in most applications since they remain superconducting in much higher magnetic fields than type I superconductors. The Bean critical state model was developed to explain the irreversible magnetic properties of hard superconductors. In this chapter, properties of hard superconductors will be described. In the first part of the chapter, the Ginzburg Landau theory and type I superconductors will be briefly mentioned. In latter part of the chapter we will study the properties of type II superconductors, the vortices, flux pinning, vortex motion and critical current.

2.1. The Ginzburg Landau theory

The phenomenology of superconductivity is based on the Ginzburg Landau (GL) theory [5]. Within this theory Ginzburg and Landau introduced an order parameter ψ to describe the phenomena of superconductivity. In its simplest version, $\psi = |\psi(\mathbf{r})| \exp(i\varphi)$ is a complex order parameter, where φ is the phase of the order parameter. In the superconducting phase, which is the ordered phase, $|\psi| \neq 0$, while for temperatures above T_c, $|\psi| = 0$ in the state of thermodynamic equilibrium. The absolute value of the order parameter is related to the density of superconducting electrons, $n_s/2 = |\psi(\mathbf{r})|^2$.

Based on Landau's theory of second-order phase transition [6], the free energy of the superconducting state can be written as a power series in $|\psi(\mathbf{r})|^2$. Near the critical temperature it is sufficient to retain only the first two terms in this expansion. Furthermore, if a wavefunction $\psi(\mathbf{r})$ is not constant in space, this gives rise to a kinetic energy, and to take this into account, an additional term is added to the free energy, which is proportional to the square of the gradient of $|\psi(\mathbf{r})|^2$. As a result the difference between the free energy densities of superconducting and normal phases is written in the following form

$$F_s - F_n = \alpha(T)\left|\psi(\mathbf{r})\right|^2 + \frac{\beta(T)}{2}\left|\psi(\mathbf{r})\right|^4 + \frac{1}{2m_s}\left|-i\hbar\nabla\psi(\mathbf{r}) - q_s\mathbf{A}(\mathbf{r})\psi(\mathbf{r})\right|^2 + \frac{(\nabla\times\mathbf{A})^2}{2\mu_0}, \quad (3)$$

where F_S and F_n are the values of the free energy density in a superconducting and normal state, respectively, and **A** is a vector potential generating the magnetic flux density, $\mathbf{B} = \nabla \times \mathbf{A}$. m_S and q_S are the mass and charge of Cooper pairs respectively, i.e. $m_S = 2m_e$, and $q_S = 2e$, where m_e and e are the mass and charge of the electron respectively. The GL expansion (3) is valid only near T_c where the order parameter $\psi(\mathbf{r})$ is small enough. The GL coefficients $\alpha(T)$ and $\beta(T)$ are phenomenological parameters.

When the superconductor coexists with the magnetic field, $\psi(\mathbf{r})$ and $\mathbf{A}(\mathbf{r})$ can be determined by minimizing the free energy with respect to the order parameter and vector potential. One arrives to the two GL equations.

$$\frac{1}{4m_e}\left(-i\hbar\nabla - 2e\mathbf{A}\right)^2 \psi(\mathbf{r}) + \alpha(T)\psi(\mathbf{r}) + \beta(T)\left|\psi(\mathbf{r})\right|^2 \psi(\mathbf{r}) = 0, \tag{4}$$

$$\mathbf{J} = \frac{-i\hbar e}{2m_e}\left(\psi^*(\mathbf{r})\nabla\psi(\mathbf{r}) - \psi(\mathbf{r})\nabla\psi^*(\mathbf{r})\right) - \frac{2e^2}{m_e}\left|\psi(\mathbf{r})\right|^2 \mathbf{A}. \tag{5}$$

2.1.1. Coherence length and flux penetration depth

The set of Eqs (4) and (5) permits one to define two fundamental lengths: λ, the penetration depth of magnetic field, and ξ, the coherence length. The electromagnetic properties in the superconductor are determined by these two characteristic lengths. They are related to the spatial variations in the magnetic flux density **B** and the order parameter $\psi(\mathbf{r})$ see Fig. 2. Temperature dependence of the penetration length is

$$\lambda(T) = \lambda(0)\left[1 - (T/T_c)\right]^{-1/2}, \tag{6}$$

where $\lambda(0)$ denotes the penetration length at zero absolute temperature. The magnitude of the penetration depth depends on the material and temperature. On the other hand the coherence length is given by

$$\xi(T) = \xi(0)\left[1 - (T/T_c)\right]^{-1/2}. \tag{7}$$

At $T \to T_c$ both quantities $\lambda(T)$ and $\xi(T)$ approach infinity.

The ratio of these two characteristic lengths is defined by $\kappa = \lambda(T)/\xi(T)$. According to the GL theory, $\lambda(T)$ and $\xi(T)$ have the same temperature dependence, and

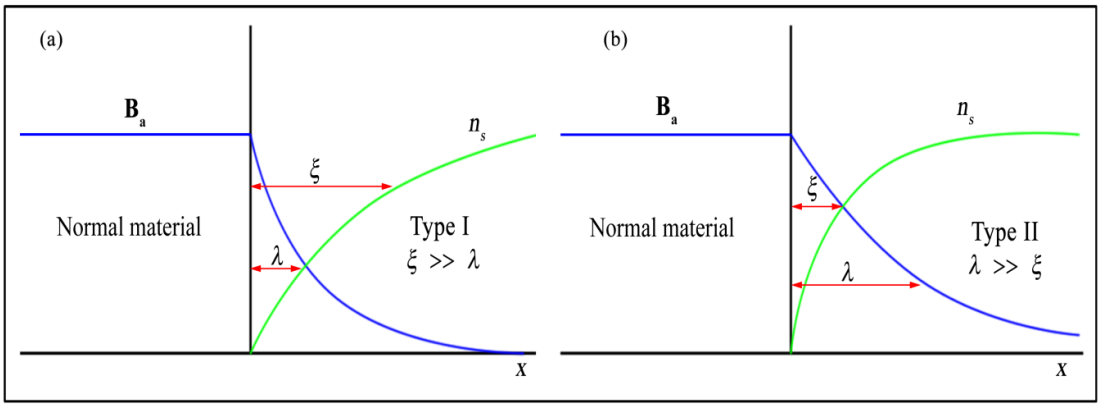

Fig. 2: *The coherence length ξ and penetration depth λ associated with the change in n_s and the magnetic induction* ***B*** *inside the superconductor. (a) Type I superconductor, with $\xi > \lambda$, and (b) Type II superconductor, with $\lambda > \xi$, and $B_a < B_{c1}$, where B_a is the applied magnetic field and B_{c1} is the lower critical field.*

hence κ is independent of temperature. As a matter of fact, κ decreases slightly with increasing temperature. The GL parameter κ plays an important role in a description of the magnetic properties of superconductors. In particular classifies the superconductors into type I and type II.

The GL theory was constructed, in particular, to explain the positive surface energy of the superconductors. Abrikosov has studied this possibility in detail [7]. He demonstrated that GL theory predicts the division of superconductors into two categories according to the magnitude of the GL parameter κ. These categories are referred to as type I and type II superconductors. For type I superconductors $\kappa < 1/\sqrt{2}$ with a positive surface energy associated with a domain wall between normal and superconducting material. This positive surface energy stabilizes a domain pattern in intermediate state. On the other hand, in type II superconductors $\kappa > 1/\sqrt{2}$ that leads to the negative surface energy and a process of subdivision into domains would proceed until it is limited by the coherence length ξ. Abrikosov has shown that the magnetic field starts to penetrate type II superconductors at lower critical field B_{c1} in a regular array of flux tubes (vortices), instead of laminar domains in case of type I, and reaches the applied field B_a at higher critical field B_{c2}, i.e. $B = B_a$. Each vortex carries a quantum of a magnetic flux, $\Phi_0 = h/2e$. Between B_{c1} and B_{c2} the sample is said to be in the mixed state or Shubnikov phase.

2.2. Type I superconductors

Type I superconductors include all superconducting elements except for Nb, V and Tc. Behaviour of a long superconducting rod in an external magnetic field $\mathbf{B_a}$ is demonstrated in Fig. 3. At sufficiently small applied field, $|\mathbf{B_a}| < B_c$, where B_c is the critical magnetic field, the interior of the sample is completely screened by induced shielding currents that flow near a surface and magnetization **M** acts opposite to the applied field $\mathbf{B_a}$. The magnetic flux is completely expelled and the magnetic flux density inside the sample is $\mathbf{B} = \mu_0 (\mathbf{H} + \mathbf{M})$, where **H** is the magnetic field strength. A magnetic susceptibility of a superconductor is $\chi = \mathbf{M}/\mathbf{H} = -1$, which is equal to the ideally diamagnetic material. If the external magnetic field is increased, screening breaks down at the critical magnetic field B_c and a transition to a normal state takes place. The single value $\mathbf{M(B_a)}$ curve demonstrates that the superconducting state is a thermodynamic equilibrium state and the transition from the normal to the superconducting state represents a phase transition. B_c depends on temperature, as is shown in Fig. 4. This figure is in fact the *B*-*T* phase diagram of an ideal superconductor. At $B_a < B_c$, penetration of a magnetic field in superconductor is thermodynamically unfavourable. Thus, a superconductor can be characterized by perfect conductivity and perfect diamagnetism. The dependence of B_c on temperature can be expressed approximately by the empirical relation

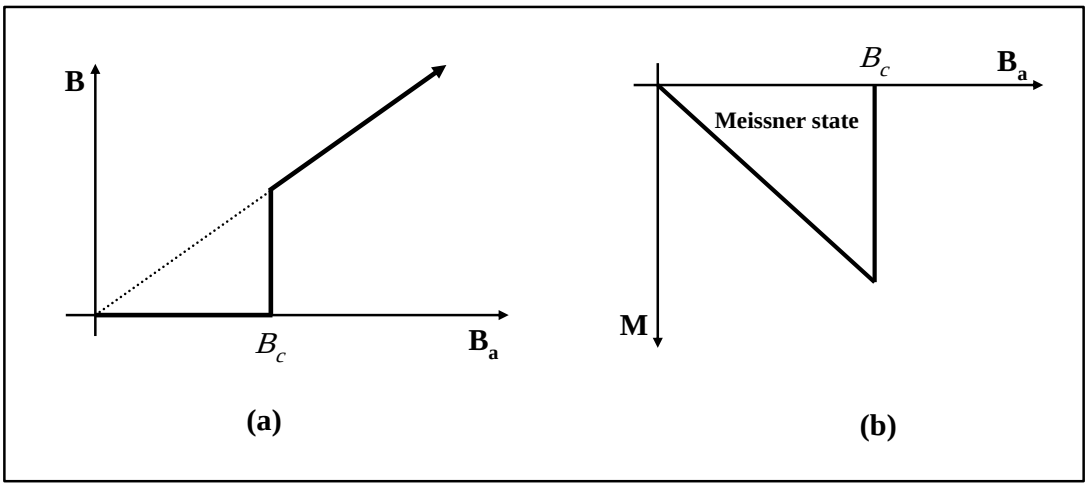

Fig. 3: *(a) Magnetic field **B** inside a type I superconductor, and (b) its magnetization as a function of the applied magnetic field $\mathbf{B_a}$. The material shows a perfect diamagnetism below the critical magnetic field B_c.*

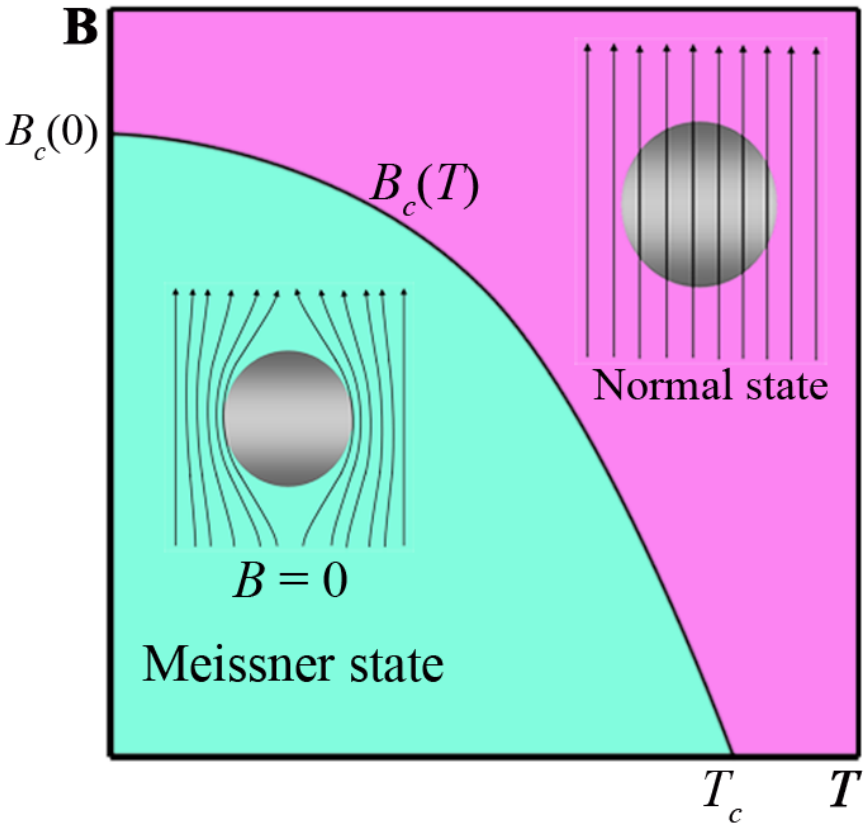

Fig. 4: *Phase diagram of type I superconductors.*

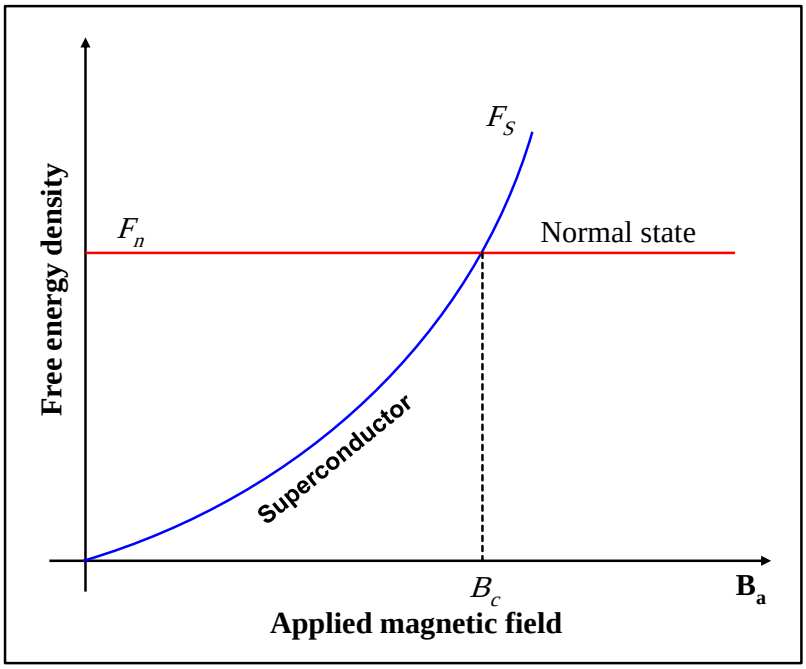

Fig. 5: *The curve of the free energy of a superconducting sample. When the applied magnetic field exceeds B_c it is energetically favourable for the sample to be in the normal state.*

$$B_c(T) = B_c(0)\left(1 - \left(\frac{T}{T_c}\right)^2\right). \quad (8)$$

According to the thermodynamic principle, that the free energy is always minimized at equilibrium, the superconducting state must have the lowest free energy below the critical temperature T_c, while the normal state has the lowest free energy at temperature higher than T_c. The free energy of a sample in the superconducting state is shown in Fig. 5. It is represented by a parabolic curve crossing the free energy line of the sample in the normal state at $B_a = B_c$. The change in the free energy density of a superconducting sample when the magnetic field decreased through B_c is

$$\Delta F = \frac{B_c^2}{2\mu_0}, \quad (9)$$

which means that the superconducting state has a lower energy and is preserved up to B_c, which is called the thermodynamic critical field.

In many real situations the effect of sample geometry causes the flux density to exceed B_c at some part of the sample surface due to a large demagnetization factors. As a result, a flux penetrates into the type I superconductor in a field smaller than B_c. A good example is a thin superconducting film in a perpendicular magnetic field. Therefore some volume fractions of the sample suffer a transition from a superconducting state to a normal state. In this case the sample is said to be in the intermediate state [6, 8].

Type I superconductors have limited practical applications due to the small values of the critical magnetic field B_c and the critical current density J_c.

2.3. Type II superconductors

Type II superconductors are characterized by the GL parameter $\kappa > 1/\sqrt{2}$, i.e. by negative surface energy. Therefore the appearance of normal regions in the interior of a specimen placed in a magnetic field is energetically favourable and the material should split into a fine-scale mixture of superconducting and normal regions, with the arrangement being such as to give the maximum possible boundary area. Such a state is called a mixed state. It was first demonstrated by Shubnikov [9] in 1937. However, it was not understood until the work of Abrikosov [7] twenty years later, who explained

the full consequences of a negative surface energy and the nature of type II superconductors.

The typical *B*-*T* phase diagram for a type II superconductor of a cylindrical sample placed in a parallel magnetic field is shown in Fig. 6. For weak applied fields $B_a < B_{c1}$ there is complete flux expulsion (Meissner phase). At $B_a = B_{c1}$ it becomes energetically favourable for the magnetic flux to penetrate the sample. When $B_a > B_{c1}$ the magnetic flux penetrates the superconductor partially in the form of flux lines (vortices). Complete penetration of a flux takes place at a much higher field $B_{c2} > B_c$ which is called the upper critical field. The curve $B_{c2}(T)$ on the phase diagram is the line of the second-order phase transition between superconducting and normal states. In the field range, $B_{c1} < B_a < B_{c2}$, a superconductor is said to be in a mixed state. In equilibrium conditions the vortices form a regular vortex lattice. The existence of the vortex lattice was first confirmed by a direct experimental observation using a decoration technique by Essman and Träuble [10].

The dependence of internal magnetic flux density **B** and magnetization **M** on an applied magnetic field $\mathbf{B_a}$ in ideal type II superconductors without pinning is shown in Fig. 7.a. The Meissner state exists at low fields $B_a < B_{c1}$, while the mixed state exists in the range between B_{c1} and B_{c2}. There is a second-order phase transition to the mixed state at B_{c1} and to normal state at B_{c2}. The two shaded areas separated by the thermodynamic field, B_c, are equal. It can be defined by the expression

$$\int_{B_{c1}}^{B_c} \left(B_a + \mu_0 M\right) dB_a = \mu_0 \int_{B_c}^{B_{c2}} \left(-M\right) dB_a. \qquad (10)$$

The real magnetization and internal magnetic flux unlike Fig. 7.a are rounded as indicated in Fig. 7.b. Both type I and type II superconductors exhibit a thermodynamic field B_c. The Gibbs free energy between the normal and the superconducting state in type I (Eq.(9)) is given by $B_c^2/2\mu_0.B_{c1}$ and B_{c2} can be expressed in terms of B_c as follows,

$$B_{c1} = \frac{B_c \ln\kappa}{2\sqrt{2}\kappa}$$
$$B_{c2} = 2\sqrt{2}\kappa B_c, \qquad (11)$$
$$\text{where} \quad B_c = \frac{\Phi_0}{2\sqrt{2}\lambda\xi}.$$

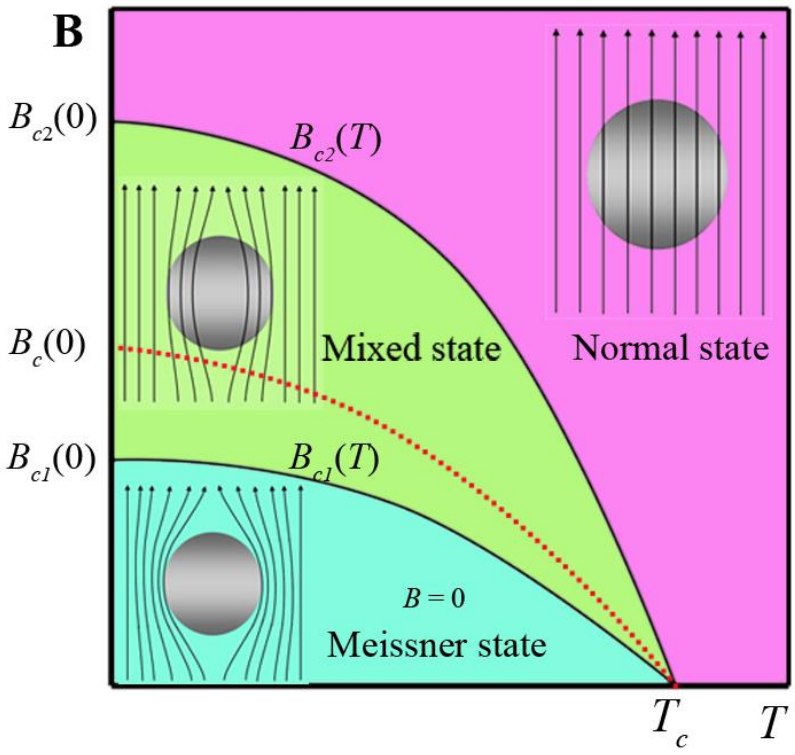

Fig. 6: *The* ***B****–T phase diagram of type II superconductors.*

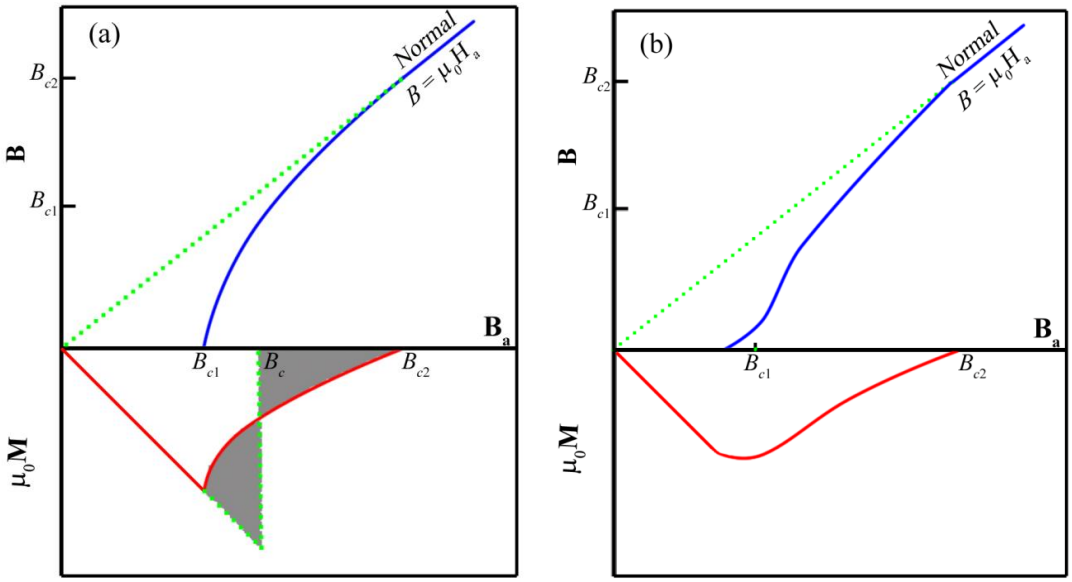

Fig. 7: *Dependence of the magnetic flux* ***B*** *and magnetization* ***M*** *on an applied magnetic field* $\boldsymbol{B_a}$ *for (a) an ideal type II superconductor. The two shaded areas separated by* B_c *are equal. (b) non–ideal type II superconductors. The curves near the lower-critical field are rounded.*

When the applied magnetic field is perpendicular to the surface of the superconductor, the upper critical field is B_{c2}. When it is parallel to the surface, the superconducting state can persist in a thin surface layer of the order of $\xi(T)$. This surface superconductivity exists in an interval $B_{c2} < B_a < B_{c3}$, where the so-called surface nucleation field $B_{c3} = 1.69\, B_{c2}$ [11, 12]. The existence of the surface superconductivity may manifest itself in measuring the resistance between two surface probes, but has minor influence on the magnetization curve of a macroscopic sample. The lower and upper critical fields of type II superconductors have similar temperature dependence. Type II superconductors are preferred in practical applications, due to their relatively high transition temperatures. They also carry large currents and often operate in large magnetic fields.

2.3.1. Vortex state

In a pioneering paper A. Abrikosov [7] predicted that in the mixed state type II superconductors could retain superconductivity in strong magnetic fields by allowing the magnetic flux to penetrate the sample as a periodic arrangement of quantized magnetic flux lines, i.e. flux line lattice (FLL). Within the framework of the Ginzburg Landau theory the structure of an Abrikosov vortex is characterized by two fundamental length scales: the magnetic penetration depth λ and the coherence length ξ, where $\lambda > \xi$. In simple way the vortex can be described as a cylindrical normal core with radius ξ and a superconducting current circulating around it with radius λ. The structure of the Abrikosov vortex is depicted in Fig. 8. A maximum of the magnetic flux density is in the centre of the vortex and at large distance from the core decays roughly exponentially with the penetration depth λ. The order parameter $\psi(r)$ or the Cooper pair density is reduced in a small core region with radius of the order of the coherence length ξ, therefore the vortex core can be represented as a region of normal phase of an area $\sim \xi^2$. The vortex enters and leaves the superconductor at the surface.

Each vortex carries one magnetic flux quantum Φ_0. Vortices exert a Lorentz–like force on each other. The energy associated with the repulsive interaction between vortices decreases as the separation increases. Inside the superconductor, the vortices arrange themselves at distances $\sim \lambda$ from each other, so that in the cross-section, they form a regular triangular or square lattice (Fig. 9). Once formed at $B > B_{c1}$, the flux line lattice (FLL) persists at much higher fields. As the external field increases, the lattice

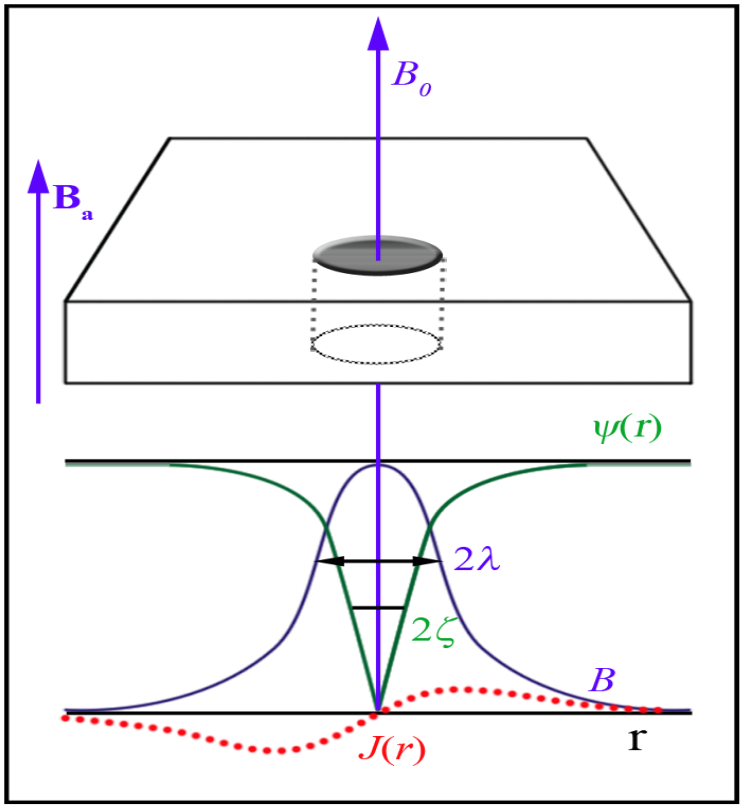

Fig. 8: *Spatial variation of the superconducting current, the magnetic flux density and the magnitude of the order parameter, ψ(r), in isolated vortex. The magnetic flux density decreases from the maximum value at the vortex centre to zero at a distance λ in the superconductor. The order parameter grows from zero to maximum value in the superconductor at a distance ξ.*

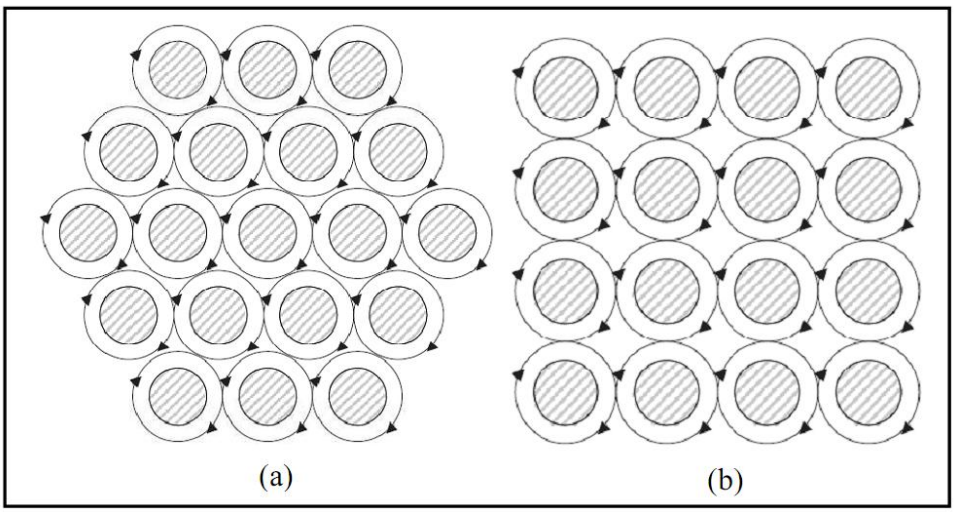

Fig. 9: *Mixed state of a type II superconductor. Superconducting vortices form a regular triangular (hexagonal) (a) or square (b) lattice. Vortex cores (dashed regions) are normal [13].*

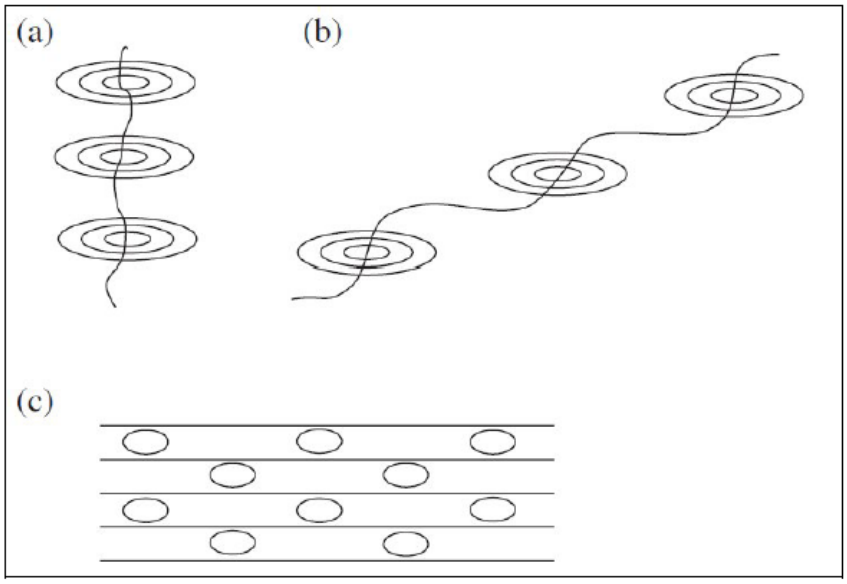

Fig. 10: *(a) Pancake vortices and strings. (b) Vortices of high-T_c cuprates for inclined magnetic field. (c) Josephson vortices [14].*

period steadily decreases and the density of the vortices rises. At a field $B = B_{c2}$, the vortex lattice becomes so dense that the distance between the neighbouring vortices reaches the order of ξ. This means that the normal cores of the vortices come into contact with each other and the order parameter $\psi(r)$ becomes zero over the total volume of the superconductor.

In the absence of a driving current the FLL is in equilibrium. Consequently, each vortex has no net force acting on it because the forces from all the other vortices in the array exactly cancel each other. The presence of external currents and crystal lattice defects is usually referred to as a non–equilibrium situation. The existence of an ideal equilibrium FLL would result in finite resistance at any small value of external current. The drag force by an external current on a vortex is usually referred to as the Lorentz force. It is directed perpendicular to the current flow and results in a vortex motion in this direction. Magnetic flux motion under an external current results in the generation of an electric field. Direct evidence of a voltage generation under flux motion was first given by Giaever in 1965 [15]. This leads to the importance of creating flux pinning in type II superconductors.

In general, there are three important energy scales to discuss the physics of vortex matter. They are (a) interaction between vortices, which favours the ordered state such as FLL, (b) pinning by disorder, which hinders ordering and favours the glassy state, (c)

thermal energy, which also hinders the vortices ordering. For conventional superconductors, (a) is much stronger than the other two cases, and the ordered FLL dominates [14].

In high T_c cuprates, the physics of the vortex matter is changed due to the strong two–dimensionality [16]. The circulating current around the quantized vortex is confined in each CuO_2 plane. These confined vortices are called pancake vortices (Fig. 10.a and Fig. 10.b) [17-19]. Pancake vortices in adjacent layers interact with each other through Josephson coupling [20]. When the magnetic field is applied parallel to the CuO_2 plane we can have coreless Josephson vortices (Fig. 10.c) [21, 22]. The coreless feature leads to ultra high speed motion in the presence of a driving current.

2.3.2. Vortex pinning

The origin of pinning forces is a subject of a detailed research. There are many models and theories which have been proposed to explain it [23-26]. A pinning force $\mathbf{F}_p$ is a short-range force that holds the core of a vortex in a pinning centre and allows the formation of a static vortex density gradient. Usually the pinning centres are related to impurities and the defect structure of a material. In a real superconductor there are always lattice defects such as dislocations, normal precipitates, voids, grain boundaries, etc. It is important that the introduction of pinning defects does not generally lead to a degradation of the critical temperature of the sample. The density of pinning centres can be high with average separations of 10^{-8} m or less [27, 28]. Pinning centres act most efficiently if their spatial extension is of the order of the coherence length. This implies that in the high temperature superconducting materials the pinning sites of atomic size have to be introduced. In hard superconductors, pinning properties play an important role to attain high critical current density J_c where the limit of J is reached when vortices leave their pinning sites and move through the lattice.

There are two regimes of pinning forces: the elementary pinning force at the level of an individual flux line and the bulk pinning force density. The simplest example of elementary pinning interaction between a flux line and crystal lattice is a void which may be present due to the manufacturing process of type II superconductors. When a vortex passes through the void, its energy is lowered by roughly the product of the condensation energy density and the void dimensions hence the vortex prefers to pin to the defect. The bulk pinning force density, which is the pinning force per unit volume of

a pinning centres, is given as a product of the critical current density and the corresponding magnetic flux density. It is rarely possible to sum the local pinning forces directly. The summation usually depends on the strength and distributions of the pinning centres and on the distortions they are able to produce in the vortex lattice [29, 30].

Vortices can undergo thermally activated hopping between pinning centres [31-33]. The Lorentz force needed to depin a single vortex equals to the pinning force. The force per unit length needed to produce this depinning, F_p, has been found to have the temperature dependence

$$F_p(T) = F_p(0)\left[1-(T/T_c)\right]^n, \tag{12}$$

with F_p (0) varying over a wide range from 10^{-12} to 4×10^{-4} N/m and n ranging from 1.5 to 3.5 [34-39].

The existence of pinning in type II superconductor has several consequences [40]:

(i) The $I - V$ curve of a superconductor in a magnetic field is highly nonlinear. At $T = 0$ or for conventional superconductors, one has the electric field, $E = 0$, for $J < J_c$ and $E = \rho_F J$ for $J >> J_c$, where ρ_F is the flux flow resistivity. For J slightly above J_c various concave or convex shapes of $E(J)$ are observed, depending on the type of pinning and on the geometry of the sample.

(ii) The magnetization curve $M(B_a)$ is irreversible and performs a hysteresis loop when the applied magnetic field B_a is cycled.

(iii) In general, the current density in type II superconductors can have three different origins: (a) surface currents (Meissner currents) within the penetration depth λ. (b) a gradient of the flux-line density, or (c) a curvature of the flux lines. Since in simple geometries a deformation of the flux line lattice (FLL) is caused mainly by pinning, it is sometimes said that 'the current flows in regions where the FLL is pinned' [41, 42].

(iv) The flux pinning suppresses the voltage drop induced by vortex motion when $J < J_c$ [43].

(v) Pinned vortices exert a force on the atomic lattice which leads to magneto-mechanical effects [44, 45] and to a change of the velocity and damping of

ultrasound [46-49]. Another mechanical effect of pinning is a strong internal friction [50-52].

A successful theory dealing with random pinning centres is the collective pinning theory [30]. The central idea of this theory is the assumption that the long-range order of the vortex lattice is destroyed by the presence of the disorder (weak pinning centres), leaving a short range order over a correlation length L_c. When L_c is much larger than the coherence length ξ, i.e. $L_c >> \xi$, the pinning is considered to be weak, while it is considered to be strong when $L_c \sim \xi$. Within this theory the critical current density J_c is given by

$$J_c \approx J_0 \left(\frac{\xi}{L_c} \right)^2 , \tag{13}$$

where J_0 is the depairing current density. The dimenensionless ratio J_c/J_0 is a measure of the strength of the pinning force density $\mathbf{F}_p$ [53]. The regime of weak collective pinning ($L_c >> \xi$) is characterized by a large reduction of the critical current density J_c with respect to the depairing current J_0. On the other hand, in the strong pinning regime, when $L_c \sim \xi$, the critical current density J_c achieves its maximum possible value of the order of the depairing current J_0 which is important for practical applications of type II superconductors.

2.3.3. Motion of vortices

Vortices can move as a unit or in large groups (flux bundle) under the action of perturbing forces. When an electric current density **J** flows through type II superconductor in the mixed state, it exerts a Lorentz force density, $\mathbf{F}_L = \mathbf{B} \times \mathbf{J}$, on the flux-line lattice (FLL), which causes the vortices to move with mean velocity $\boldsymbol{v}_L$, see Fig. 11. This vortex drift generates an electric field $\mathbf{E} = \mathbf{B} \times \boldsymbol{v}_L$ where **B** is the flux density in the sample. There are two regimes of flux motion, both of which involve dissipation [54]. The first is flux creep, when the pinning force dominates [55], and the second is flux flow, when the Lorentz force dominates [56].

Moving flux lines dissipate energy by two effects which give approximately equal contributions:

(a) By dipolar eddy currents that surround each moving flux line and have to pass

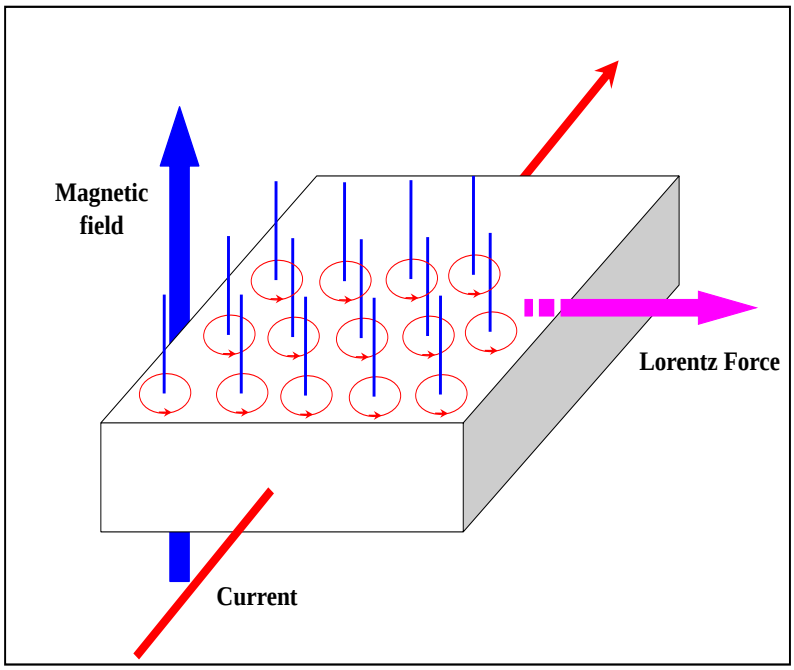

Fig. 11: *A superconductor carries current in a magnetic field. The Lorentz force acts on the flux lines in the direction shown by the arrow.*

through the vortex core, which in the model of Bardeen and Stephen [57] is approximated by a normal conducting cylinder.

(b) By the retarded recovery of the order parameter $\psi(r)$ at places where the vortex core (a region of suppressed $|\psi|$) has passed by [56].

2.3.3.1. Flux flow

When a pin free type II superconductor carries a current in presence of a magnetic field **B** or if the Lorentz force $\mathbf{F}_L$ is so strong that it exceeds the pinning force $\mathbf{F}_p$, the vortices move under the effect of two forces: the Lorentz force $\mathbf{F}_L$ and viscous drag force $\mathbf{F}_v$. The latter force is due to the electric field generated in the region around a vortex core which leads to energy losses in the process of the vortex motion and is usually represented in the form $\mathbf{F}_v = -\eta\, \boldsymbol{v}_L$, where $\boldsymbol{v}_L$ is the vortex velocity and η is the viscous drag coefficient [57].

The most widely accepted theory of flux-flow was worked out by Bardeen and Stephen [57]. They considered a vortex core of radius ξ, which can be treated as if it were in the normal state. When a vortex moves, it generates an electric field in its surroundings. This state of a type II superconductor is called the resistive state. The corresponding resistivity is called the flux flow resistivity ρ_F. The induced resistive

currents in the vortex core create a loss $W = \rho_F J^2$, and thereby a flux-flow resistivity ρ_F ;

$$\rho_F = \frac{\Phi_0 B}{\eta} = \rho_n \frac{B}{B_{c2}}, \tag{14}$$

where ρ_n is the normal state resistivity. The flux flow resistivity ρ_F equals ρ_n when B reaches B_{c2} and goes to zero when B is zero. The factor B/B_{c2} is simply the fraction of the material occupied by the vortex cores, ρ_F is therefore equal to ρ_n times this fraction. The result is the same as if a uniformly distributed current were passed through the material and losses would appear from the fraction of the current which passed through the core regions. Thus the resistivity of type II superconductors in the flux-flow regime in high fields is rather large and usually is much higher than the resistivity of copper at a corresponding temperature.

2.3.3.2. Flux creep

When the DC magnetization of superconducting sample is measured for a long period, it decreases slightly. This indicates that the superconducting current decays with time and it is not persistent current. The decay of the current is a result of the decrease in the gradient of flux lines distribution. Such flux motion, which can be caused by thermal activation is called “flux creep” [58]. Thermally activated flux motion is not a macroscopic and continuous phenomenon like flux flow, but it is a partial and discontinuous one.

Consider a single vortex moving in the direction of the Lorentz force under the influence of the transport current. The variation of its energy is indicated schematically in Fig. 12.a. When the vortex moves in the Lorentz force direction, its energy decreases gradually, but when it moves in the opposite direction its energy increases. To overcome the pinning force the vortex should overcome the barrier with height U. If there is no thermal activation the vortex will stay in the pinned state. When the current increases, the height of the barrier decreases until the peak and the bottom of the barrier coincide with each other as shown in Fig. 12.b. In this case the sample is said to be in the critical state i.e. $J = J_c$. At a higher current density continuous flux motion, i.e. flux flow, is expected to occur as in Fig. 12.c. In high T_c superconductors (HTSCs), thermal activation enables the flux lines to overcome the energy barrier at finite temperatures

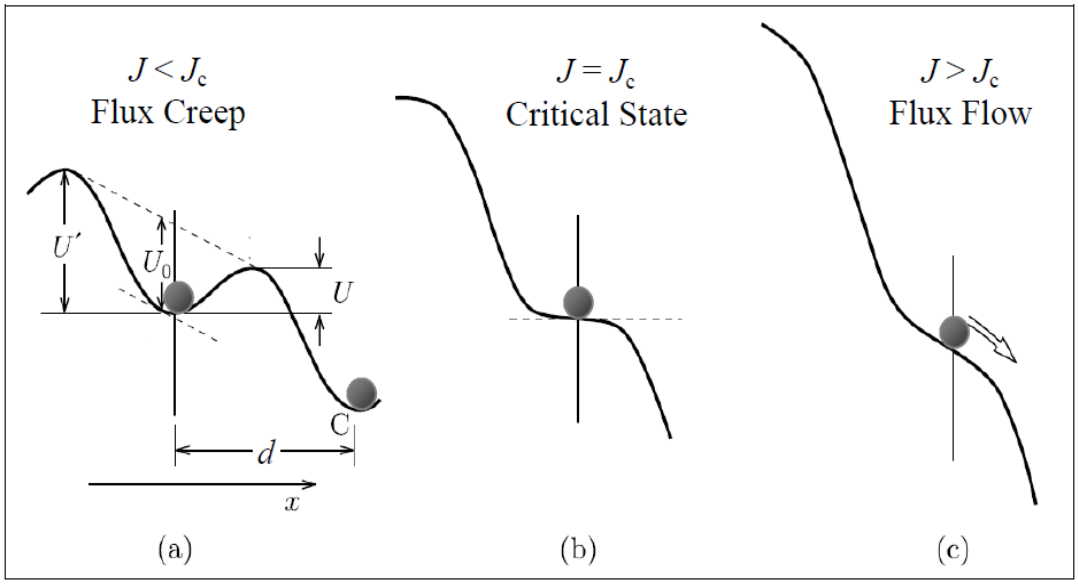

***Fig. 12**: Energy of flux line vs. its position: (a) the case of $J < J_c$, the flux line must overcome the barrier U to be depinned from the potential. (b) The critical state, $J = J_c$ and (c) the flux flow state ($J > J_c$).*

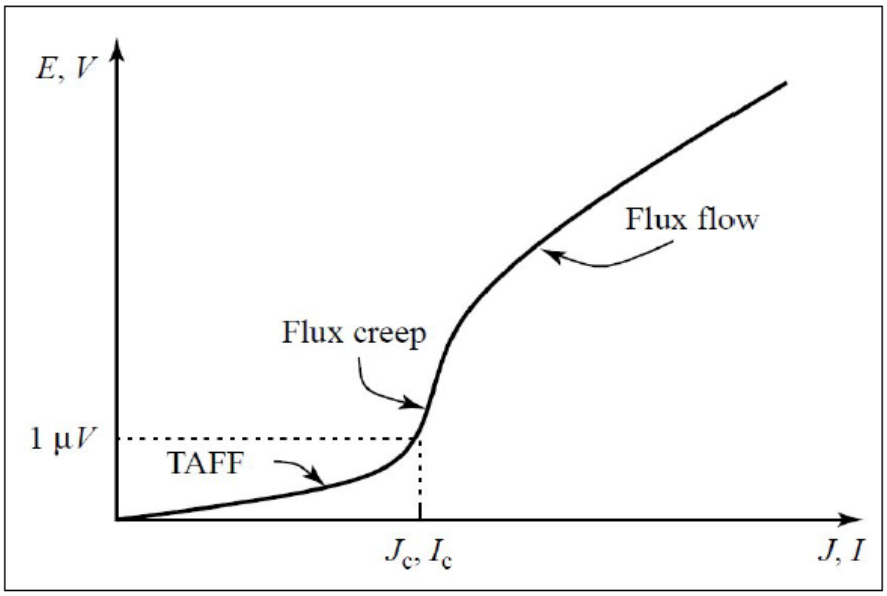

***Fig.* 13:** *A sketch for the definition of I_c or J_c by transport measurement in the presence of an external magnetic field. This curve has a linear V versus I at low I followed by a highly nonlinear region at intermediate values of I, and finally a linear relation again. The effective resistance is quite different in the two regions where ohmic behaviour is found. The plot can be read either as an E–J characteristic or as a I –V characteristic [59].*

even in the state represented by Fig. 12.a. This phenomenon is called thermally assisted flux flow (TAFF) see Fig. 13. The importance of TAFF for HTSCs arises from the fact that, the ratio of the pinning potential barrier U to the thermal activation energy is much smaller than the same ratio in conventional superconductors.

In the flux flow regime, for current $J > J_c$, the resistivity is given by Eq.(14), while at $J < J_c$ the flux creep phenomenon manifests itself in the existence of a finite resistivity. As a result, a type II superconductor at a finite temperature can be generally characterized by a I–V curve (Fig. 13)

$$E = B f\ d \exp\left[-\frac{U}{k_B T}\left(1-\frac{J}{J_{c0}}\right)\right], \tag{15}$$

where E is the generated electric field, d is the distance between pinning centres, J_{c0} is the zero-temperature critical current density and f is the attempt frequency of the flux bundle. The mechanism responsible for the appearance of the electric field is essentially the same as that for flux flow in spite of the quantitative difference and hence a distinction in experiments between flux creep and flow is difficult. The exponential I–V characteristic of a hard type II superconductor (Fig. 13) suggests the existence of a nonzero resistivity at any temperature above absolute zero, $\rho = \rho_0 \exp(-U/k_B T)$. This behaviour is usually referred to as thermally activated flux flow (TAFF). The thermally activated resistivity is exponentially small at low temperatures. At higher temperatures the effect of thermal activation becomes much more pronounced. The pinning potential well $U \to 0$ as $T \to T_c$ and thus the resistivity increases rapidly near T_c. Fig. 13 shows the characteristic I–V curve or E–J curve in the presence of an external magnetic field at $T > 0$. In the curve we can distinguish three different regions; thermally assisted flux flow (TAFF) in the low current end, flux flow in the high current region, and flux creep in the transition region. The particularly important feature of this plot is the highly nonlinear region, where the critical current I_c is marked in the region crossing over between TAFF and flux flow. It is common to define I_c at the point where $E = 1\ \mu$V/cm.

The field at which the **M** versus **B** curve is no longer double valued is known as the irreversibility field B_{irr}. In the field range between B_{irr} and B_{c2} thermal activation leads to flux motion, and only below B_{irr} does the superconductor become hard and the magnetization becomes irreversible. In practical low temperature superconductors this

field is very close to B_{c2} while in high temperature superconductors, thermal activation effects cannot be neglected since B_{irr} is appreciably smaller than B_{c2}.

2.4. Critical current density in type II superconductors

The maximum superconducting current density that the superconductor can carry is a very important factor in practical applications. According to the GL theory, [6] the maximum superconducting current density is given by

$$J_0 = \left(\frac{2}{3}\right)^{3/2} \frac{B_c(T)}{\mu_0 \lambda(T)}, \tag{16}$$

where B_c is the critical thermodynamic magnetic field. Sometimes, J_0 is called the depairing current density. However, the size of the superconductor should be smaller than ξ or λ to attain the depairing current density over its entire cross section.

In the Meissner state the current passing through a thick superconductor is restricted to a thin surface layer where the magnetic field can penetrate. Otherwise the magnetic field due to the current would exist inside the superconductor. On the other hand, in the mixed state the magnetic flux penetrates into type II superconductors in the form of quantized flux lines (FLs). The microscopic currents, connected with them, flow essentially at a length λ around their core as shown in Fig. 8 however, J_0 is reached at a distance comparable with the coherence length ξ. The macroscopic currents are the result of the spatial gradients in the density of FLs or due to their curvature. This is possible only due to the existence of pinning centres, which can compensate the Lorentz force. When the Lorentz force acting on the FLs is balanced by the pinning force density, i.e. $\mathbf{F}_L = \mathbf{F}_p$, and the electromotive force starts to appear, the current density is called the depinning current density J_c. The main difference between the two parameters, J_c and J_0 is that, J_c marks onset of dissipation in a sample still in superconducting state, while at J_0 the material loses its superconductivity.

The external currents applied to a superconductor are referred to as transport currents, in contrast to the shielding currents appearing in the superconductor as circulating currents. According to the Silsbee hypothesis [3] in the case of thick superconductors, i.e. for superconductors with a fully developed shielding layer, the critical current is reached exactly when the magnetic field of the current at the surface attains its critical value. In other words the magnetic field and the current density at a surface with a well developed shielding layer are strongly correlated. The critical value

of the current density J_c is associated with the critical value of the applied magnetic field, i.e. B_c for type I and B_{c2} for type II superconductors, where it is completely irrelevant whether the current density is due to shielding currents or a transport current.

When a type II superconductor is in the mixed state, the transport current can be distributed over the total cross section of the superconductor in the regions where the magnetic field exists, which would allow very high transport current, i.e. the current is no longer restricted to a thin surface layer as the case of type I or type II superconductor in the Meissner state. In this case the Lorentz force acts between the vortices and the current. Under the influence of the Lorentz force the vortices move perpendicular to the current direction and to the magnetic field. Hence we have losses and electrical resistance. Since in an ideal type II superconductor arbitrarily small transport currents already lead to vortex motion, the critical current of such a superconductor in the mixed state is zero [60]. Therefore, such superconductors are useless for technical applications. In other words its applications are restricted by B_{c1} instead of B_{c2}, where the maximum critical current density is $\mu_0 J_{c1} \approx B_{c1}/\lambda$ which is too small in comparison with J_0.

In hard superconductors the vortices are bound to their locations by flux pinning and energy dissipation does not occur until the Lorentz force exceeds the pinning force $\mathbf{F}_\mathrm{p}$. Hence, the critical current is given by

$$J_c = \frac{F_p}{B_a}. \tag{17}$$

Eq. (17) implies that the critical current density J_c is not an intrinsic property as the depairing current density J_0, but it is an acquired property determined by the macroscopic structure of the introduced defects. It is necessary to increase the flux pinning strength in order to increase the critical current density. The determination of the exact value of J_c experimentally is very difficult due to some excitations of the FLs or flux bundles [58], i.e. TAFF and flux creep. There are different models which include the exponential and power-like form of the current– voltage characteristics [58],

$$\frac{E}{E_c} = \exp\left[-\gamma\left(J_c - J\right)\right], \qquad \frac{E}{E_c} = \left(\frac{J}{J_c}\right)^n, \tag{18}$$

where E_c is a critical electric field which corresponds to J_c, see Fig. 14, therefore the determination of J_c is dependent on the definition of E_c. Generally, the most widely used

criterion of E_c = 1 μV cm^{-1} is well suited for practical superconducting samples, although some resistance criteria can be more useful for magnet applications. For classical low temperature superconductors, the values of n and γ are large, hence the critical state model (CSM) is adequate, stating that the currents in regions of changing **B** (or finite electric field **E**) are given by ± J_c, being zero otherwise. The general validity of the simple CSM is mainly due to the fact that the induced currents are usually not considerably larger than J_c. However, there are only a few analytical solutions, which can be used, see the next chapter.

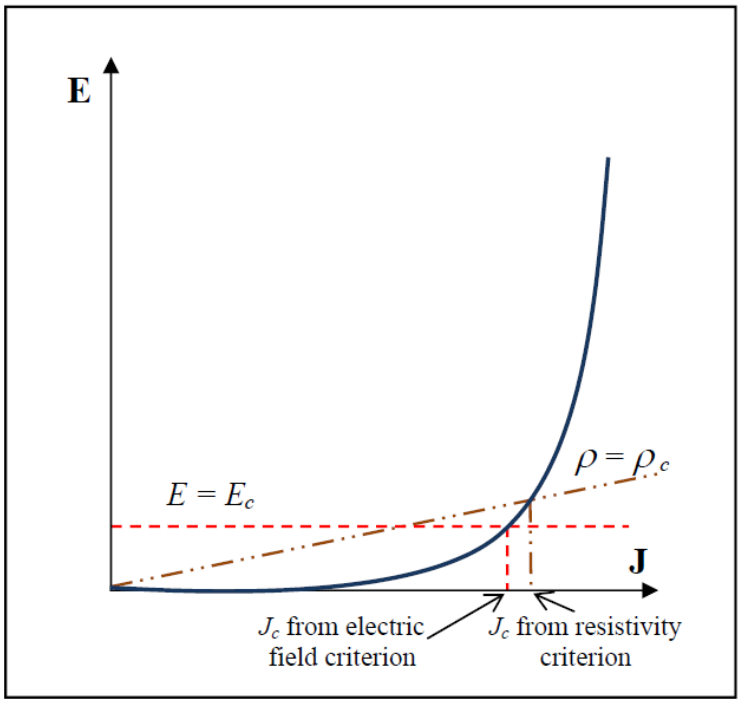

Fig. 14: *Current-voltage curve and methods of determination of critical current density using respective criteria.*

3. Bean critical state model

A useful model to describe superconductors with strong pinning in applied magnetic field is the critical state model (CSM) introduced by Bean [61, 62]. It is a simple model that captures the essential features of some irreversible behaviour of hard superconductors. In Bean's model only two states are possible to occur in the superconductor, zero current for regions with no magnetic flux penetration, and full current with density J_c in regions with partial or complete flux penetration, with a sharp transition and it has thus been named the critical state model. We begin this chapter with a discussion of critical state models in general, and then we introduce the Bean model to a number of cases.

3.1. Critical state

The concept of critical state plays a central role in understanding the irreversible magnetization in hard type II superconductors. In the critical state, a superconductor responds to the change in the applied magnetic field by inducing a shielding current that flows with a critical current density J_c. When the applied field exceeds B_{c1}, the vortices start to penetrate into the superconductor. The vortices arrange themselves so that the driving force which arises from the flux density gradient is equal to the maximum pinning force. In the static state the spatial distribution of the vortices does not vary with time, i.e. $\mathbf{F}_L = \mathbf{F}_P$. High values of the applied fields or currents cause the critical state to penetrate to the inner parts of the superconductor.

The critical state models postulate that for low applied fields or currents, the outer parts of the sample are in a so-called "critical state" with special values of the current density and magnetic flux, and that the interior part is shielded from these fields and currents. These models do not take into account the existence of the lower critical field B_{c1} or the difference between the Meissner and the mixed states. However, they provide a convenient means of describing some experimentally observed phenomena. In all these models the magnetic field **B** and the superconducting current density **J** are coupled through the Maxwell relation

$$\nabla \times \mathbf{B} = \mu_0 \mathbf{J}, \tag{19}$$

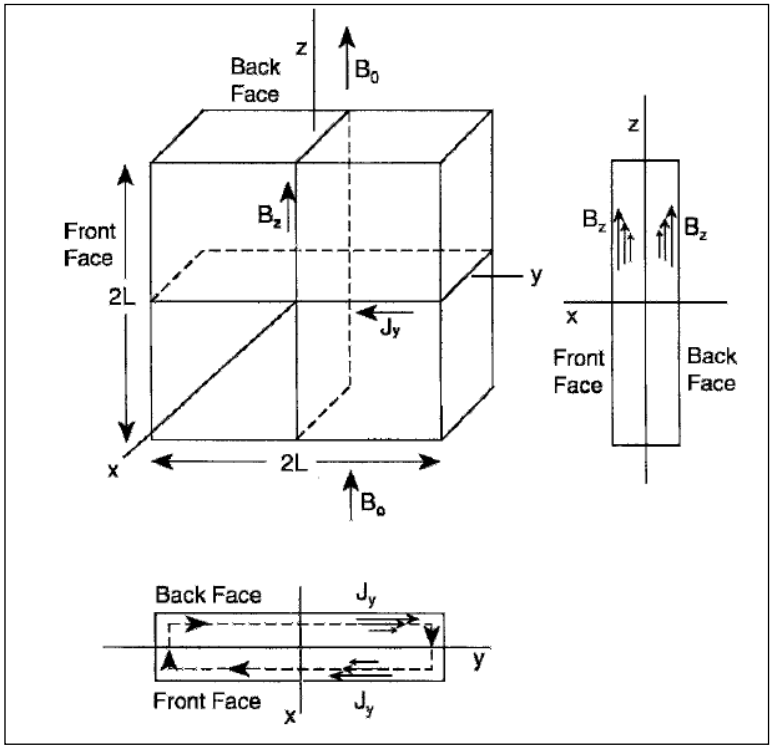

Fig. 15: *Superconducting slab of thickness 2a oriented in the y – z plane with an externally applied magnetic field B_a directed along z – direction. The induced shielding current density J_y flowing in y – direction inside the front and back faces is shown [63].*

which means that the **B** and **J** vectors are perpendicular at every point in space and either one can be calculated from the knowledge of the other.

Consider a superconducting slab oriented parallel to the applied magnetic field $\mathbf{B}_a$ along the *z*– direction as shown in Fig. 15. We assume that the magnetic flux inside the slab, $|\mathbf{B}| = B_z$, is along the *z*– direction and that the current density $|\mathbf{J}| = J_y$ has a component only in *y*- direction. The current density component J_x at the ends of the loops is neglected. For this case the magnetization effect can be neglected, then Eq. (19) is reduced to

$$\frac{d}{dx}B_z(x) = \mu_0 J_y(x). \tag{20}$$

This implies that the flux density and current density depend only on *x*. Other result is that there is a gradient in the internal flux $B_z(x)$ in a direction perpendicular to the current flow direction and hence in the vortex density if it is considered to be in a static equilibrium. For the present case the pinning force density $\mathbf{F}_p$ only has *x*–component with magnitude

$$F_{px} = \frac{1}{2\mu_0}\frac{dB_z^2}{dx}. \tag{21}$$

Equations from (19) to (21) must be satisfied when **B** is in the *z*-direction and **J** is in the *y*-direction. There are many configurations for $B_z(x)$, $J_y(x)$, and $F_p(x)$ that meet this requirement. For example the Bean model assumes J_y = const, while the fixed pinning model assumes F_p = const, all other models assume a more complex relationship between the internal field and the current density. For most models the relationship between $J_y(x)$ and $B_z(x)$ for the slab geometry [63] is of the form

$$J_y\left(B_z\right) = \frac{J_k}{f\left(B_z\right)}, \tag{22}$$

where $f(B_z)$ is a function of the magnetic flux and J_k is a parameter associated with the critical current density independent of the magnetic flux, but can depend on the temperature. J_y is substituted into Eq. (20) and the resultant differential equation is solved to obtain, $B_z(x)$, the position dependence of the internal magnetic flux. Finally, this result is substituted back in Eq. (22) to give J_y(x), while Eq. (21) immediately provides $F_p(x)$.

Table 1 [63] gives the current–field relationships for several well known critical state models. In these expressions the internal flux density is **B** = **B**(*x*), where *x* is the distance from the centre toward the surface. In most of the models J_c is the critical current in the absence of an applied field. Each of the critical-state models depends on a parameter B_k associated with the internal field and a parameter J_k associated with the critical current density. Both of these parameters can depend on the temperature. A general power law model can be written as $J(B) = A\,|B(x)|^{-n}$ [64, 65], which reduces to the Bean, square root and fixed pinning models for n = 0, ½ and 1 respectively. Kim model resembles the fixed pinning model for high applied fields, $|B(x)| >> B_k$, while the exponential model, linear model with $J_k = J'_K$, and Kim model all reduce to the Bean model for low applied fields, $|B(x)| << B_k$.

The explicit expressions for $B(x)$ and $J(x)$ that are obtained by solving the differential Eq. (20) for the functions of Eq. (22) for various cases depend on boundary conditions, such as the strength of the applied field, size, shape, orientation of the sample, and previous magnetic history.

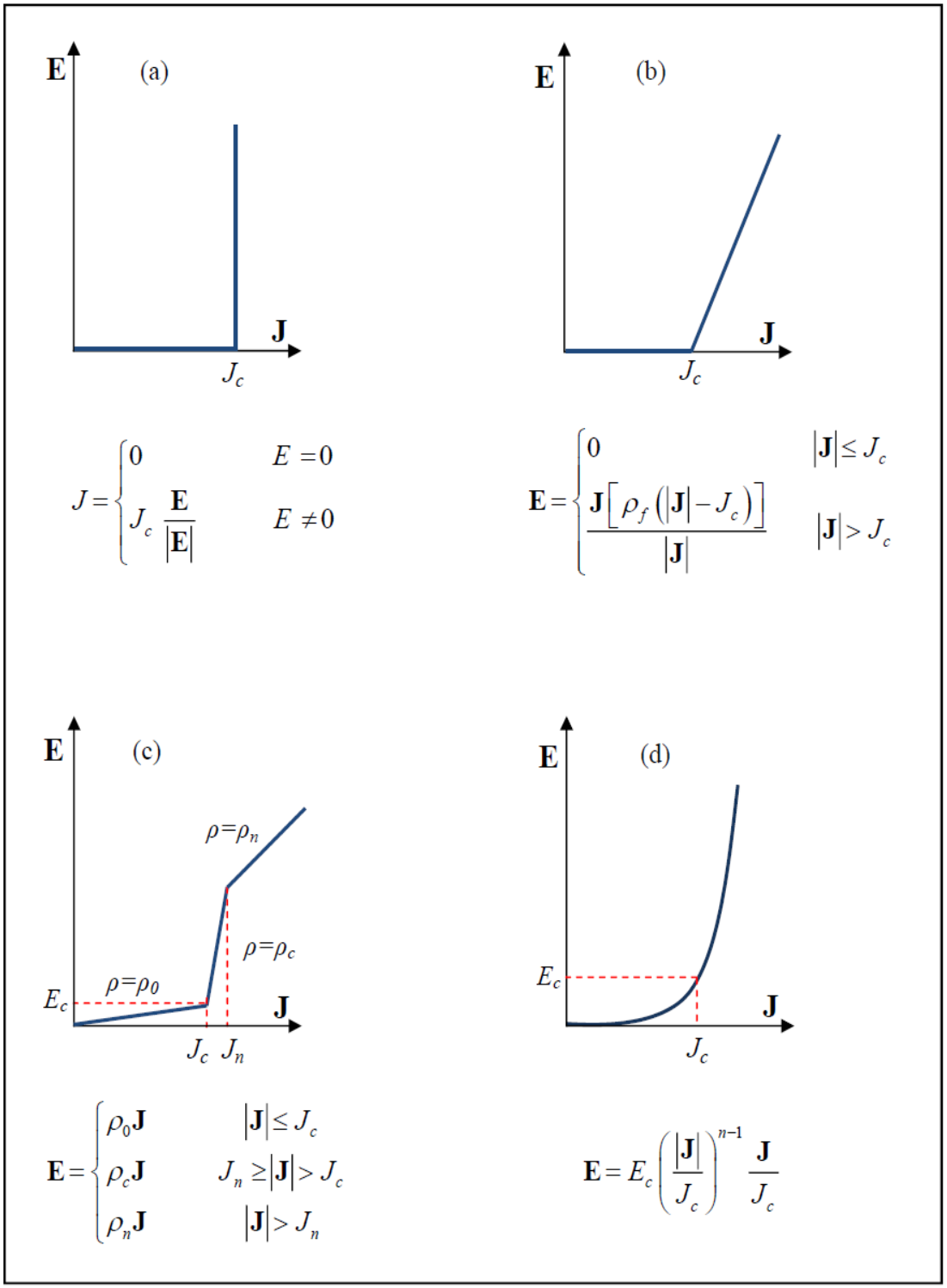

Fig. 16: *The E – J relation in (a) Bean model (b) linear critical state model (c) generalized critical state model, where ρ_n is the normal resistivity and ρ_0 and ρ_c have very small and high values respectively (d) power law model.*

Table 1: *Current–field relationships corresponding to Eq. (22) for several critical state models [63].The quantity, $\Theta[B_k - |B(x)|]$, is the Heaviside step function.*

$J(B)=J_c$	Bean [61, 62]
$J(B)=\frac{J_c}{\lvert B(x)\rvert/B_k}$	Fixed Pinning [66]
$J(B)=\frac{J_c}{\lvert B(x)/B_k\rvert^{1/2}}$	Square Root [66]
$J(B)=\frac{J_c}{1+\lvert B(x)\rvert/B_k}$	Kim [67, 68]
$J(B)=J_c\exp\left[-\lvert B(x)\rvert/B_k\right]$	Exponential [69]
$J(B)=J_c-J_c'\lvert B(x)\rvert/B_k$	Linear [70]
$\mathrm{J(B)}=J_c\left(1-\lvert\mathrm{B}(x)\rvert/\mathrm{B}_k\right)\Theta\left(B_k-\lvert B(x)\rvert\right)$	Triangular Pulse [71]
$J(B)=\frac{J_c}{\left[1+\lvert B(x)\rvert/B_k\right]^{\beta}}$	Generalized [72, 73]

The **E** – **J** relation in the critical state models can take different shapes. In Ohm's law this relation is given by **E** = ρ**J,** where ρ is the resistivity of the material. The main problem in the modelling of type II superconductors is the definition of the resistivity, which is not constant and consequently Ohm's law is nonlinear. The **E** – **J** curves due to dynamic effects are shown in Fig. 13 and Fig. 14. Fig. 16 depicts the theoretical **E** – **J** curves in a number of critical state models. In Bean model (Fig. 16.a), the relation is discontinuous step–like function where the current density cannot exceed some critical value J_c and until this threshold is reached, the electric field is zero. Because of its simplicity, the Bean model is widely used for theoretical derivations of AC losses in simple geometries such as disk, strip, slab and cylinder. Instead of a sharp transition of the Bean model, a linear part above J_c can be introduced [16, 74], where it takes into account the flux-flow resistance as can be seen in Fig. 16.b. Another possible relation is introduced by generalizing the Bean model [75] as shown in Fig. 16.c. The transition to the normal state is introduced at the point where the resistivity reached the normal value ρ_n. The power law [76-78] is shown in Fig. 16.c. The **E**–**J** relation is a smooth function. The limiting cases of $n = 1$ and $n = \infty$ correspond to the linear Ohm's law and Bean model respectively.

3.2. Bean model

The Bean critical state model (BCSM) [61, 62] is the simplest and the most widely used one of the critical state models that have been proposed for describing the field and current distribution in hard superconductors. The model serves as a straightforward phenomenological explanation for many experimental results on hard superconductors in the critical state, even for many results in high temperature superconductor (HTSC) materials. However the model does not give any explanation for the microscopic origin of pinning.

These are the basic assumptions of the Bean critical state model [79]:

- The critical current density is independent of the external magnetic field.
- Only the critical state is considered. There is no reversible magnetization and $B_{c1} = 0$.
- There is a critical current density J_c which can be carried by the superconductor.
- Even very low electromagnetic forces induce the full critical current density.
- In any region of the superconductor where magnetic flux has penetrated, the critical current density is perpendicular to the magnetic induction **B**, everywhere else $J_c = 0$ is valid.

Nevertheless, there are some important limitations to the Bean critical state model:

- There is no Meissner state in Bean's considerations.
- In some cases the critical current density depends strongly on the external magnetic field.
- The model does not consider the origin of the critical current density.
- The model neglects geometric barriers and dynamic effects like the flux creep effect.

The solution of Bean model depends on the sample shape and the arrangement of the applied magnetic field. Analytical solutions are found only in a few cases.

3.2.1. Bean critical state in longitudinal geometry

Infinitely long superconductors in parallel applied field $\mathbf{B_a}$ exhibit no demagnetizing effects. For infinite slabs and circular cylinders the problem is 1D and for general cross-section (e.g. rectangular bars) it is 2D. The linear or nonlinear response is obtained by solving a 1D or 2D linear or nonlinear diffusion equation. Many papers have discussed this problem, see for example [41, 80, 81] and the references

within them. The resulting expressions are often used to evaluate experiments even when this longitudinal geometry does not apply.

In this case the current density can take only three values $J = \pm J_c$ at the flux penetrated regions, where the slope of $B(r)$ is constant, and $J = 0$ at the flux free regions. The flux profile and critical current density distribution for a long slab of width $2a$ in a longitudinal applied magnetic field $\mathbf{B_a}$ along z-direction are shown in Fig. 17. The following is seen in Fig. 17 from left to right:

a) When the applied magnetic field B_a increases from zero, following Lenz's law, screening currents are induced at the outer parts of the slab. These induced currents have direction such as to oppose the variation of the field and screen the interior of the sample. The flux partially penetrates the sample and decreases linearly towards its centre with a slope $\partial B_z/\partial x = \pm \mu_0 J_c$. In the penetrated regions the current density is $\pm J_c$, otherwise it is zero.

b) As the amplitude of B_a reaches the full penetration field, B_p, the flux will penetrate into the centre of the sample and the whole sample will carry current with density $\pm J_c$.

c) Further enhancement of B_a leads to the introduction of more flux into the sample. Since the screening current density cannot exceed J_c, they will not oppose any further to the increase of the field inside the superconductor and the penetration pattern will simply shift upwards. The difference between the magnetic flux at the edge and the centre of the specimen remains constant and equal to B_p.

d) When the external field decreases, the screening currents have to oppose this change and near the edges of the sample areas an inverted current will exist. In the rest of the sample the field and the current density remain unchanged.

e) At $|\mathbf{B_a}| = 0$ there is still flux inside the superconductor and the flux distribution takes the form of a cone, which is referred as Bean cone, while the current patterns are completely reversed.

Once the applied field increases again, new regions with inverse currents appear at the edges and the previous steps can be repeated. We can see from the figure that the distribution of $B_z(x)$ is symmetric about the point $x = 0$, while the critical current density

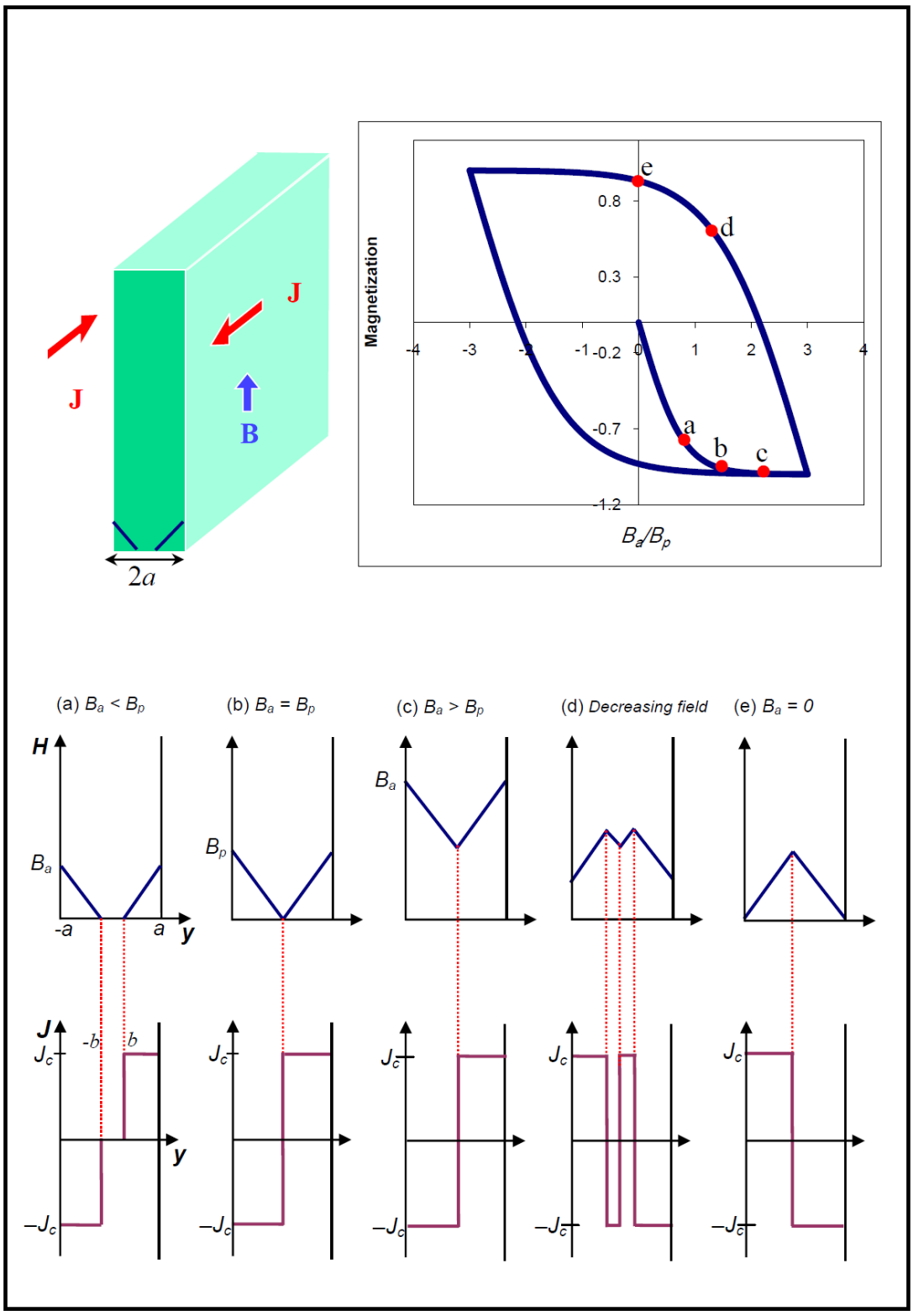

Fig. 17: *Bean model to a slab in a parallel magnetic field B_a. (Top left) A slab with width 2a in longitudinal magnetic field. (Top right) The magnetization versus applied magnetic field. The virgin curve from Eq. (43) saturates when full penetration is reached at $B_a = B_p$. The hysteresis loop follows from Eq. (47). (Middle) Profiles of the current and field distribution. The letters correspond to the letters in the magnetization curve.*

$J_y(x)$ is anti–symmetric about this point. Following from Eq. (20), the critical state profile in a long slab geometry which corresponds to Fig. 17 in low fields $|\mathbf{B_a}| < B_p$ is given by

$$J_y(x) = \begin{cases} J_c & -a \le x < -b \\ 0 & -b \le x < b \\ -J_c & b \le x \le a \end{cases} \tag{23}$$

$$B_z(x) = \begin{cases} B_a\left(\dfrac{b+x}{b-a}\right) & -a \le x < -b \\ 0 & -b \le x < b \\ B_a\left(\dfrac{x-b}{a-b}\right) & b \le x \le a \end{cases} \tag{24}$$

These expressions match the boundary condition $B_z(\pm a) = B_a$ on the two surfaces at $x = \pm a$. The quantities J_c and B_a are related to each other by the expression $J_c = B_a/\mu_0(a - b)$. At high fields $|\mathbf{B_a}| \ge B_p$ the magnetic field and the critical current reach to the centre of the sample, hence equations (23) and (24) become

$$J_y(x) = \begin{cases} J_c & -a \le x < 0 \\ -J_c & 0 \le x \le a \end{cases} \tag{25}$$

$$B_z(x) = \begin{cases} B_a - B_p\left(\dfrac{a+x}{a}\right) & -a \le x \le 0 \\ B_a + B_p\left(\dfrac{a-x}{a}\right) & 0 \le x \le a \end{cases} \tag{26}$$

It is worth mentioning that the current density distribution and the magnetic profile in a long slab (Fig. 17) is qualitatively the same as in a long cylinder.

3.2.2. Bean critical state in transverse geometry

In previous section we have discussed the application of Bean model to hard type II superconductors when the specimen is an almost infinitely extended cylinder or slab with constant J_c in a parallel magnetic field, where demagnetizing effects are neglected. However, most experiments deal with thin flat samples in a perpendicular applied magnetic field $\mathbf{B_a}$.

In general the current and field profiles in thin type II superconductors in a perpendicular applied magnetic field are qualitatively different from the Bean model for parallel magnetic field in many ways [82].

1) In transverse geometries, the flux penetration initially is quadratic in $\mathbf{B_a}$, i.e. it looks delayed as if there were a surface barrier or large lower critical field B_{c1}. While in longitudinal geometries it is linear.
2) The deviation of the magnetic moment from linearity and remaining moment initially are cubic in $\mathbf{B_a}$. On the other side it is quadratic in longitudinal geometries.
3) The AC losses initially grow with the fourth power of the applied field amplitude, while in longitudinal geometries grow with third power of $\mathbf{B_a}$.
4) The penetrating flux front has vertical slope, while in longitudinal geometries it is constant.
5) When the flux has partially penetrated and the critical state is established in the outer regions, the currents flow in the entire width of the sample to shield the central flux free region. On the other hand in longitudinal geometries the flux free regions are current free.
6) The screening current density is continuous with a vertical slope at the flux front where $J = J_c$, whereas in longitudinal geometries it is a piecewise constant.
7) As soon as the direction of $\mathbf{B_a}$ is changed or reversed, the current density in thin films ($d < \lambda$, where d is the thickness of the sample) falls below J_c everywhere, while in longitudinal geometries $J = J_c$.
8) In a perpendicular field the shielding current is mainly caused by curvature of the magnetic field lines and not by the gradient of the flux lines, i.e. shielding currents mainly come from the flux radial gradient $\mu_0 J = \partial B_z/\partial r$ in case of cylinder and slab while mainly from the flux axial gradient $\mu_0 J = \partial B_r/\partial z$ in the case of disk and strip.

In this section we will concentrate on thin disk and strip in a perpendicular applied magnetic field.

3.2.2.1. Thin disk in a perpendicular applied magnetic field

Mikheenko and Kuzovlev created the Bean critical state model for 2D disk-shaped superconductor [83]. They found the complete analytical solutions of field and current patterns in a thin superconducting disk in perpendicular time-varying periodic applied magnetic fields. This model was extended and corrected by Zhu et al. [84]. They proved that the current density decreases continuously in vortex-free annulus from J_c to zero in the centre of the disk as shown in Fig. 18. They also gave analytical solutions to the magnetic moment and the effective magnetic susceptibility. They showed that the analogy of current patterns between a thin film disk and a long

cylindrical superconductor is not valid. They explained that because of strong demagnetizing effects, the flux density bends around the disk and shielding currents flow over the entire surface of the disk. In general the circular shielding current density is given by [85]

$$J(r) = \frac{1}{\mu_0}\left(\frac{\partial B_r}{\partial z} - \frac{\partial B_z}{\partial r}\right). \tag{27}$$

In case of a thin disk the magnitude of $\partial B_r/\partial z$ is much larger than the magnitude of $\partial B_z/\partial r$ for weak external fields except at the centre of the disk. Thus, the shielding current mainly comes from the term $\partial B_r/\partial z$ in contrast to the case of a long cylindrical sample. The model is constrained for the film thickness $d \leq 2\lambda$, where λ is the London flux penetration length, to assure that the circulating currents in the film plane may be treated as having uniform density in the thickness direction. Also, the external field is assumed to be weak enough so that the critical current density in the film is independent of the local density of trapped vortices, i.e. $J_c\, d$ = const. A characteristic field for disk geometry is defined as $B_d = \mu_0\, J_c\, d/2$.

In 2D disk-shaped superconductors, as the external field is decreased from the maximum field B_0, the current density flowing in the outer annulus $b_1 < r < R$ is the critical current density $+J_c$. In the inner annulus $0 < r < b_1$ the current density $J(r)$ is a function of location r as is indicated in Fig. 18. In the region where $0 < r < b_2$, there is no flux penetration. In any case the critical current density must satisfy constraint $|J(r)| \leq J_c$.

Clem and Sanchez extended this model for either $d \geq \lambda$ or, if $d < \lambda$, that $\Lambda = 2\lambda^2/d << R$, where Λ is the two-dimensional screening length [86]. They introduced analytical solution to hysteretic current density, magnetic flux density profiles in the critical state and hysteretic magnetization curves. They presented limiting expressions for fundamental complex AC susceptibility components $\chi(B_0/J_c d)$ on basis of this model and gave an approximate behaviour. They concluded that for finite applied fields the annular region where the current density is J_c never fills the entire disk, and the critical state flux density profiles never penetrate all the way to the centre, where B_z remains equal to zero. In real thin films however, the above 2D approach breaks down and B_z becomes nonzero when the vortex free radius b_2 approaches the largest of the quantities d, λ and Λ. They summarized that independently of geometry of the sample the

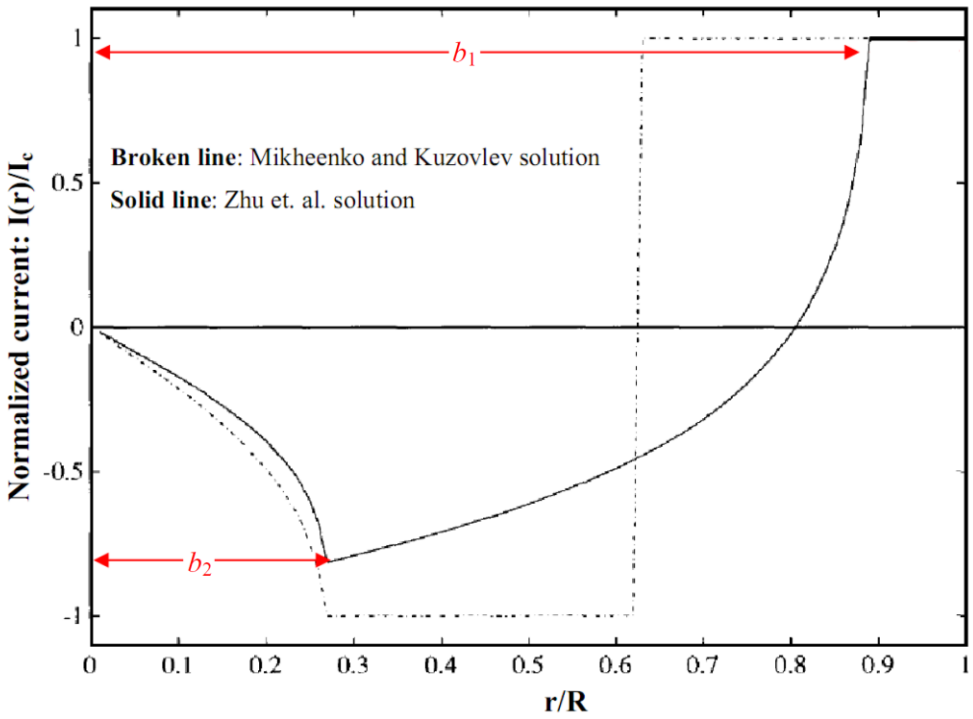

Fig. 18: *Normalized current patterns in a 2D disk-shaped superconductor for $B_0 = 2B_d$ and $B_a = B_d$. The solid line is Zhu et al. solution while the dashed line is Mikheenko and Kuzovlev solution [84].*

hysteretic critical state behaviour is that during quasi-static changes of an applied magnetic field, vortices move and thus the local flux density **B** changes.

Let us consider the Clem and Sanchez solution for a thin type II superconducting disk in the critical state [86]. The distribution of a current density and magnetic field for a disk of radius R and uniform thickness d, where $\lambda \leq d << R$ is shown in Fig. 19. The disk is considered to be in $x-y$ plane and centred in the $z-$axis. In cylindrical coordinates $\rho = (x^2 + y^2)^{½}$ and $\phi = \tan^{-1}(y/x)$. If $d < \lambda$, the screening length $\Lambda = 2\lambda^2/d << R$. We can distinguish two cases: for increasing and decreasing field.

For increasing fields:

Consider the disk is initially cooled to low temperature in the absence of a magnetic field. The disk contains no vortices. Application of a weak magnetic field induces azimuthal screening currents in the disk. Due to the high demagnetization factor, the applied magnetic field bends around the disk as is shown in Fig. 19.a, hence screening currents arise from the discontinuity of radial magnetic induction at $z = \pm d/2$. These currents flow on the surface of the specimen even without field penetration.

Strong demagnetizing factor is responsible for the sharp rise in the value of the flux density near the edge of the film. The distribution of the current and the flux density profile for $B_a < B_{c1}$ are given as

$$J_\phi(\rho) = -\left(4B_a/\mu_0\pi d\right)\rho/\left(R^2-\rho^2\right)^{1/2}, \tag{28}$$

$$B_z(\rho,0) = \begin{cases} 0, & \rho \le R, \\ B_a\left\{1+\dfrac{2}{\pi}\left[\dfrac{1}{\sqrt{(\rho/R)^2-1}} - \sin^{-1}\left(\dfrac{R}{\rho}\right)\right]\right\}, & \rho > R. \end{cases} \tag{29}$$

When the local magnetic field at the edge of the sample exceeds B_{c1} the vortices start to penetrate into the superconductor from the edges of the sample in the absence of the edge barrier. In the presence of pinning centres vortices penetrate only as far as necessary to reduce the magnitude of the current density J to J_c, where the magnitude of $J_\phi(\rho)$ is equal to J_c throughout the annular filled region, whose inner radius b_2 is given by $b_2 = R/\cosh(B_a/B_d)$. The current can not change discontinuously in the interior of the film, so its magnitude decreases continuously from $J = J_c$ at $\rho = b_2$, to zero at $\rho = 0$ at the centre of the disk. In this case ($B_a > B_{c1}$) equations (28) and (29) have to be changed to

$$J_\phi(\rho) = \begin{cases} -(2J_c/\pi)\tan^{-1}\left[(\rho/R)\left(R^2-b_2^2\right)^{1/2}\Big/\left(b_2^2-\rho^2\right)^{1/2}\right], & \rho \le b_2, \\ -J_c, & b_2 < \rho < R, \end{cases} \tag{30}$$

$$\frac{B_z(\rho,0)}{B_d} = \begin{cases} 0, & 0 \le \rho \le b_2, \\ \cosh^{-1}(R/b_2) - \cosh^{-1}(R/\rho) + \displaystyle\int_{\sin^{-1}(b_2/\rho)}^{\pi/2} P_1(\rho/R,\theta)\,d\theta, & b_2 < \rho < R, \\ B_a/B_d + \displaystyle\int_{\sin^{-1}(b_2/R)}^{\pi/2} P_2(\rho/R,\theta)\,d\theta, & \rho > R, \end{cases} \tag{31}$$

where

$$\begin{aligned} P_1(x,\theta) &= \frac{2}{\pi}\left[\frac{1-\theta\cot\theta}{\left(1-x^2\sin\theta\right)^{1/2}}\right], && x < 1, \\ P_1(x,\theta) &= \frac{2}{\pi}\left[\frac{1}{\left(x^2-\sin^2\theta\right)^{1/2}} - \frac{\sin^{-1}\left(x^{-1}\sin\theta\right)}{\sin\theta}\right], && x > 1. \end{aligned} \tag{32}$$

The value of b_2 suggests that the annular region where the current density equals to J_c never fills the entire disk and the critical state flux density profile never penetrates

to the centre where $B_z(0,0)$ remains equal to zero. However, in practice the field at the centre of the film becomes nonzero when b_2 approaches the largest of quantities d, λ and the screening length $\Lambda = 2\lambda^2/d << R$ [87]. The induced azimuthal current density $J_\phi(\rho)/J_c$ and the corresponding flux density distribution $B_z(\rho,0)/B_d$, where $B_d = \mu_0 J_c d/2$ is shown in Fig. 19.c for B_0/B_d = 0.75, 1.5, 2.5 and 3. Theses curves have been calculated from Eq. (30) and Eq. (31).

For decreasing field:

When B_a is decreased, i.e. is reduced from B_0 to $-B_0$, both the current density profile and the magnetic flux density distribution change, where they can be given by

$$J_\phi(\rho) = \begin{cases} -(2J_c/\pi)\tan^{-1}\left[(\rho/R)\left(R^2-b_2^2\right)^{1/2}\Big/\left(b_2^2-\rho^2\right)^{1/2}\right] \\ \quad +(4J_c/\pi)\tan^{-1}\left[(\rho/R)\left(R^2-b_1^2\right)^{1/2}\Big/\left(b_1^2-\rho^2\right)^{1/2}\right], & \rho \le b_2, \\ -J_c+(4J_c/\pi)\tan^{-1}\left[(\rho/R)\left(R^2-b_1^2\right)^{1/2}\Big/\left(b_1^2-\rho^2\right)^{1/2}\right], & b_2 < \rho \le b_1, \\ +J_c, & b_1 < \rho < R, \end{cases} \tag{33}$$

$$\frac{B_z(\rho,0)}{B_d} = \begin{cases} 0, & 0 \le \rho \le b_2 \le b_1 \le R, \\ \left[\cosh^{-1}(R/b_2)-\cosh^{-1}(R/\rho)\right]+\int_{\sin^{-1}(b_2/\rho)}^{\pi/2} P_1(\rho/R,\theta)\,d\theta, & b_2 \le \rho \le b_1 \le R, \\ \left[\cosh^{-1}(R/b_2)-\cosh^{-1}(R/\rho)\right]-2\left[\cosh^{-1}(R/b_1)-\cosh^{-1}(R/\rho)\right] & \\ \quad +\int_{\sin^{-1}(b_2/\rho)}^{\sin^{-1}(b_1/\rho)} P_1(\rho/R,\theta)\,d\theta-\int_{\sin^{-1}(b_1/\rho)}^{\pi/2} P_1(\rho/R,\theta)\,d\theta, & b_2 \le b_1 \le \rho < R, \\ B_a/B_d+\int_{\sin^{-1}(b_2/\rho)}^{\sin^{-1}(b_1/\rho)} P_2(\rho/R,\theta)\,d\theta-\int_{\sin^{-1}(b_1/\rho)}^{\pi/2} P_2(\rho/R,\theta)\,d\theta, & b_2 \le b_1 \le R < \rho. \end{cases} \tag{34}$$

Within an annulus of inner and outer radii b_1 and R the critical current density is equal to J_c as indicated in Fig. 18. In this annulus the vortices experience a Lorentz force, which drives them out of the sample as the field initially decreases. The inner radius of the annulus where $J = J_c$ and the flux density is decreasing is $b_1 = R/\cosh[(B_0 - B_d)/2B_d]$. On the other hand, the vortex free radius is $b_2 = R/\cosh(B_0/B_d)$. The current density changes as a continuous function of the position and increases from its minimum at $\rho = b_2$, to $+J_c$ at $\rho = b_1$. This leads to a superposition

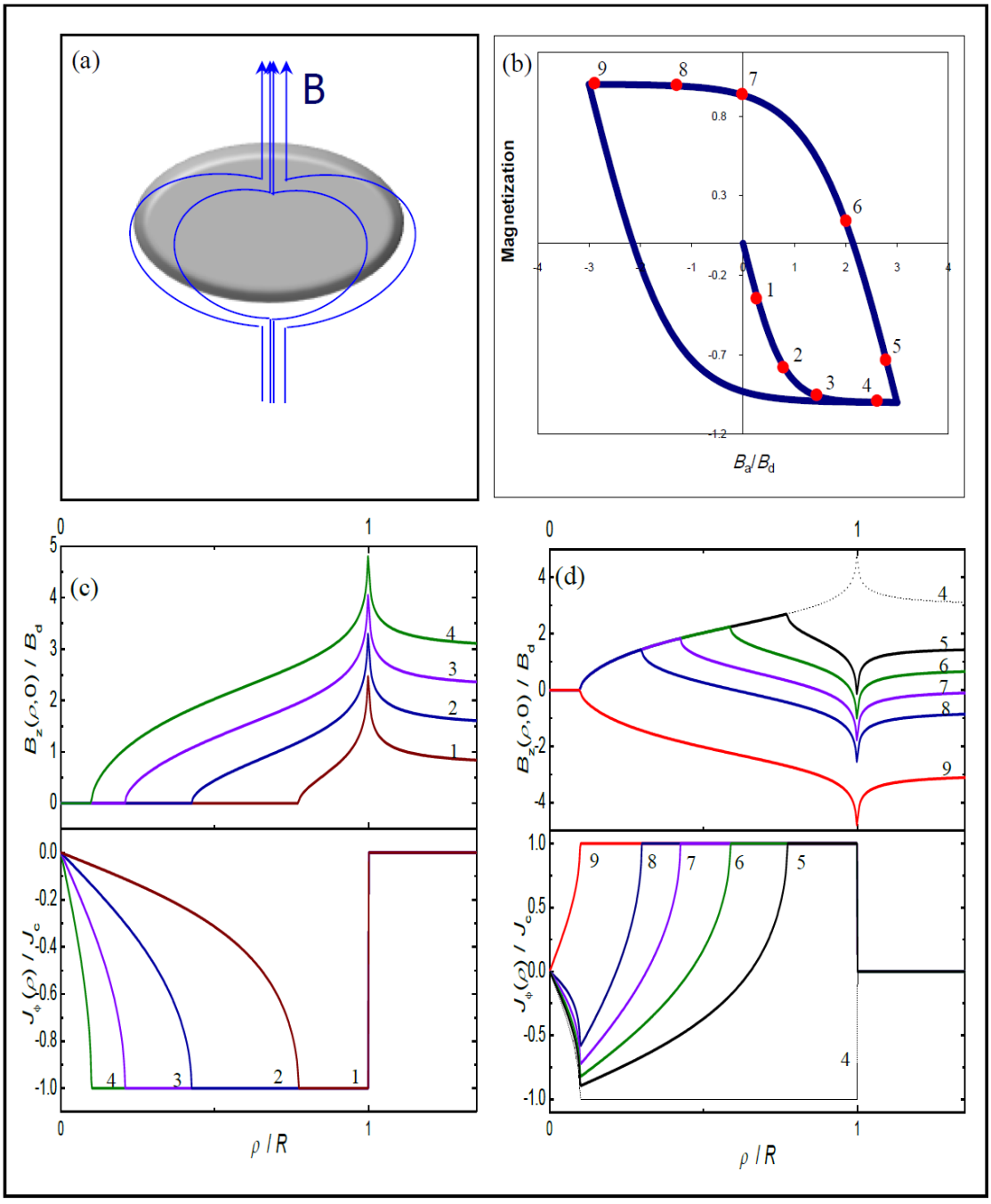

Fig. 19: *Bean model for a type II superconducting disk in a perpendicular magnetic field. (a) Due to strong demagnetizing factor, the magnetic flux density bends around the disk. (b) The magnetization curve where the numbers are corresponding to the numbers in current and field profiles. (c) The current distribution and magnetic field profile in increasing applied fields B_0/B_d = 0.75, 1.5, 2.5 and 3, (d) in decreasing fields B_0/B_d = 3, 1.5, 0.75, 0, -0.75 and -3.*

of the frozen flux contribution and the reverse field contribution. When the applied field is decreased continuously, the current density and flux density profile inside the sample completely reverse their direction. Fig. 19.d shows the profiles of both the magnet flux density and the current density for B_0/B_d = 3, 1.5, 0.75, 0, -0.75 and -3. It is worth mentioning that, the current density profiles are antisymmetric around the origin point where the flux density profiles are symmetric. In Fig. 19.b, the complete hysteresis magnetization loop is demonstrated. The numbers in the curve correspond to the numbers in Fig. 19.c and Fig. 19.d.

3.2.2.2. Thin strip in a perpendicular applied magnetic field

The Bean critical state model of thin strips of constant thickness was first solved for current carrying strips by Norris [88]. This classical work was extended to strips in a perpendicular magnetic field without transport current [89] and with transport current [82, 90] and later to current carrying strips with an elliptical cross section by Yang et al. [91].

Brandt et al. [82, 89] calculated analytically the current density and local magnetic field for a strip of type II superconductors in perpendicular magnetic field, $\mathbf{B}_a$, assuming constant J_c. He found that the exact solution for a strip is different from the original Bean model. As a matter of fact, the magnetic flux density and current density profiles in a thin strip and circular disk are qualitatively the same. Hence Fig. 19.b, c and d also describe the critical state distributions in a flat superconducting strip. The strip is considered to be with width $2a >> d$ and filling the space $|x| \leq d/2$, $|y| \leq a$, $|z| < \infty$, in which a spatially constant magnetic field $\mathbf{B}_a$ applied along x induces a supercurrent density $\mathbf{J}(x, y)$ along z–direction. When $d >> \lambda$ the current is completely pure Meissner current. This current flows in two surface layers of thickness λ and leaves the central free region, current free. On the other hand if $d < \lambda$ the current is vortex current, which is nearly constant over the thickness d. As soon as the flux penetrates, the current density is limited to J_c. If J is $|J| = J_c$, the flux lines move and rearrange such that $|J| < J_c$ is held everywhere. In Meissner state the ideal shielding current is given by

$$J(y) = 2y\, B_a / \mu_0 \left(a^2 - y^2\right)^{1/2}. \tag{35}$$

While the magnetic flux density profile outside the sample is expressed as

$$B\left(|y|>a\right)=|y|B_a\Big/\mu_0\left(y^2-a^2\right)^{1/2}. \tag{36}$$

When the applied magnetic field is increased, the shielding current saturates near the edges of the strip to $J\ (y > b) = J_c$ and the vortices penetrate within a region where $b < y < a$. In this case the current distribution and the magnetic flux density are given by

$$J\left(y\right)=\begin{cases}\dfrac{2J_c}{\pi}\tan^{-1}\dfrac{c\,y}{\left(b^2-y^2\right)^{1/2}}, & |y|<b,\\ J_c\,y/|y|, & b<|y|<a,\end{cases} \tag{37}$$

$$B\left(y\right)=\begin{cases}0, & |y|<b,\\ B_d\tanh^{-1}\dfrac{\left(y^2-b^2\right)^{1/2}}{\mu_0 c\,|y|}, & b<|y|<a,\\ B_d\tanh^{-1}\dfrac{c\,|y|}{\mu_0\left(y^2-b^2\right)^{1/2}}, & |y|>a,\end{cases} \tag{38}$$

where $b = a/\cosh(B_a/B_d)$, $c = \tanh(B_a/B_d)$ and $B_d = \mu_0 J_c\, d/\pi$ is a special critical field for the strip.

When the applied field B_a is decreased from $+B_0$ to $-B_0$, the current density $J\,(y, B_a, J_c)$ and the magnetic field $B\,(y, B_a, J_c)$ are given by a linear superposition from the virgin results in equations (35) to (38)

$$\begin{aligned}J\left(y,B_a,J_c\right) &= J\left(y,B_0,J_c\right)-J\left(y,B_0-B_a,2J_c\right),\\ B\left(y,B_a,J_c\right) &= B\left(y,B_0,J_c\right)-B\left(y,B_0-B_a,2J_c\right).\end{aligned} \tag{39}$$

3.2.3. Magnetization curve

The magnetization M of a sample is related to $B(r)$ and $B_a = \mu_0 H_a$ by the relation

$$\left\langle \mu_0 M\right\rangle=\left\langle B\left(r\right)\right\rangle-B_a, \tag{40}$$

where $< >$ denotes the average over the whole sample volume, thus the magnetization determines how great is the difference between the average internal field and the applied field. Calculation of the magnetization from a series of flux distributions and critical current density profiles yields a diamagnetic hysteresis loop as indicated in Fig. 17 and Fig. 19. The area of the hysteresis is a measure of the energy dissipation. For a slab case depicted in Fig. 15, the energy loss, W, per unit volume per cycle is [63]

$$W = \oint M \, dB_a = \frac{2B_0^2}{\mu_0}\Gamma(h_0), \tag{41}$$

where $\Gamma(h_0)$ is the loss factor [63] and h_0 is a dimensionless factor, $h_0 = B_0/B_p$, where $B_p = \mu_0 J_c a$ is the field of full penetration. On the basis of Bean model, this enables the quantitative determination of J_c from magnetization hysteresis, but only where the magnetization curve does not have a significant slope where J_c can be given by

$$J_c = K\frac{\Delta M}{R}, \tag{42}$$

where $\Delta M = M\uparrow - M\downarrow$ and $M\downarrow$ and $M\uparrow$ are the branches in increasing and decreasing B_a respectively. Here R is the dimension of the sample perpendicular to the field direction and K is a constant that depends on the geometry of the sample. From Eq. (42) we can notice that the wider the magnetization loop is, the higher is J_c. Before computing the value of J_c one should attempt to remove the equilibrium part of the magnetization curve, i.e. the $M(B_a)$ curve which is obtained without pinning.

As it was mentioned above, virgin and hysteresis curve calculations for an infinitely long cylinder and slab in parallel magnetic field were presented by Bean [62], while Campbell and Evetts [41] considered the case of a finite rectangle, and provided a method for elliptic and arbitrary cross-sections in small fields. On the other hand Brandt et al. [82, 89], and Clem and Sanchez [86] gave the analytical virgin and hysteresis curve for a thin strip and disk in perpendicular field respectively. In general the total magnetic moment **m** due to a current density $J(r)$ in an arbitrarily shaped sample is given by $|\mathbf{m}| = MV = \tfrac{1}{2}\int r \times J(r)\, d^3r$, where V is total volume of the sample. Within Bean model, m depends only on the sample shape and on the orientation of the applied field B_a. Being irreversible, m depends on the history of $B_a(t)$, but it does not depend explicitly on time t. The magnetic moment of a long superconducting slab of width $2a$ and area A, and a long cylinder with radius a and length L, in a parallel field can be given by [41, 61, 62]

$$m_{slab} = -J_c a^2 A(2h - h^2), \tag{43}$$

$$m_{cly} = -\pi J_c a^3 L(h - h^2 + h^3/3), \tag{44}$$

for $0 < h < 1$ with $h = B_a/B_p$, where $B_p = \mu_0 J_c a$ is the field of full penetration. For $B_a \geq B_p$ or $h \geq 1$, m stays constant since the current density has saturated to $J = J_c$ in the entire sample. The magnetic moment is saturated to $m_s = m(B_a \geq B_p) = J_c a^2 L$ in a slab geometry [40] and $m_s = \pi J_c a^3 L/3$ in a cylinder geometry [92].

The magnetic moments of a thin strip [82, 89] of width $2a$ and length $L >> a$ and a circular disk [40, 86, 93, 94] of radius a, both with thickness $d << a$, in a transverse applied field $\mathbf{B}_a$ are given by

$$m_{strip} = - J_c \, d \, a^2 L \, \tanh h, \tag{45}$$

$$m_{disk} = - J_c d a^3 \frac{2}{3}\left(\cos^{-1} \frac{1}{\cosh h} + \frac{\sinh |h|}{\cosh^2 h} \right), \tag{46}$$

for $0 \leq h < \infty$ with $h = B_a/B_d$, where $B_d = \mu_0 J_c d/\pi$ for a strip and $B_d = \mu_0 J_c d/2$ for a disk. Above the penetration field B_d, the magnetic moment saturates to the values $m_{\text{sat (strip)}} = J_c d a^2 L$ and $m_{\text{sat(disk)}} = J_c d a^3 \pi/3$. In the considered limit $d/a \rightarrow 0$ the transverse moments $m_{\text{strip}}(B_a)$ and $m_{\text{disk}}(B_a)$ saturate only at infinitely large field B_a. The magnetic moments of a strip, disk, and square geometries in the Bean model are very similar when normalized to the same initial slope and same saturation value; the magnetic moment $m(B_a)$ of a strip Eq. (45) then exceeds that of a disk Eq. (46) only by 0.01 $m(\infty)$ [40], and the magnetic moment of a square differs from a disk only by less than 0.002 $m(\infty)$ along the entire curve [40, 76, 80].

A general consequence of the Bean assumption of a field independent J_c is that the virgin curve $m(h)$ with h increased from zero determines the full hysteresis loop of m when h is cycled between $-h_0$ and $+h_0$ [41, 93], where $h_0 = B_0/B^*$ and $B^* = B_p$ for slab and cylinder geometries and B_d for disk and strip geometries,

$$\begin{aligned} m_{\downarrow}(h, h_0) &= m(h_0) - 2m\left(\frac{h_0 - h}{2}\right), \\ m_{\uparrow}(h, h_0) &= -m(h_0) + 2m\left(\frac{h_0 + h}{2}\right), \end{aligned} \tag{47}$$

where $m_{\downarrow}$ and $m_{\uparrow}$ are the branches in increasing and decreasing B_a respectively. Fig. 20 shows magnetization loops of a thin disk calculated from equations (46) and (47) for $h_0 = B_0/B_d$ = 0.75, 1.5, 2.5 and 3. The applied magnetic field is normalized to $B_d = \mu_0 J_c d/2$, while the magnetization is normalized to $m_{\text{sat}}(\text{disk}) = J_c d a^3 \pi/3$.

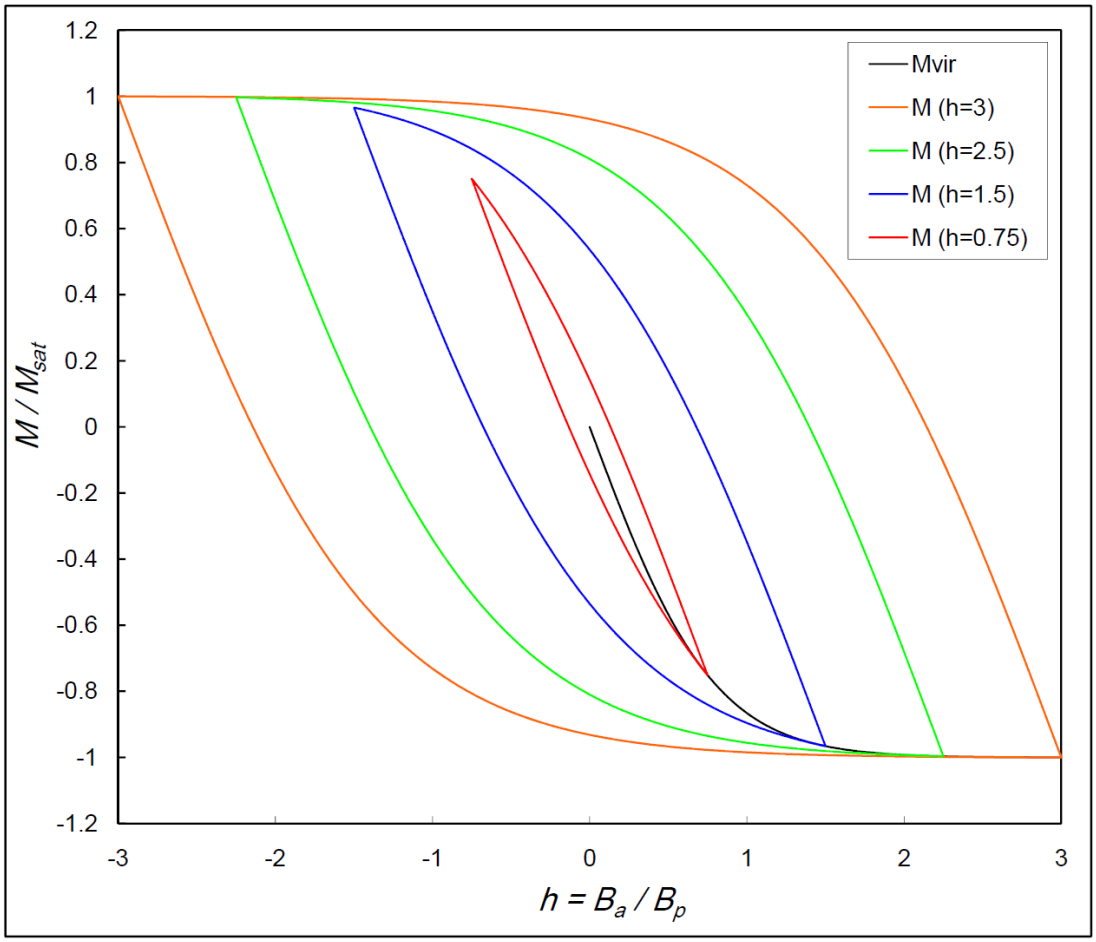

Fig. 20: *Magnetization vs applied field for a thin superconducting disk. The applied field is cycled between + h_0 and – h_0. The curves are for $h_0 = B_0/B_d$ = 0.75, 1.5, 2.5 and 3. The magnetization are normalized to $M_{sat} = J_c\, d\, a^3\, \pi/3$.*

3.2.4. Response to AC fields

Consider a hard type II superconducting sample placed in an applied field of the form $B_a(t) = B_{dc} + B_0 \cos(\omega t)$, where the frequency ω is small enough for the sample to respond quasi-statically. For $B_{dc} = 0$, the response is fully described by the hysteresis curve, where the B field in the sample will show a phase lag φ behind the applied magnetic field B_a. Characteristic of such a hysteretic behaviour is the distorted periodic waveform, where neither B nor M can be expressed as a sinusoidal function of single frequency. The area enclosed within the hysteresis curve is equal to the power loss per cycle, W, and can be written as [95]

$$W = \oint M\, dB_a = \frac{\pi B_0^2}{\mu_0}\chi_1'', \tag{48}$$

where χ_1'' is the imaginary part of the AC susceptibility. The non-linear magnetic response implies that the magnetization in an AC field of frequency ω will contain a response at higher harmonics $n\omega$, and this magnetization will not be in-phase with the applied field. The magnetization of the sample can be generalized to be in the form

$$\mu_0 M(t) = B_0 \sum_{n=1}^{\infty} \left[\chi_n' \cos(n\omega t) + \chi_n'' \sin(n\omega t) \right], \tag{49}$$

where χ_n' and χ_n'' are referred to the real and imaginary parts of the harmonics of the complex susceptibility respectively. The complex AC susceptibility is given by $\chi_n = \chi_n' - i\,\chi_n''$, ($n$ = 1, 2, 3,…) where n = 1 denotes the fundamental susceptibility [96]. The fundamental susceptibility χ_1 has clear physical meaning. The real part χ_1' corresponds to the dispersive magnetic response and reflects supercurrent shielding for superconductors while the imaginary part χ_1'' corresponds to energy dissipation. Eq. (48) implies that the higher harmonics are not responsible for any power dissipations, and hence the fundamental term remains the key component for loss analyses [95]. Bean's model predicts the existence of odd harmonics only because of the symmetry of the magnetization curve, i.e. $M(B_a) = -M(-B_a)$. The susceptibility coefficients χ_n' and χ_n'' can be obtained from:

$$\begin{aligned} \chi_n'(B_0,\omega) &= \frac{\mu_0}{\pi B_0} \int_0^{2\pi} M(t) \cos(n\omega t) d(\omega t), \\ \chi_n''(B_0,\omega) &= \frac{\mu_0}{\pi B_0} \int_0^{2\pi} M(t) \sin(n\omega t) d(\omega t), \end{aligned} \tag{50}$$

The same definition is used when a DC magnetic field is superimposed on the AC field [96]. Usually the χ_n are normalized such that for $B_0 \to 0$ or $\omega \to \infty$ the ideally diamagnetic susceptibility $\chi(0,\omega)$ results [97]. The AC susceptibilities obtained from the critical state model are quasi-static (i.e. χ depends only on the amplitude B_0 but not on the frequency ω).

4. Experimental work and model calculations

To measure the susceptibility and magnetization we used the non-commercial home made SQUID magnetometer. In this chapter there is a brief description to the experimental measurement technique and the method of simulation and fitting the model data to the experimental ones.

4.1. SQUID magnetometers

SQUID is an acronym for Superconducting Quantum Interference Device. These devices are the most sensitive detectors of magnetic flux currently known, where physical quantities which can be converted to the magnetic flux can be measured with an extreme sensitivity. The SQUIDs can be used, for example, for measuring magnetization, magnetic susceptibility, magnetic fields, current and voltage [98].

The principle of operation of the SQUID is based on two physical phenomena, namely Josephson tunnelling and flux quantization. The first key element is the Josephson junction which is characterized by a limited critical current at zero voltage and by switching to the voltage state above a current threshold. The second basic element of the SQUID is a closed superconducting loop for which the flux is quantized in units of the flux quantum $\Phi_0 = h/2e = 2.07 \times 10^{-15}$ Wb.

The theory of different types of SQUIDs is described in detail in the literature [98-100]. SQUIDs are operated as either RF or DC SQUIDs. The prefix RF or DC refers to whether the Josephson junction is biased with an alternating current (RF) or a DC current. The DC SQUID consists of a superconducting loop interrupted by two junctions and is biased by a current source. The output is the voltage across the parallel junctions. On the other hand the radiofrequency (RF) SQUID has only one junction in the loop and the readout uses a resonant LC circuit inductively coupled to the superconducting loop. In both cases the output is a periodic function of the magnetic flux applied to the loop with a period of Φ_0.

SQUIDs can be fabricated from low and high T_c materials. Low T_c SQUIDs are made from niobium (T_c = 9.2 K), while $YBa_2Cu_3O_7$ (T_c = 92 K) is the most frequently used material for high T_c SQUIDs.

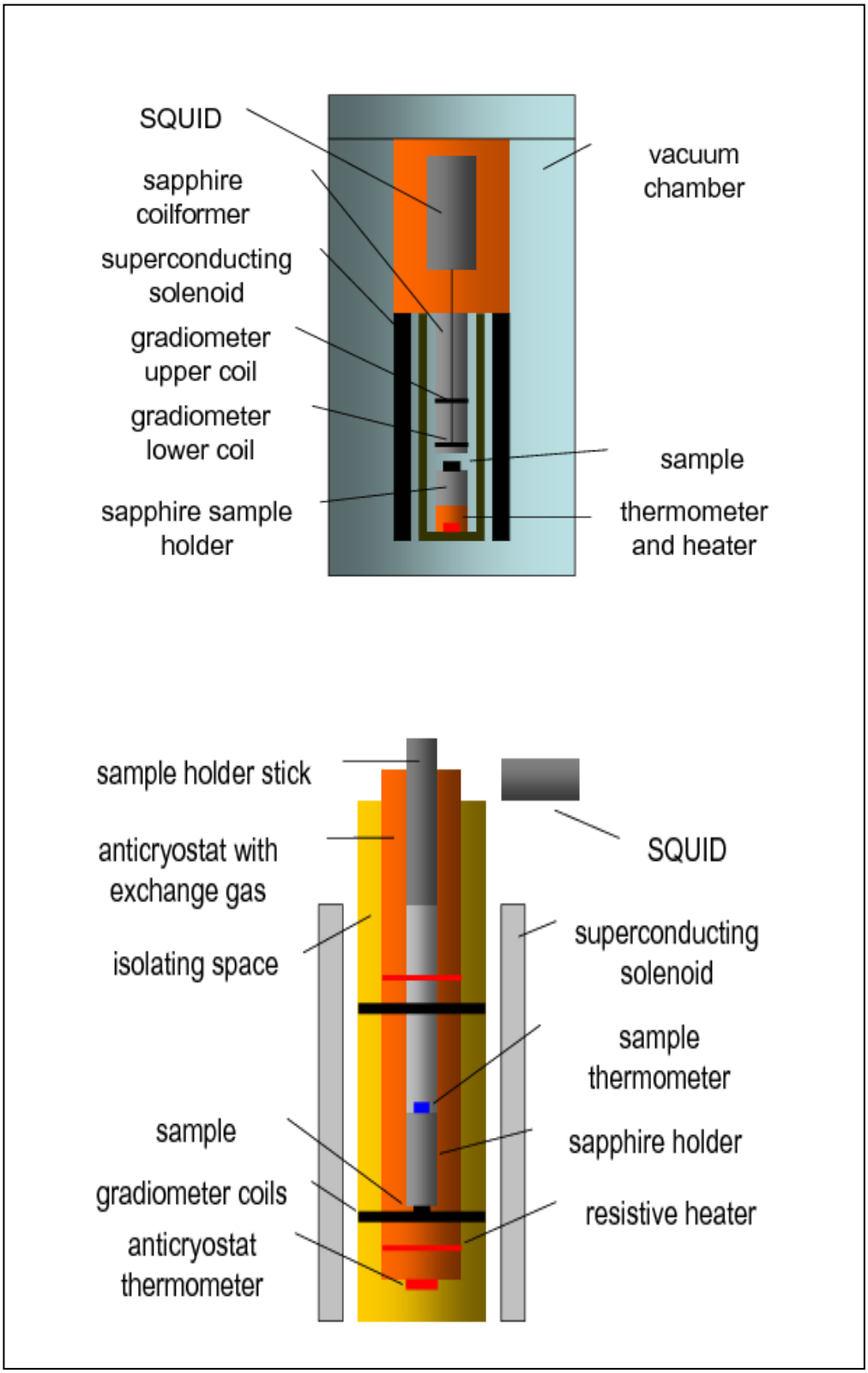

***Fig. 21**: Above: Schematic diagram of the HR magnetometer. Below: Schematic diagram of the SR magnetometer [101].*

In our laboratory we use two non-commercial RF SQUID magnetometers: a standard sensitivity magnetometer (SR) [102] and high sensitivity magnetometer (HR) [103]. The HR magnetometer possesses a more effective screening of an external magnetic field, higher temperature stability, and higher sensitivity. Its disadvantage is more complicated and time-consuming exchange of a sample in comparison with the SR magnetometer. Both magnetometers are fully computer controlled using non-commercial software. Table 2 summarizes the basic parameters of the HR and SR SQUID magnetometers.

Unlike the commercial magnetometers, the sample is static with respect to the detection system and the superconducting magnet [104]. This technique eliminates disturbing effects caused by reciprocating the sample. Furthermore, it allows fast continuous reading of the magnetic moment of the sample, required for harmonic analysis, and accurate sample temperature reading. The response of the sample which is placed in or near one of gradiometer coils can be continuously readout without interference from the stimulus (stimulus is the applied homogeneous field).

The SQUID system contains various building blocks in addition to the SQUID itself (Fig. 21). In the following sections we consider the issues relating to these components for both SR and HS SQUID magnetometers.

Table 2: *The basic parameters of SR and HR SQUID magnetometer.*

	SR	**HR**
Maximum sample size	7 mm	5 mm
Field range	± 25 mT	± 4 mT
	± 2.5 mT	± 400 μT
	± 0.25 mT	± 40 μT
Heat exchange	^{4}He exchange gas	Fibre–glass support, sample is placed in a vacuum
Temperature sweep rate	0.001 – 10 K/min	0.001–10 K/min
Temperature range	4.2 – 300 K	4.2 – 150 K
Frequency range	0 – 100 Hz	0 – 100 Hz
Sensitivity	7.4 pAm^2 Hz$^{-1/2}$	5 fAm^2 Hz$^{-1/2}$

4.1.1. Shielding

SQUID operation can be disturbed by stray low-frequency and RF electromagnetic fields from various sources such as permanent magnets, power cables, transformers, motors, television or communication transmission towers, radars or railways. An interference can also originate from the Earth's magnetic field (about 50 μT) and electronics or computers in the vicinity. In order to take advantage of the high sensitivity of SQUIDs, the sample space must be shielded from external fields.

In the HR magnetometer, three layers of μ-metal shield the whole cryostat and the HR magnetometer. The μ-metal has very high magnetic permeability (80000–100000 compared to several thousands for ordinary steel). This high permeability makes it very effective to screen static or low frequency magnetic fields. SQUID, flux transformer with a gradiometer, solenoid, temperature sensor, heater, and sample are placed in a copper vacuum chamber with an inset superconducting lead can. The shields attenuate external fields at the place of the sample to flux density noise lower than 100 pT $Hz^{-1/2}$.

A cryostat with a SR magnetometer is inserted in a stand made of a magnetically soft iron tube. The SQUID, flux transformer with a gradiometer, solenoid, sample, sample temperature sensor, and so on, are placed in a superconducting lead can. A flux density noise at a sample place is lower than 100 nT $Hz^{-1/2}$.

4.1.2. Flux transformer

In both SR and HR SQUID magnetometers the flux transformers are superconducting made of Nb wire so they do not generate thermal noise and their gain in flux density is noiseless. Transformer consists of a first order gradiometer pickup coil which is exposed to the measured fields, and a SQUID input coil. Two coils forming the gradiometer are wound in opposite direction so a homogeneous field does not induce any net current while field gradient does.

The use of the flux transformer to couple the SQUID with the measured object, instead of direct coupling, increases the sensitivity to magnetic flux density and separates the SQUID from strong static magnetic field which may interfere with the SQUID operation.

4.1.3. Field generation

The field is generated by a low–noise and highly linear field source. It consists of

analogue to digital converters, voltage driven current sources and superconducting solenoid. The superconducting solenoid operates in continuous (non–persistent) mode. The maximum field generated by the superconducting solenoid is ± 25 mT for the SR magnetometer and ± 4 mT for the HR magnetometer.

4.1.4. Residual field

It is easy to detect the residual field in the case of a superconducting sample. If the sample is cooled through its critical temperature the signal of expelled magnetic flux can be detected. The residual field may be compensated by a countervailing current into the solenoid. In case of HR magnetometer, the residual field is typically 145 nT in the sample space. It can vary by about 1 nT between subsequent cooling (He refilling).

4.1.5. Temperature measurement and control

The temperature is regulated and controlled by Cryocon model 34 temperature controller. It automatically regulates the temperature by controlling the amount of heat supplied to a resistive wire (nickel-chrome) heater.

In the SR magnetometer, the sample temperature is controlled in the range from 4.2 to 300 K with temperature stability better than 10 mK and cooling or warming rate from 1 mK/min. The sample is mounted by varnish or Apiezon grease on the bottom surface of a cylindrical sapphire holder. The sapphire is an excellent thermal conductor but an electrical insulator. The sample temperature sensor (GaAlAs diode) is mounted on the upper surface of the holder. The holder is suspended on an electrically and thermally insulating support, which is connected to a stainless tube. This insert is placed in the anti-cryostat in a ^{4}He exchange gas at atmospheric pressure. The anti-cryostat temperature is measured using a Si diode temperature sensor.

In the HR magnetometer, the sample is mounted on a sapphire holder using varnish or grease. The holder is placed in a copper vacuum chamber. Warming is achieved by heating the whole holder, which is placed in a copper block including a Si diode temperature sensor and heater. The temperature controller reads the temperature with a six digit resolution. The relative temperature stability is better than 10^{-5}, and the lowest cooling or warming rate is 1 mK/min. The temperature range is from 4.2 K to 150 K. A temperature response “Lake Shore Curve 10” is used to convert a measured voltage on Si diodes to temperature (see Lake Shore catalogue).

4.1.6. Signal processing

Generation of the applied magnetic field, data acquisition, and signal processing are fully computer controlled, using 16-bit analogue to digital (AD) and digital to analogue (DA) converters and non-commercial software. The SQUID output voltage $m(t)$ and the voltage monitoring current to the solenoid $h(t)$ are simultaneously digitized with 16 bit resolution at a sampling rate of 6.4 kS/s and recorded on a hard disk. Real time data processing yields DC moments of a flux and field and fundamental AC susceptibility. Typically, these values represent a floating average over a time interval of 2.56 s, and together with the sample and control temperature readings are stored every 0.64 s. Digital records of the measured flux and applied field allow later post–processing, particularly for harmonic analysis and reconstruction of magnetization loops.

The experimental complex susceptibility is computed from digitized $m(t)$ and $h(t)$ readings using a discrete fast Fourier transform method (FFT). The nth harmonic of the AC susceptibility is given by

$$\chi_n = \frac{\mu_0 M\left(n f_0\right)}{B_0 \exp\left(ni\varphi\right)}, \tag{51}$$

where f_0 is the fundamental frequency and B_0 is the amplitude of the magnetic field. Complex $B_0 \exp(ni\varphi) \equiv |B(f_0)| \exp(ni \arg(B(f_0))$ takes into account a phase of the Fourier component of the applied field $B(f_0)$, i.e time shift between a Fourier transformation data segment and cosine field. The $M(f)$ and $B(f)$ are Fourier transforms of the SQUID magnetometer signal response and applied field, respectively. The FFT is real time calculated by the digital signal processing from the realisation. While one realisation data are under acquisition, the previous realisation data are processed.

4.2. Model calculations

4.2.1. Generating the magnetization loops

In the previous chapter the virgin magnetic moment curves for different geometries namely slab, cylinder, disk and strip were mentioned, i.e. Eq. (43) to Eq. (46). The model magnetization curves $m(h)$ or rather $m[h(\varphi)]$ were computed using the equations from (43) to (47). The magnetic field $h(\varphi) = h_0 \cos\varphi$ series were computed for

the discrete phase values as a function of $h_0 = B_0/B^*$, where $B^* = B_d$ for disk and strip, and $B^* = B_p$ for cylinder and slab. The values of φ change from 0 to 2π in 1024 steps for each value of h_0. The data length per period (magnetization loop) is 1024, which is the same as for the experimental loop.

4.2.2. Model AC susceptibility

The model susceptibility $\chi(h_0)$ is computed from the model magnetization data $m(\varphi)$ and $h(\varphi)$ series in the same way and for the same number of points per cycle as the experimental susceptibility. The magnetic moments for different geometries i.e. cylinder, slab, disk and strip, give a similar fundamental AC susceptibility, see Fig. 22, and in fact they must because χ_1' shows the Meissner effect and χ_1'' the AC losses [105]. The differences appear only in the higher harmonics as indicated in Fig. 23. This leads to the importance of taking into an account the behaviour of the higher harmonics when choosing a model.

The third harmonic of the model AC susceptibilities is shown in Fig. 23 (on the top). Unlike the fundamental AC susceptibilities, the third harmonic exhibits some

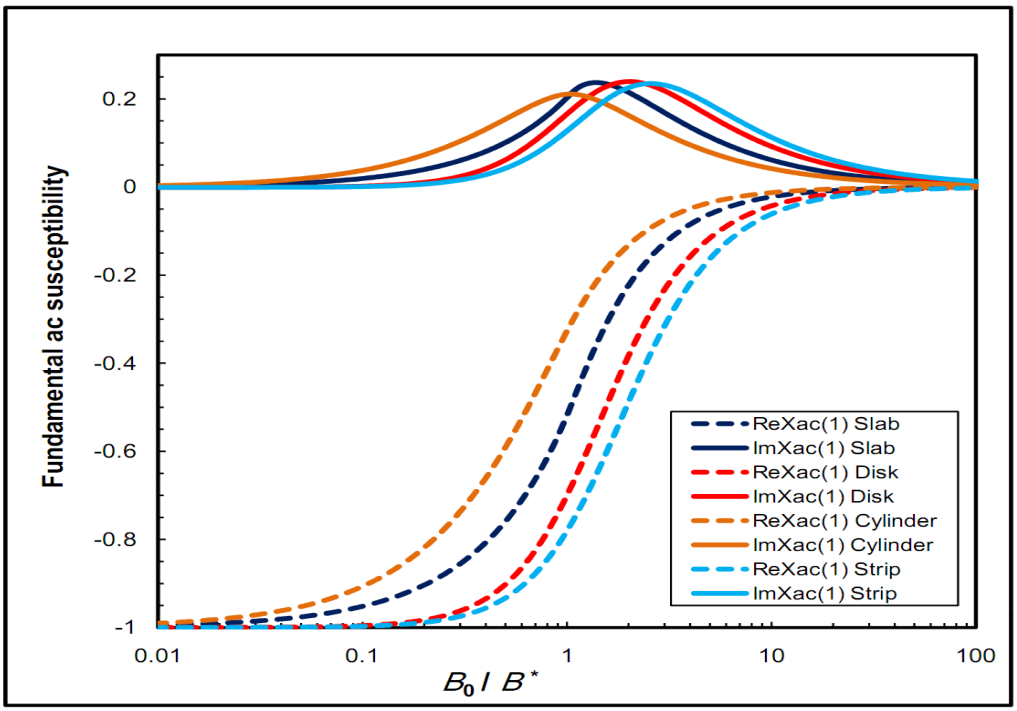

Fig. 22: *Fundamental AC susceptibility for different sample geometries; disk, strip, slab, and cylinder. The four geometries have similar behaviours.*

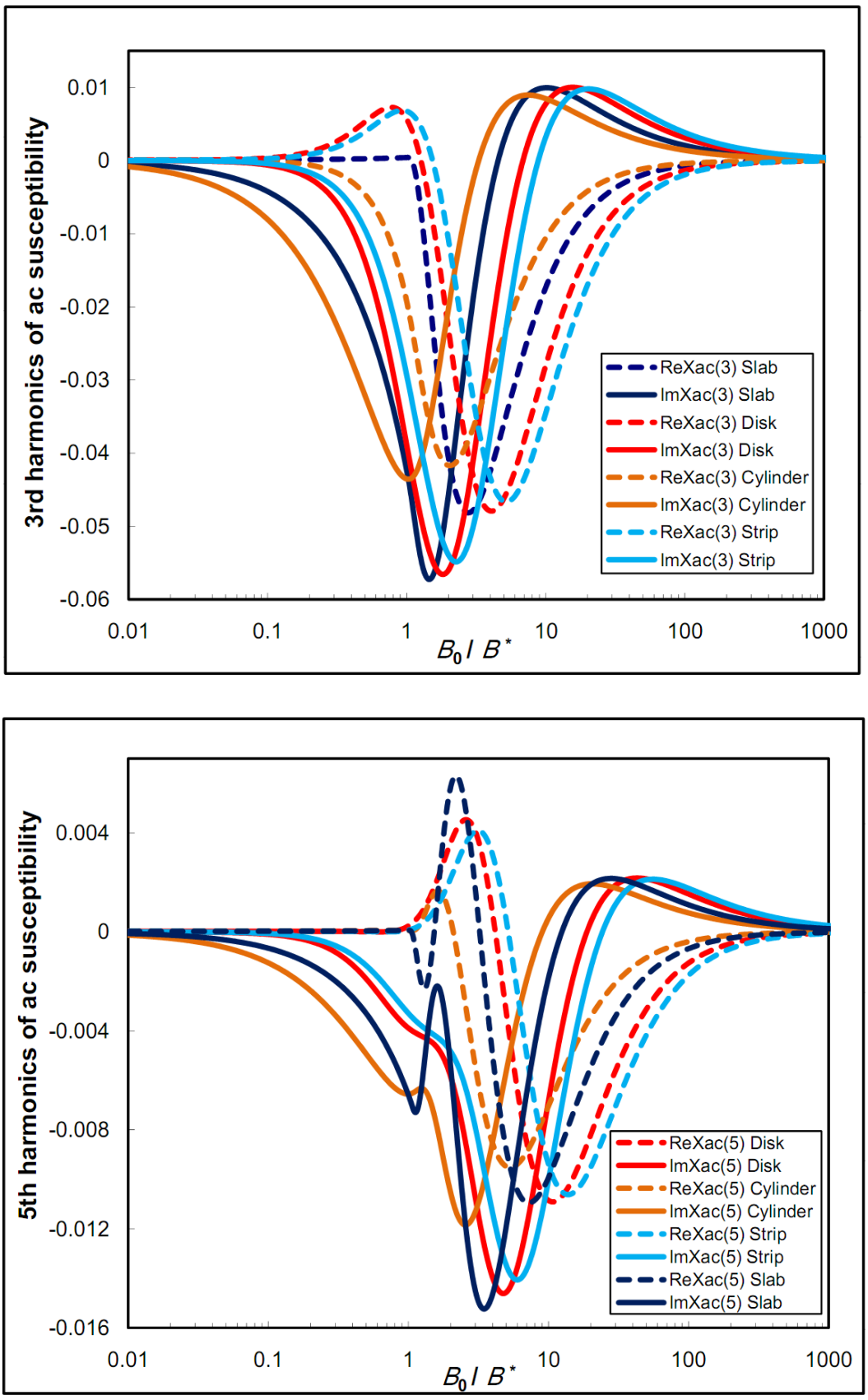

Fig. 23: *The higher harmonics of the AC susceptibility of the disk, strip, cylinder, and slab in the Bean critical state. Third harmonics are on the top and fifth harmonics on the bottom. The solid line is the imaginary part and the dashed line is the real part.*

differences. A hump on the real part of the third harmonic for the model to disk and strip is observed. The hump precedes negative values at decreasing current density (increasing temperature). Such a hump is also seen on the third harmonic of the experimental susceptibility [106-108]. The fifth harmonic of the model AC susceptibilities is shown in Fig. 23 (on the bottom). The hump is present in all four model data, but for the model to cylinder it is much narrower and smaller. In the model to slab it makes small dip (negative values) and turns to positive values to make a higher hump. Another difference is a small kink on the imaginary part of the susceptibility of the model to cylinder and negative values dip and hump on the model to slab. The models to disk and strip are very similar and have the same behaviour and the differences appear only in case of the models to slab and cylinder.

It is worth to mention that within the Bean critical state model, the height of the peak χ''_{1p} in the imaginary part χ''_1 is independent of the amplitude of the applied magnetic field, B_0. Table 3 shows the values of the height of the peaks in different geometries.

Table 3: *Peak values of normalized AC susceptibility.*

Geometry	Slab	Cylinder	Disk	Strip
The height of the peak (χ''_{1p})	0.239	0.212	0.241	0.236

4.2.3. Mapping of model susceptibility to experimental one

We have two data arrays, experimental susceptibility $[T, \chi]$ and model susceptibility $[h_0, \chi]$ to find the critical depinning current density and its temperature dependence. We assume that the critical depinning current density is a monotonically decreasing function of temperature,

$$\frac{J_c(T)}{J_c(0)} = \frac{B^*(T)}{B^*(0)} = \left[1 - \left(\frac{T}{T_c}\right)^m\right]^n . \qquad (52)$$

Model magnetization hysteresis loops and consequently the model susceptibility depends only on the dimensionless ratio h_0. The relation between temperature T and ratio h_0, i.e. the experimental and model susceptibilities, is obtained using the inverse function for equation (52) and multiplying both the numerator and denominator $B^*(T)/B^*(0)$ by B_0,

$$\left(\frac{T}{T_c}\right)_{model} = \left[1-\left(\frac{B_0}{B^*(0)}\frac{B^*}{B_0}\right)^{1/n}\right]^{1/m} = \left[1-\left(c\frac{1}{h_0}\right)^{1/n}\right]^{1/m}. \tag{53}$$

In Eq. (53) we have four free parameters, $c \equiv B_0/B^*(0)$, n, m, and T_c, to match the model and experimental susceptibilities

$$\left\{\left[1-\left(c\frac{1}{h_0}\right)^{1/n}\right]^{1/m}, \chi(h_0)\right\} \leftrightarrow \left\{\frac{T}{T_c}, \chi(T)\right\}. \tag{54}$$

When we find c, n, m, and T_c the zero temperature critical depinning current density can be determined where

$$\begin{aligned} J_c(0)_{disk} &= 2B_0/\mu_0 cd, \\ J_c(0)_{strip} &= \pi B_0/\mu_0 cd, \\ J_c(0)_{cylinder,slab} &= B_0/\mu_0 ca, \end{aligned} \tag{55}$$

and its temperature dependence is given by Eq.(52).

5. Results and discussion

Magnetic measurements using alternating fields have long been recognized as an important tool in the verification of models for pinning and motion of vortices in the mixed state of type II superconductors [41, 62, 109]. However, the physical models to calculate the complex AC susceptibility χ_{ac} still remain controversial. Among the proposed interpretations, the critical state model may be the most used one for explaining the temperature and field dependent characteristics of χ_{ac} especially Bean model. It is probably the most used model for comparison with experimental data. In this chapter we will discuss our experimental results.

This chapter is divided into three parts. In the first part we will discuss the application of Bean critical state model (BCSM) to a conventional superconductor in the form of thin film in perpendicular applied magnetic field, i.e. Nb thin films. In the second part we will apply the BCSM to unconventional superconductor YBCO thin film in a perpendicular applied magnetic field. In the third part we will apply the BCSM to a bulk unconventional superconductor YBCO.

5.1. Critical state response in Nb Thin Films

Niobium has the highest critical temperature of the elementary superconductors: 9.2 K. Also it has the largest London penetration length, λ_L of any element. It is one of only four elementary superconductors which are type II thus it may sustain the mixed state with quantized vortices. The Nb thin films are starting material for superconducting electronics. The SQUIDs, chips for Josephson voltage standard, electromagnetic cavity resonators, filters, etc. are made by lithographic processes on these films.

5.1.1. Dimensions and preparation of the sample

The Nb thin film of thickness of 250 nm was deposited by DC magnetron sputtering in Ar gas on 400 nm thick silicon-dioxide buffer layer which was grown by a thermal oxidation of silicon single crystal wafer [110]. The film is poly-crystalline with texture of a preferred orientation in the (110) direction and is highly tensile. Grain size

is about 100 nm. The square samples of 5 mm × 5 mm in dimensions were cut out from a 3-inch wafer.

5.1.2. Meeting the model assumptions

Our Nb thin film sample fulfils the model assumptions in the case of disk and strip. For a model disk: a) The film thickness, d = 250 nm, is larger than the flux penetration length for Nb, $\lambda(0)$ = 40 nm, thus the first Clem and Sanchez condition [86], $d \geq \lambda$ is fulfilled. However, λ may become larger than the thickness near T_c. Considering Gorter-Casimir or Ginzburg-Landau model for temperature dependence of λ, the $\lambda(T) \approx d$ for $T \approx$ 0.99-0.999 T_c. However, in this case, the second Clem and Sanchez assumption on the two-dimensional screening length Λ is fulfilled as $\lambda^2 << a\,d/2 \approx 0.5 \times 2.5$ mm × 250 nm, i.e. $\lambda << 18\ \mu$m and a is the radius of the disk. b) The AC susceptibilities were measured in a low frequency field for frequencies from 1.5625 up to 12.5 Hz. As the susceptibilities do not change with a frequency, the field may be considered quasi-static.

On the other hand the important condition for strip is that $d << a$ [82, 89] (where d = 250 nm << a = 2.5 mm, a is the half width of the strip). When $d >> \lambda$ the current is completely pure Meissner current and flows in two surface layers of thickness λ leaving the central free region current free while for $d < \lambda$ the current is vortex current, which is nearly constant over the thickness d. Both cases are allowed.

5.1.3. AC susceptibility and the model validity

The fundamental AC susceptibility and the 3rd and 5th harmonics are shown in Fig. 24. The experimental data have been fitted to the 2D BCSM to disk and strip. The experimental data have been plotted as function of the reduced temperature, T/T_c, while the model data have been plotted against, $1-(cB_d/B_a)^{3/2}$, using reduced temperature defined in Eq. (53). Both models predict that the transition is completed at reduced temperature, $T/T_c \approx 0.985$, in the AC field of $B_0 = 10\ \mu$T. Hence we have scaled the model susceptibility (the fundamental and the 3rd and 5th harmonics, i.e. the vertical scale, while the horizontal scale, i.e. reduced temperature, was left as it is) by a factor of s = 0.97, $\chi \rightarrow s\chi$, to fit experimental data. This vertical scaling has no influence on an estimated critical current density and its temperature dependence since these are given by concord in temperature axis.

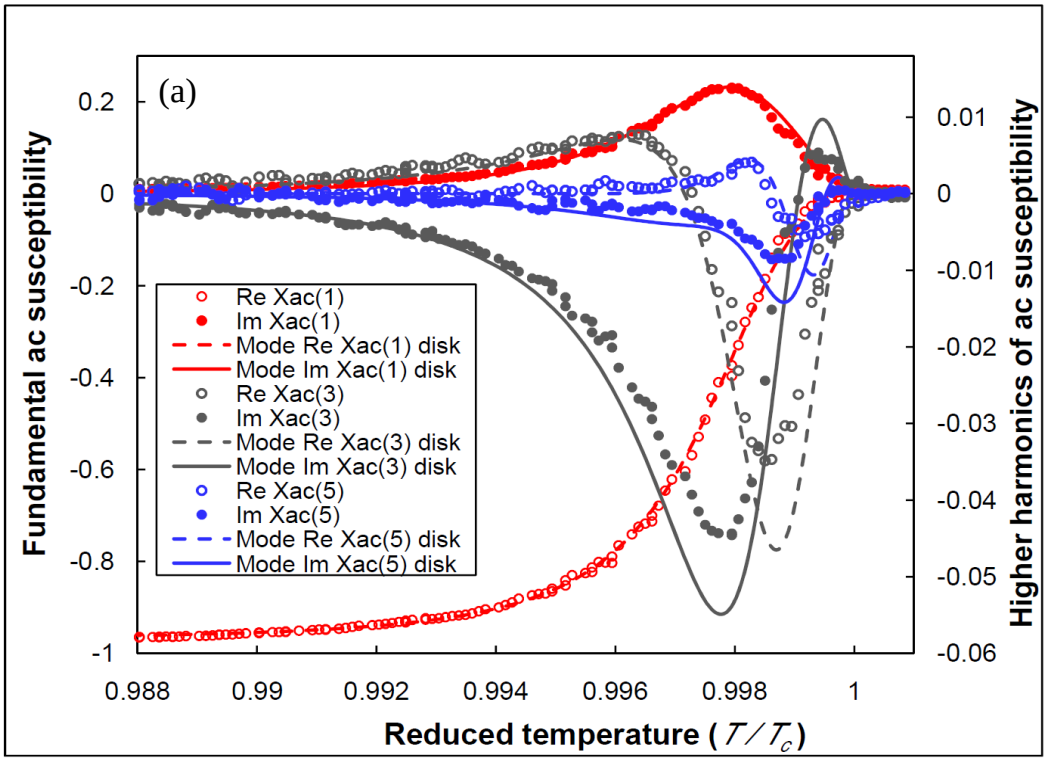

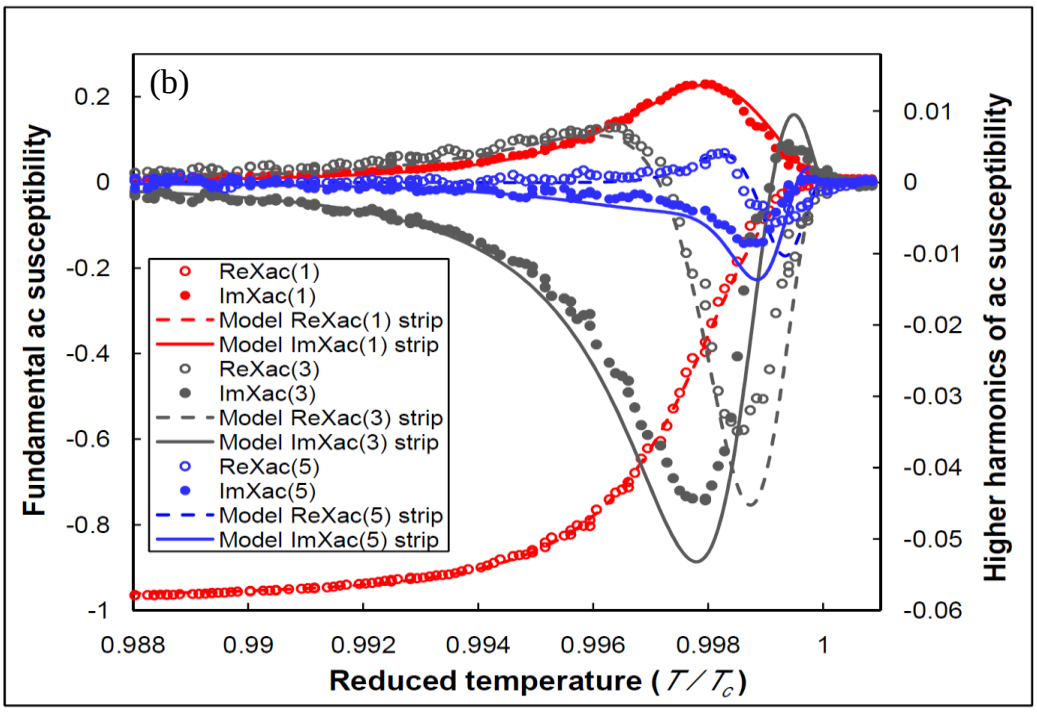

***Fig. 24*:** *The fundamental AC susceptibility and third and fifth harmonics as a function of temperature for B_0= 10 μT, frequency 1.5625 Hz, zero DC field, and cooling rate 0.1 K/min. The marks are experimental data. The curves are susceptibilities calculated on the basis of the 2D BCSM model to disk (a) and strip (b). In both models the data (χ_1, χ_3 and χ_5) are scaled by a factor s = 0.97, i.e. $\chi \rightarrow s\chi$.*

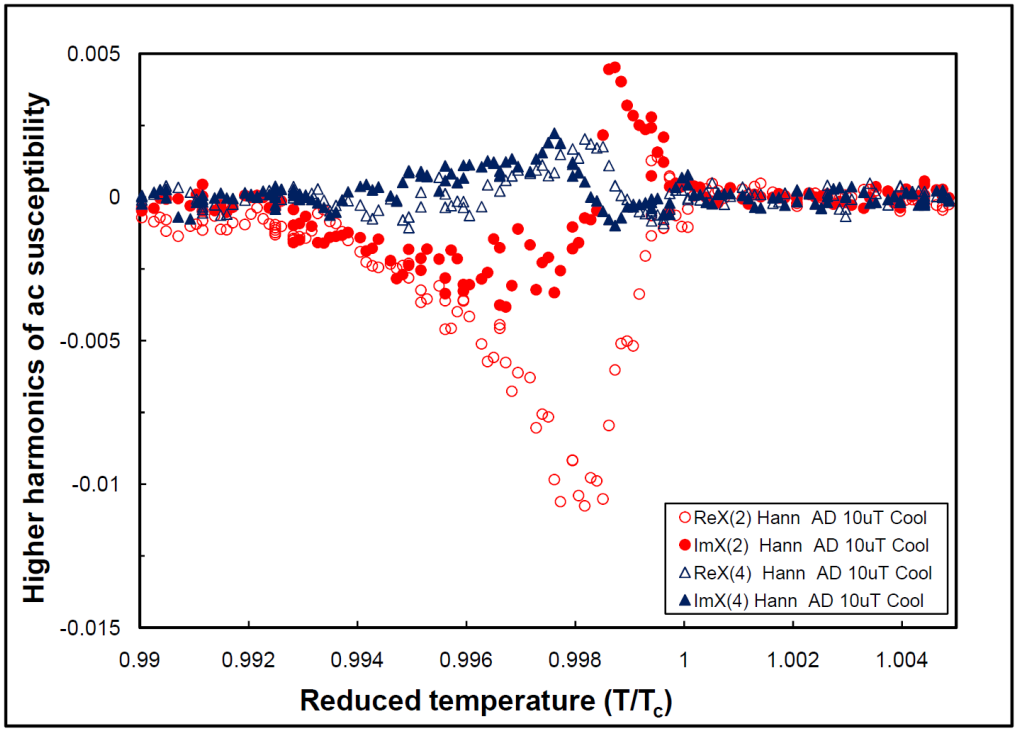

Fig. 25 : *Temperature dependence of the real and imaginary parts of even (2nd and 4th) harmonics of complex AC susceptibility.*

The hysteretic nonlinear relationship between the applied magnetic field and the magnetization due to the existence of the flux pinning is reflected in the appearance of the higher harmonics [41, 61, 62, 96, 111]. According to BCSM the symmetry of the magnetization hysteresis curves is odd, i.e. $M(B_a) = -M(-B_a)$. Hence only the odd harmonics can be generated. In Fig. 24 we can see that both the model to strip and disk successfully describe the experimental data, specially the higher harmonics.

The generation of even harmonics has not been reported in well fabricated conventional superconductors [112]. The probable reason is that for this generation to be noticeable, the following conditions must be satisfied: (1) the critical current is field dependent, (2) DC and AC fields are of the same order of magnitude, and (3) the total field is much greater than B_{cl}. Since B_{cl} is rather larger for conventional materials except near T_c, the generation of even harmonics may not be observable with the small AC field amplitudes typically used in this type of experiment. However, we detect even harmonics in our measurements [106, 107]. Fig. 25 depicts the even harmonics of the AC susceptibility. The second harmonic is of the level of 10^{-2} and the forth harmonic is of the level of 10^{-4}. The second harmonic is small compared to the third harmonic,

while the forth is small compared to the fifth harmonic. Their appearance may be attributed to residual ambient DC field [96].

Cole–cole plot

In Bean model the penetration field B_d is proportional to the critical current density $J_c(T)$ with the proportionality coefficient being determined by the geometrical length scales of the sample. Thus, the reduced field $h_0 = B_0/B_d \propto J_c^{-1}$ with a proportionality constant containing geometrical factors. If the model is tested by plotting the imaginary part χ_1'' versus the real part χ_1', the reduced field h_0 can be treated as a curve parameter within $0 \leq h_0 < \infty$. Any specific sample shape then yields a characteristic curve in the Cole-Cole plot. Hence, there should be no difference whether the experimental data were obtained by a variation of the applied field B_a or temperature T.

The method is demonstrated in Fig. 26, where the imaginary part of the fundamental AC susceptibility χ_1'' is plotted versus the real part χ_1' for experimental

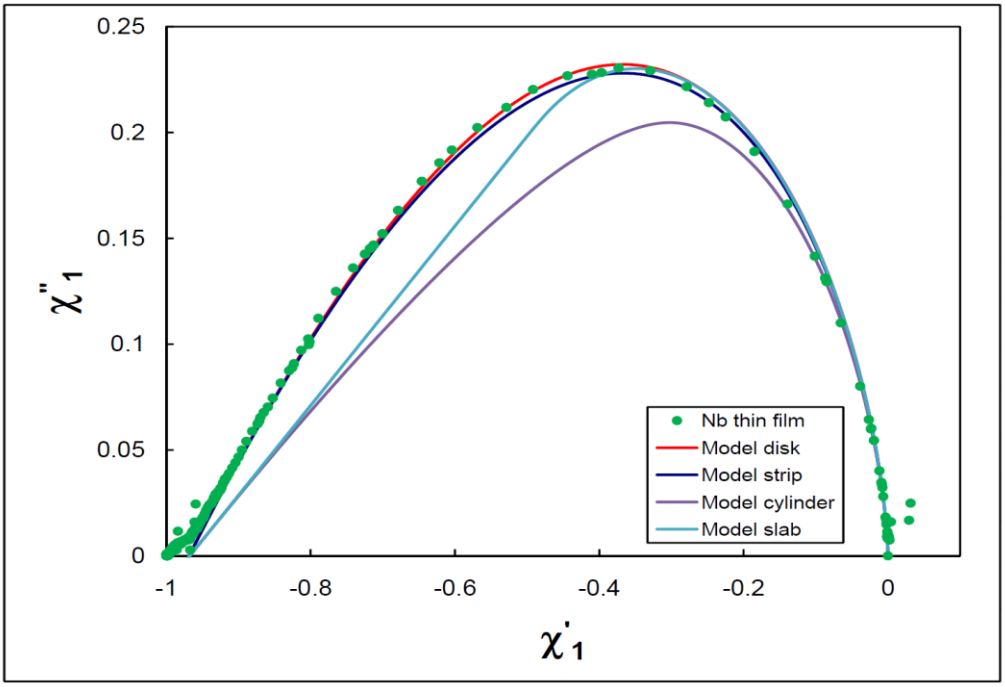

Fig. 26 : *Cole-Cole plot as obtained from the temperature dependence of the AC susceptibility at B_0 = 10 μT, frequency 1.5625 Hz, and zero DC field. The corresponding theoretical predictions of Bean model to the disk, strip, cylinder and slab are added. The model susceptibility data have been scaled by a factor s = 0.97.*

data of a square Nb sample. In addition, the prediction of the Bean model for an infinite cylinder and slab geometries in a longitudinal magnetic field is included in the figure for comparison. The data are characterised by a dome shape. It is clear that the small part of the experimental data near $\chi_1' = -1$ does not belong to the critical state behaviour, hence all theoretical model data are scaled by ratio, s = 0.97, i.e. $\chi \rightarrow 0.97\,\chi$, as explained above. The curves at the high temperature end ($\chi_1' \rightarrow 0$) are found to be independent of the sample shape. There is, however, a significant difference at the low temperature end $(\chi_1' = -1)$. Only the model to disk and strip predict the experimental data. The maximum height of the χ_1'' in the experimental data is in agreement with the theoretical predictions of the model to disk and strip. The models to cylinder and slab fail to describe the data obtained for the Nb thin film sample.

Critical current evaluation

The actual temperature dependence of the critical current density can be determined by best fitting to χ_1' and χ_1'' with aiding of the third and fifth harmonics. The fitting is shown in Fig. 24. It was found that both models to disk and strip can fit the experimental data well with the fitting parameters m = 1, n = 3/2 and T_c = 8.972 K (we note that our temperature sensor is not calibrated to such absolute accuracy even if the temperature resolution is of the order of ppm). Other parameters can be found in Table 4. The estimated temperature dependence of the critical current density is $J_c(T) = J_{c0}\,(1 - T/T_c)^{3/2}$ with zero temperature critical depinning current density J_{c0} = 3.32 × 10^{11} A/m^2 and 4.62 × 10^{11} A/m^2 for disk and strip geometry, respectively, at B_0 = 10 μT, frequency f = 1.5625 Hz, and zero DC field. These values sound reasonably. The zero temperature critical current is $I_c(0) = 2\,J_{c0}\,a\,d \approx 0.42$ kA and 0.53 kA for the model to disk and strip, respectively, where 2a is the width of the sample and d is its thickness. Using the temperature dependence given by Eq. (52), the critical depinning current is $I_c(4.2) \approx 161$ A and 206 A for disk and strip geometries respectively at liquid ^{4}He temperature.

The difference in calculations of the critical current using 2D Bean model to strip and disk is nearly 22%. Since our sample is square and the difference between the virgin magnetization curve of square and disk geometry is smaller than the difference between square and strip geometry [40, 76, 80, 94], it is expected that the 2D Bean model to disk should give better results than the 2D Bean model to strip.

5.1.4. AC field dependence of the AC susceptibility

The AC field dependence of the fundamental AC susceptibility

The fundamental AC susceptibility as a function of temperature at various AC field amplitudes (B_0 = 1, 2, 5 and 10 μT), for frequency f = 1.5625 Hz and zero DC field, is shown in Fig. 27. As discussed previously the model susceptibility data were scaled by a factor s = 0.97 to fit the experimental data. A typical trend towards a shift of the maximum χ''_{1p} in χ''_1 to lower temperatures for increasing field amplitudes can be noticed clearly. Within the Bean model, χ''_{1p} is attained at a temperature T_p, at which the applied field amplitude B_0 approaches the penetration field B^* for the corresponding sample geometry, i.e. for $B_0 = B_d(T_p)$. The scaling of B_d with $J_c(T)$, which is expected to be a monotonically decreasing function of temperature, immediately leads to the observed shift of T_p to lower values. Once the applied field exceeds B_d at a fixed temperature or T exceeds T_p at a constant B_0, the magnetic moment of the sample approaches saturation and the susceptibility decreases, respectively. Another general trend found for the susceptibility curves presented in Fig. 27 is the developing asymmetry of the χ''_1 peaks towards lower temperatures for increasing amplitudes B_0 accompanied by a corresponding broadening of the $\chi'_1(T)$ transition. This behaviour reflects the temperature dependence of the critical depinning current density and dependence of the susceptibility on B_a/B_d.

There is another point worth mentioning. Within the BCSM, the height of the χ''_1 peak, χ''_{1p}, is independent of the AC field amplitude B_0. For disk χ''_{1p} = 0.241 at reduced field, $h_0 = B_0/B_d$ = 1.94, while for strip χ''_{1p} = 0.235 at h_0 = 2.568 according to the calculations performed using equations from (45) to (47). Using this criterion the model fits the experimental data for B_0 = 10 and 5 μT. For B_0 < 5 μT, the χ''_{1p} is smaller than the theoretically predicted values and disappears with decreasing amplitude of the AC field. This is demonstrated more quantitatively in Fig. 28, where the values of χ''_{1p} are plotted versus the amplitude of the applied magnetic field, B_0. We can notice that there is an increase on χ''_{1p} values for small applied field amplitudes B_0 followed by saturation like behaviour. It is important to mention that any experimental test of theories based on the Bean model should be performed applying amplitudes B_0

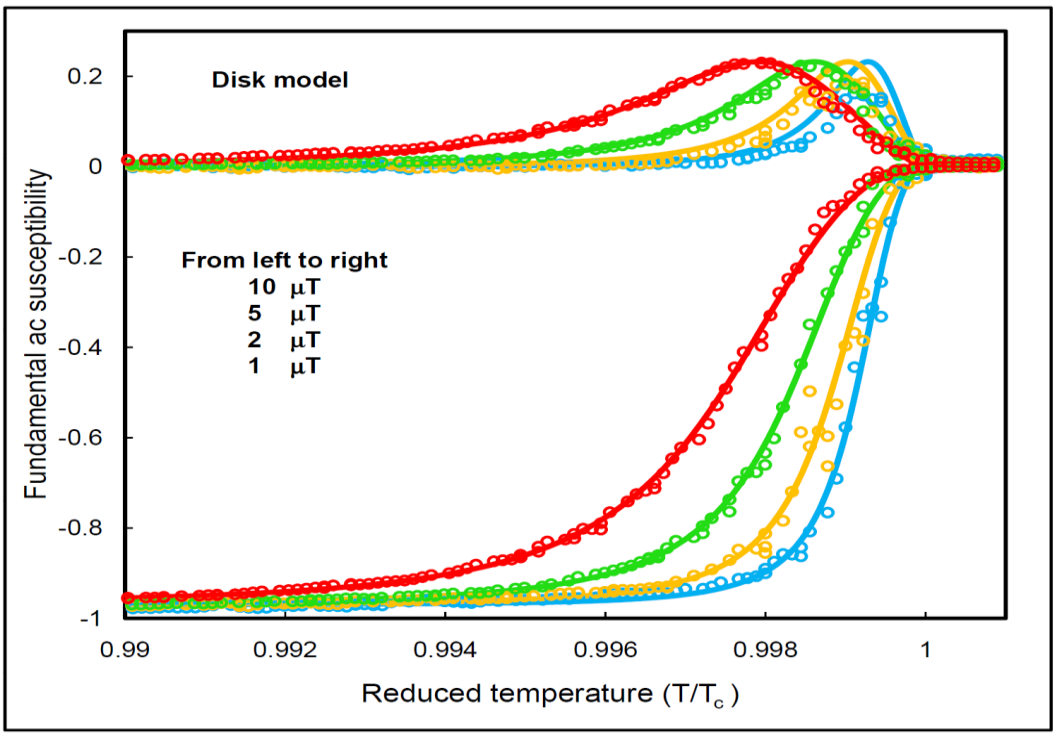

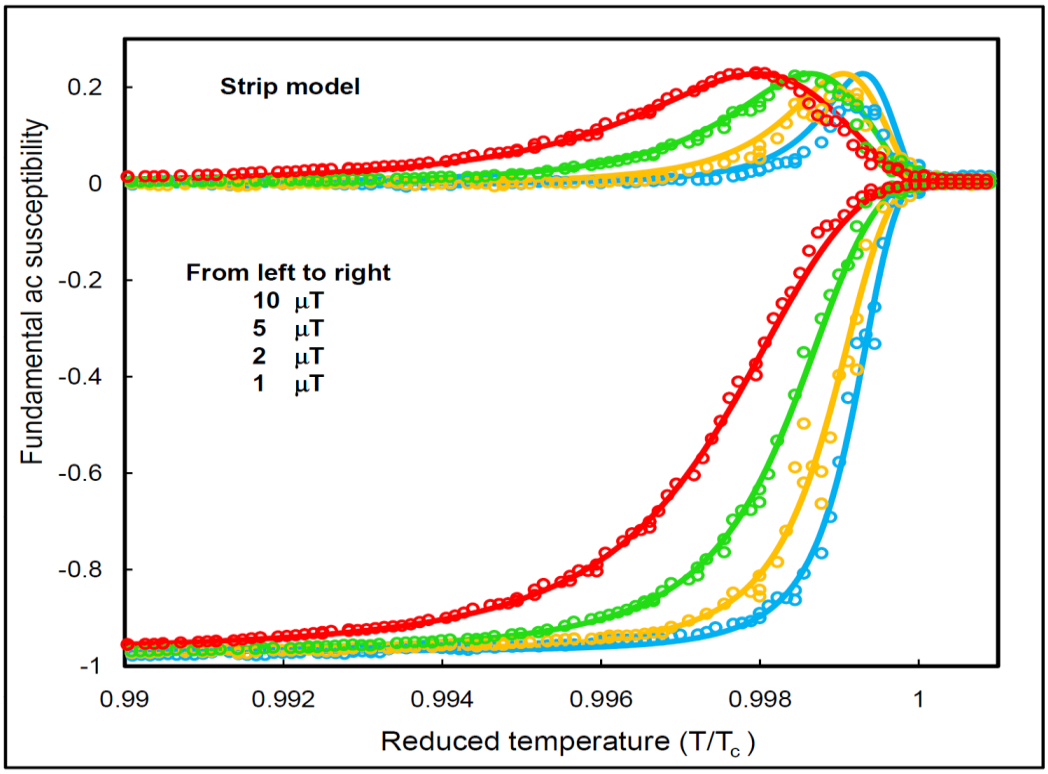

***Fig. 27**: Temperature dependence of the fundamental AC susceptibility for different AC field amplitudes measured with frequency f = 1.5625 Hz and cooling rate 0.1 K/min in zero DC field. The marks are the experimental data while curves are susceptibility calculated on basis of 2D BCSM to disk (top) and strip (bottom). Model susceptibility data have been scaled by a factor s = 0.97, i.e. $\chi \rightarrow s\chi$.*

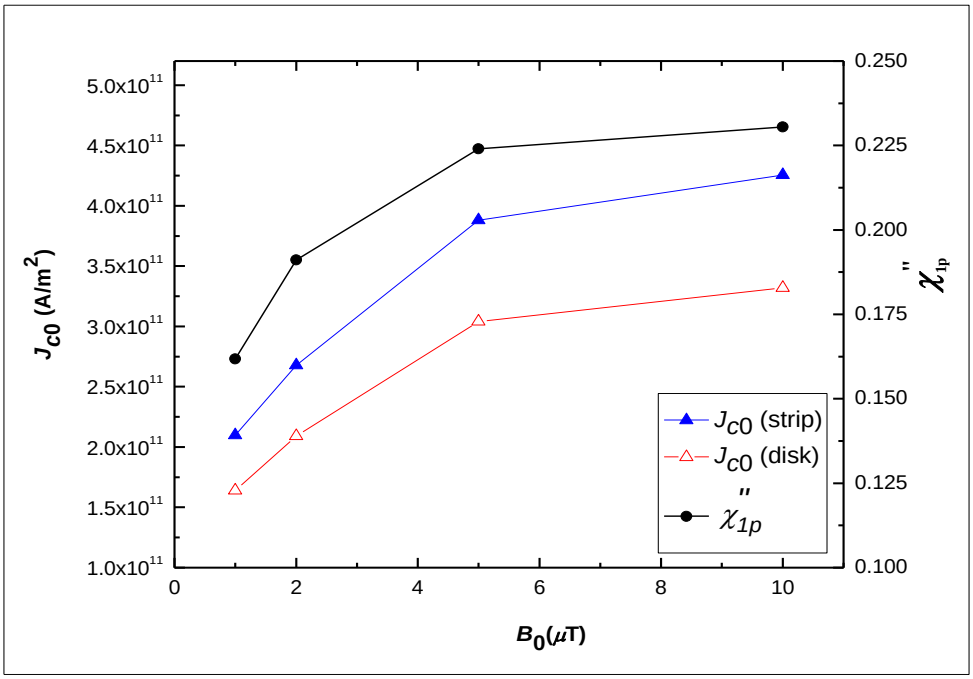

Fig. 28 : *The variation of the maximum height of* χ_1'' *and the calculated zero temperature critical current density with the amplitude of the applied magnetic field.*

Table 4: *Parameters as a function of the amplitude of the applied magnetic field* B_0.

Bean model	B_0 (μT)	c	J_{c0} (A/m^2)	I_{c0} (A)	I_c(4.2) (A)	T_c	T_p	χ''_{1p}
Disk	10	1.92×10^{-4}	3.32×10^{11}	415	161	8.972	8.954	0.231
	5	1.05×10^{-4}	3.04×10^{11}	380	148	8.977	8.963	0.224
	2	6.08×10^{-5}	2.09×10^{11}	262	102	8.982	8.973	0.191
	1	3.88×10^{-5}	1.64×10^{11}	205	80	8.988	8.980	0.162
Strip	10	2.35×10^{-4}	4.26×10^{11}	532	206	8.972	8.954	0.231
	5	1.29×10^{-4}	3.88×10^{11}	485	188	8.977	8.963	0.224
	2	7.47×10^{-5}	2.68×10^{11}	335	130	8.982	8.973	0.191
	1	4.77×10^{-5}	2.10×10^{11}	262	102	8.988	8.980	0.162

corresponding to χ''_{1p} values on the saturation regime. Applying this criterion to our results, the models are valid for AC field amplitudes, $B_0 \geq 5$ μT. The increase of χ''_{1p} with increasing the applied magnetic field amplitude B_0 will be investigated in the next subsection.

The values of T_c, c, T_p, χ''_{1p}, and the calculated J_{c0}, for set of amplitudes B_0 are listed in Table 4. As the field is increased, the critical temperature T_c shifts down, in agreement with expected suppression of the superconductivity by the applied magnetic field. At the same time, the transition region broadens and the absorption peak shifts to

lower temperature. The values of the critical current and critical current density in Table 4 show that the difference between the results of the 2D Bean model to disk and strip is nearly 22% for $B_0 = 10\ \mu$T. As explained previously it is expected that the 2D model to disk should give better results than 2D model to strip.

AC loss mechanism

When an AC magnetic field is applied, the sample is taken through a complete hysteresis loop within time period $t = 1/f$. Because the hysteretic loss is proportional to the area of the magnetization loop, the peak in χ_1'' and the changes in the peak height of χ_{1p}'' can be explained by considering the magnetization loops at different temperatures. In Fig. 29, we plot the magnetization loops at four reduced temperatures $T/T_c = 0.993$,

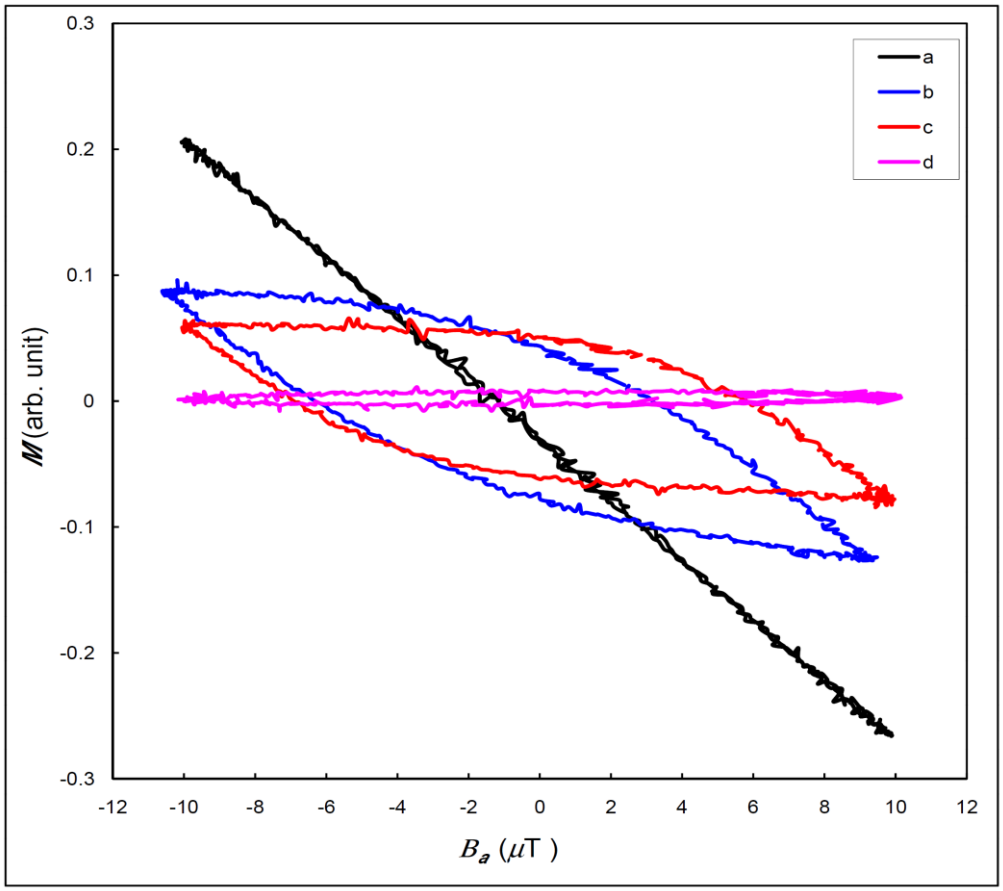

***Fig. 29**: The magnetic moment of Nb sample measured in $B_0 = 10\ \mu$T, $f = 1.5625$ and zero DC field. The letters from a to d are corresponding to reduced temperatures $T/T_c = 0.993$, 0.998, 0.999 and 1.018. These reduced temperatures are corresponding to $T/T_p = 0.995$, 1, 1.001 and 1.020 respectively.*

0.998, 0.999 and 1.018 for f = 1.5625 Hz, B_0 = 10 μT, and zero DC magnetic field. These reduced temperatures are corresponding to T/T_p = 0.995, 1, 1.001 and 1.020 respectively. For T/T_c = 0.993, the applied AC field causes shielding currents to flow on the surface of the sample and a line to be traced out in the $M - B_a$ plane (Fig. 29 curve a). This means that there is no hysteresis, $\chi_1'' = 0$ and the current density $J < J_c$. When T is somewhat below T_c, J_c has decreased and shielding currents have to flow within the sample. The hysteresis loop in the $M- B_a$ plane has an area associated with it, and $\chi_1'' > 0$. The losses and χ_1'' attain their maximum values after supercurrents and penetrated flux reach the centre of the sample at $T \approx T_p$ (curve b in Fig. 29). When $T > T_p$, the magnetization loops start to saturate (see curve c in Fig. 29), which is theoretically predicted by Bean model [86, 93]. As T approaches T_c, J_c approaches 0 and the magnetization loops have collapsed, hence there is no area to the loops, no hysteretic loss and $\chi_1'' = 0$ (curve d in Fig. 29). This interpretation is in accordance with the expectations of the critical state model, in which all energy losses are hysteretic and frequency independent.

When the applied magnetic field is not large enough, it is expected that the flux and current front cannot penetrate to the centre of the sample, since the total displacement of the vortices in each cycle is proportional to the local amplitude of the AC field. There is a threshold value of B_0, below which the vortices will not be able to leave the pinning centres [41, 113, 114]. In this situation each vortex will oscillate inside its effective pinning potential well rather than jumping from one to another. Therefore the transverse moments will not saturate. These concepts can be explored in Fig. 30, where the AC magnetic loops are plotted at different temperatures in the transition regime for different AC applied magnetic fields which were shown in Fig. 27 and Fig. 28. At B_0 = 10 and 5 μT the magnetic flux and current front penetrate to the centre of the sample at $T \approx T_p$. The height of χ_1'' in this case is in agreement with the Bean model prediction, and the AC losses reach its maximum. For B_0 = 2 and 1 μT, it is clear from Fig. 30, that the magnetic moment does not reach saturation. This can explain the decreasing of χ_{1p}'' and J_{c0} with decreasing the AC magnetic field amplitude, B_0, which were indicated in Fig. 28. Since the critical state model deals with macroscopic magnetization, supercurrent, flux density and field, the decrease in both quantities χ_{1p}'' and J_{c0} is clearly understood. It is worth to mention that, in Fig. 30, we

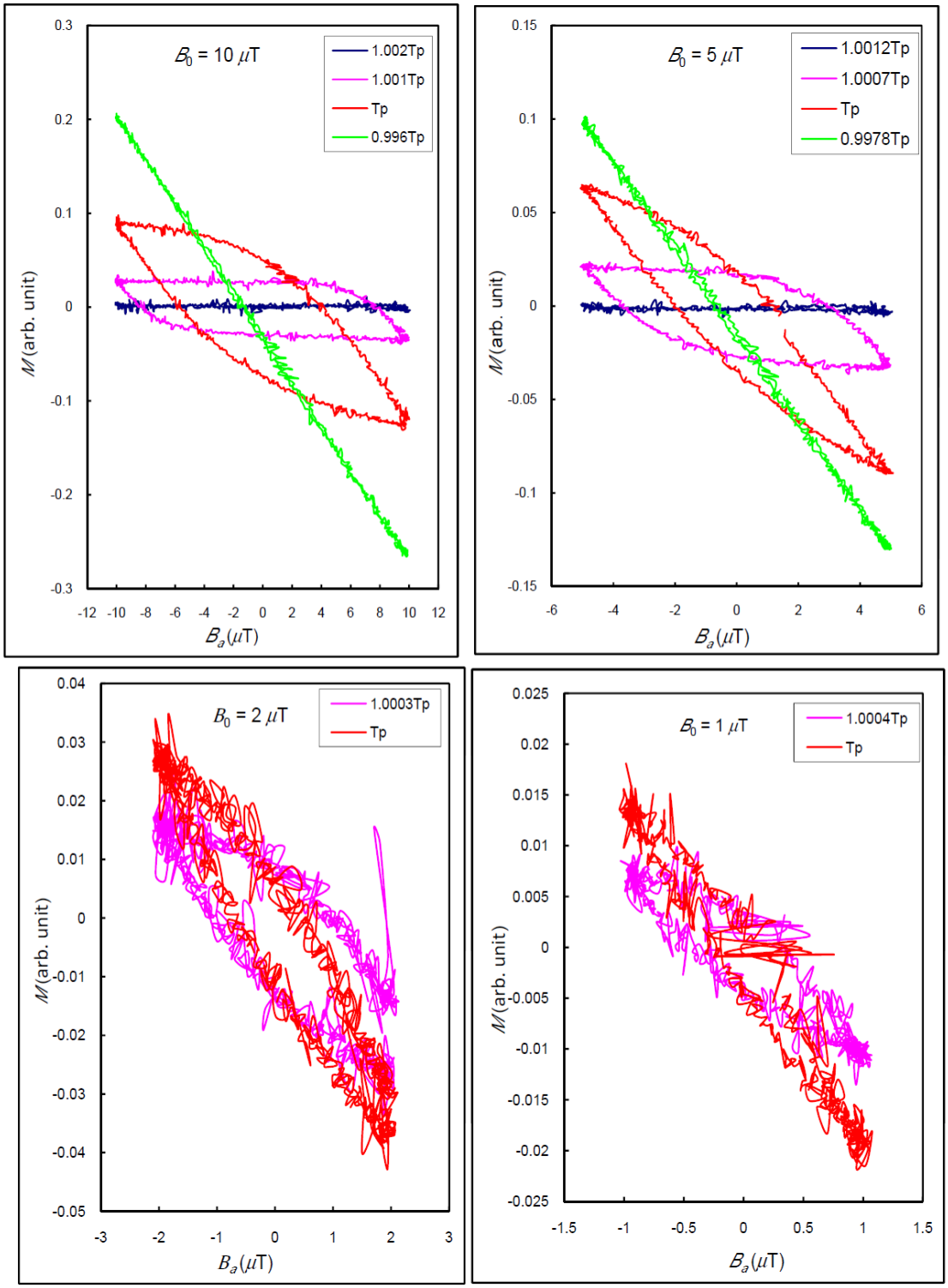

Fig. 30: *Hysteresis magnetization loops for AC fields B_0 = 10, 5, 2 and 1 μT at frequency f = 1.5625 Hz and zero DC field. For B_0 = 2 and 1 μT, the magnetization loops corresponding to Meissner and normal state are omitted because the background noise is high.*

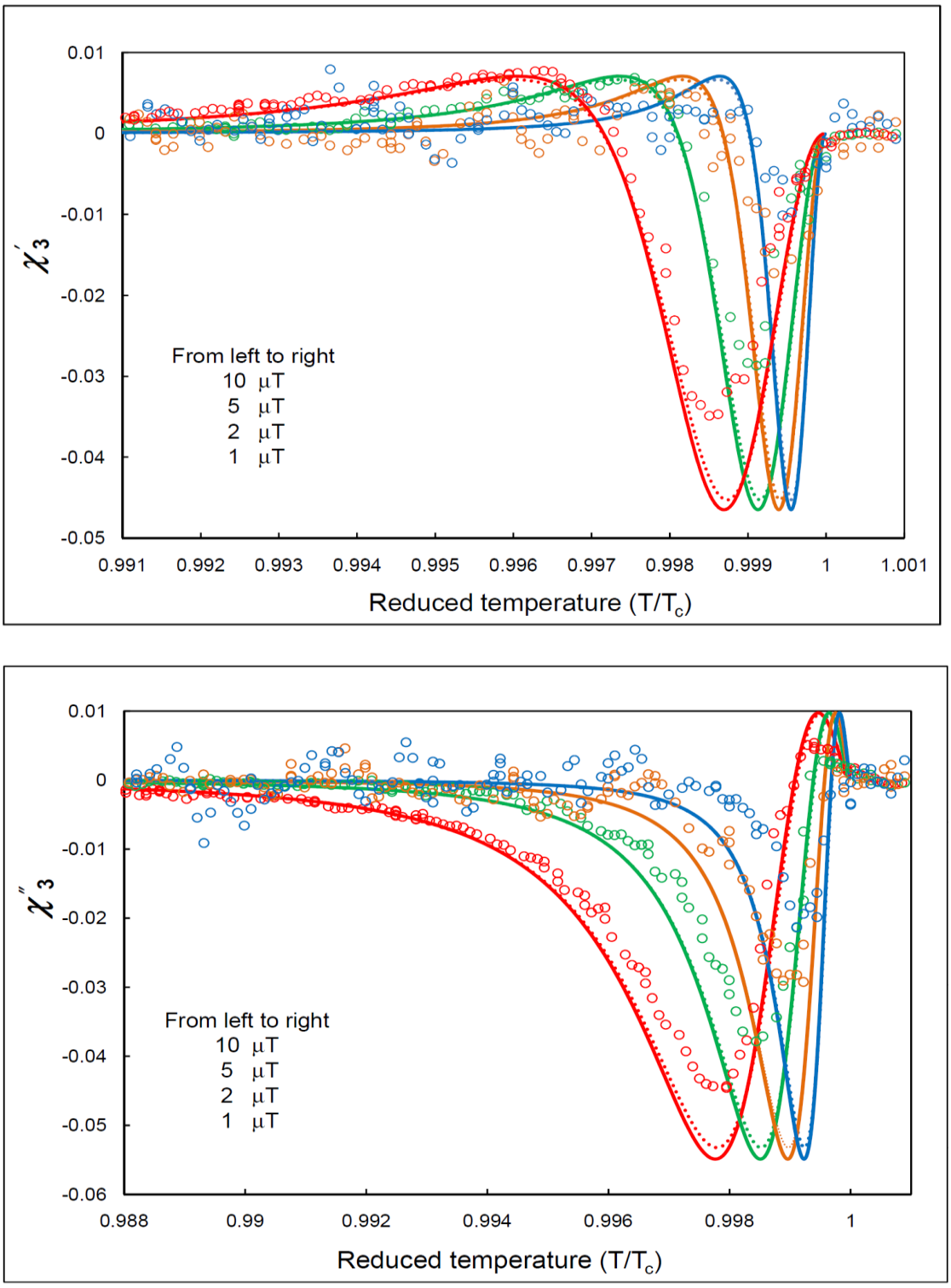

Fig. 31: *The AC field dependence of the experimental and theoretical 2D BCSM model data of third harmonic of AC susceptibility. The marks are the experimental data, while dashed and solid lines are the model to strip and disk data respectively. The sample has been measured in zero DC field, f = 1.5625 and cooling rate 0.1 K/min. Model susceptibility data have been scaled by a factor s = 0.97, i.e. $\chi \rightarrow s\chi$.*

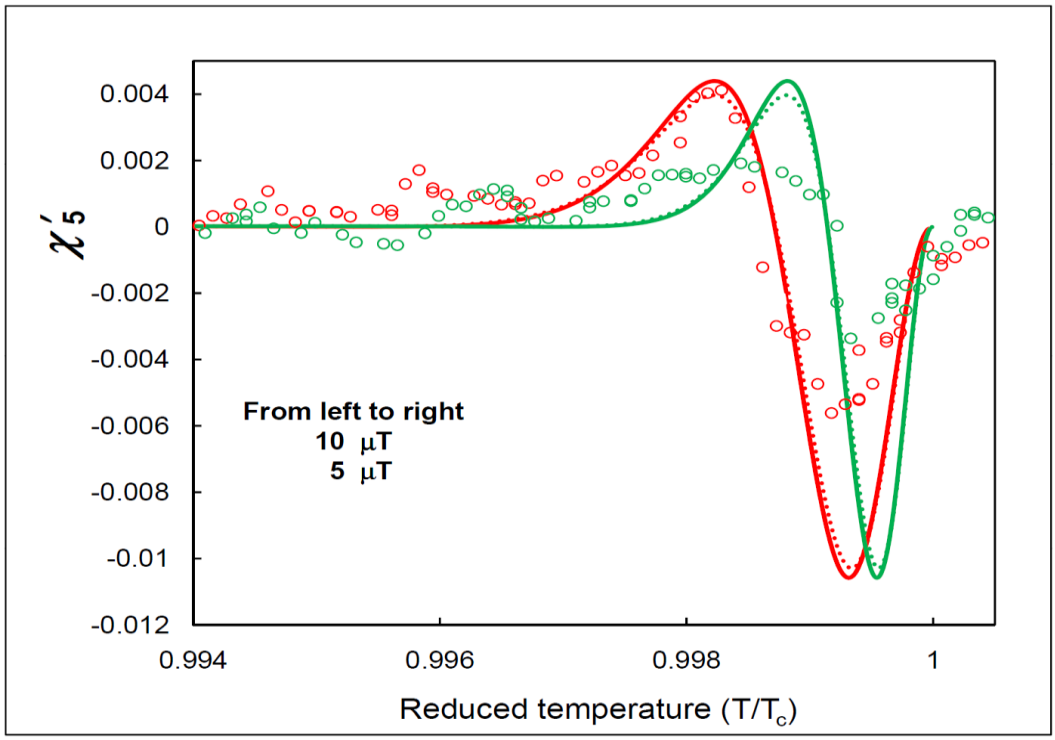

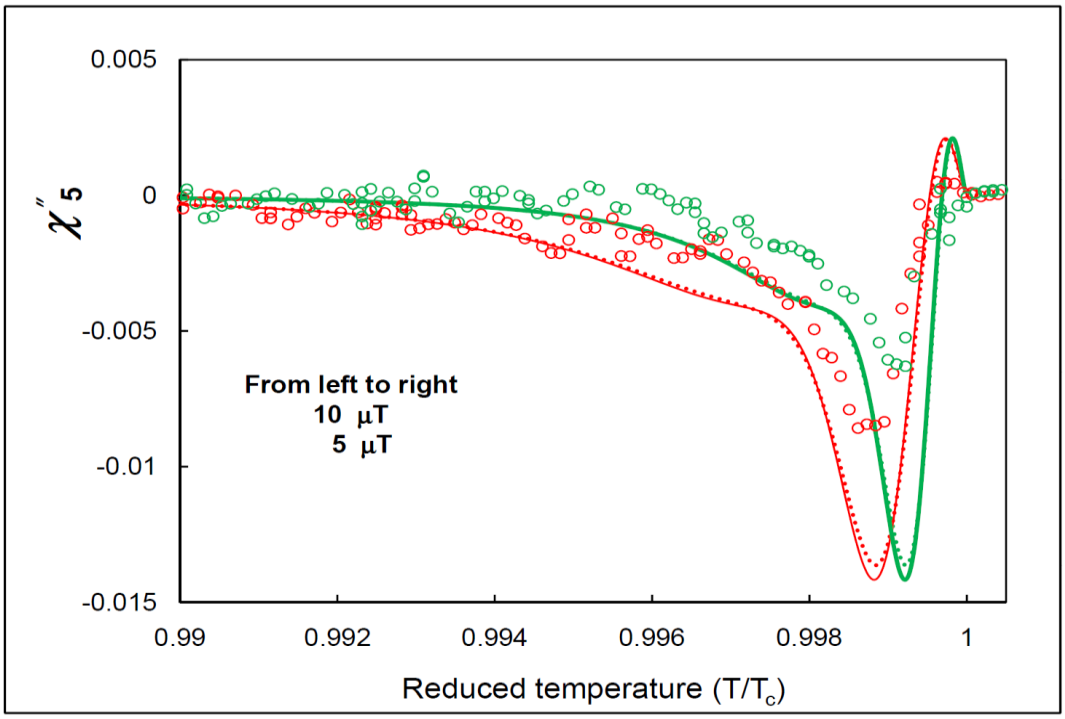

Fig. 32: *The AC field dependence of the experimental and theoretical 2D BCSM model data of fifth harmonic of AC susceptibility. The marks are the experimental data, while dashed and solid lines are the model to strip and disk data respectively. The sample has been measured in zero DC field, f = 1.5625 and cooling rate 0.1 K/min. The experimental data for $B_0 < 5$ μT were omitted because of high background noise. Model susceptibility data have been scaled by a factor s = 0.97, i.e. $\chi \rightarrow s\chi$.*

have plotted the AC magnetization loops, which cover the transition region, i.e. the last loop in the Meissner state towards T_c, the most saturated curve before converting to the normal state and the first curve in the normal state in addition to the curve corresponding to $T \approx T_p$. For B_0 = 2 and 1 μT the curves corresponding to the Meissner and normal state are omitted because of high background noise.

The AC field dependence of higher harmonics

The AC field dependence of the third and fifth harmonic measurements for the data which were shown previously in Fig. 27, can be found in Fig. 31 and Fig. 32 respectively. We noticed that there is a big similarity between the experimental and theoretical data. The differences are only quantitative. The higher harmonics show pronounced field dependence. The imaginary and real components of the third harmonic oscillate between positive and negative values. For B_0 = 10 μT the negative and positive peaks take the maximum values. When the AC field is decreased the two peaks decrease and shift to higher temperature. In addition their broadness also decreases. This is consistent with the results of critical state model (see the discussion above). The fifth harmonic (Fig. 32) shows the same trend like the third one, i.e. by decreasing the applied AC field the peaks shift to higher temperatures and there broadness decreases. Comparing our results to that in references [115, 116], the behaviour of the positive peak in χ_3 is different, where it increases with decreasing AC field amplitude. In our sample the decreasing in the positive peaks may be due to the increasing of linear response, where at small AC field amplitudes the vortices will not be able to leave the pinning centres [41, 113, 114]. In this situation each vortex will oscillate inside its effective pinning potential well rather than jumping from one to another.

In fact, the measurements of the higher harmonics have big advantages, where it can help in investigating the properties of the superconductors, see for example table 1 in reference [105]. Other thing is that the behaviour of the higher harmonics is important to determine the theoretical model to fit our data.

5. 2. Critical state response in $YBa_2Cu_3O_x$ wire

It was recognized soon after the discovery of high temperature superconductors (HTSC) that their magnetic properties are irreversible and show thermo-magnetic history effects [117]. The magnetic irreversibility properties observed under quasi-static changes of magnetic field are similar to those observed in conventional "hard" superconductors. Therefore they are understood within the same phenomenological models, i.e. the critical state model, which was applied earlier to the conventional hard superconductors.

Recently, highly sophisticated second generation high temperature superconducting (2G HTS) wires, namely $YBa_2Cu_3O_x$ (YBCO), were prepared with much more favourable flux pinning conditions at high temperatures. The conductors with critical current densities exceeding 10^{10} A m^{-2} at 77 K and self field have been fabricated. In particular, 2G HTS wire holds enormous promise for the efficient and reliable supply of electricity in applications such as electric power cables, fault current limiters, motors, generators, transformers and superconducting magnetic energy storage systems. These materials allow the validity of models to flux dynamics to be studied.

5.2.1. Dimensions and preparation of the sample

The sample of 2G HTS wire made by Super Power, Inc. is cut into 4 mm long segment of 4 mm wide wire [118, 119]. The structure of the wire is shown in Fig. 33. The wire consists of a 50 micrometers substrate, ~0.2 micrometer buffer stack, ~1 micrometer YBCO layer, ~2 micrometers of Ag with 40 micrometers total thickness of surround copper stabilizer. The substrate serves for two purposes: it provides the mechanical backbone of the conductor and is the base for growing the subsequent layers. The nickel alloy substrate (typically Hastelloy ® C276) is either 50 or 100 micrometers thick. The thin substrate thickness enables a high engineering current density, *J* in the final tape that is critical for many applications. It is electrochemically polished to a surface roughness of less than 2 nm and is smooth enough for ion beam assisted deposition of a textured MgO-based buffer stack that serves several functions including diffusion barrier, lattice matching and as the critical aligned template for growing the current carrying HTS film. Metallo-organic chemical vapour deposition (MOCVD) is used to grow the YBCO HTS film. The advantages of the MOCVD method include its extremely high deposition rate, ~0.7 m/min, and ability to extend its

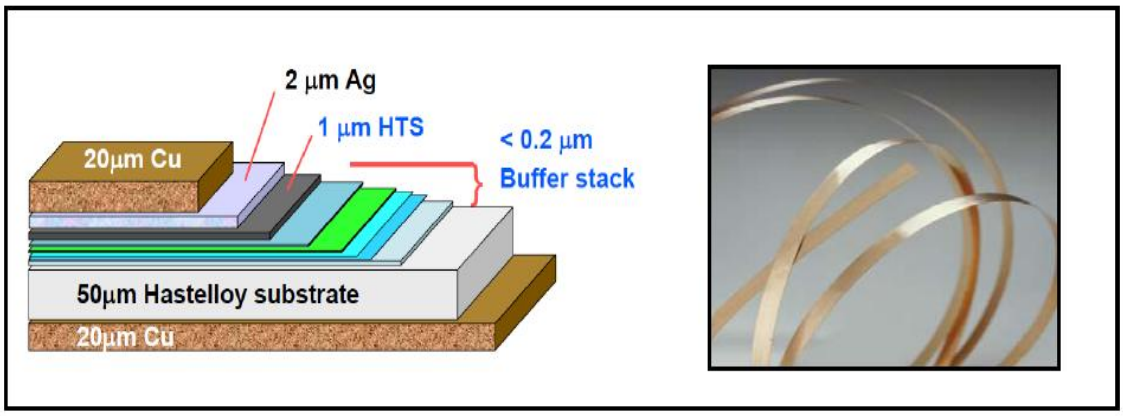

Fig. 33: *The structure of the second generation wire (2G HTS wire) [120].*

deposition area resulting in very high throughput. The YBCO HTS film is then capped by a thin Ag layer to provide good electrical contact. When required, stabilization of the conductor is provided by an electroplated copper layer that surrounds the entire structure. The thickness of the copper layer can be varied to meet the operational requirements of the wire in a specific application.

5.2.2. Meeting the model assumptions

The YBCO 2G wire sample satisfies the model assumptions. For 2D Bean critical state model (BCSM) to disk, the thickness $d = 1\ \mu$m $<< 2a = 4$ mm, where $2a$ is the width of the sample. But $d \geq \lambda$ is fulfilled only up to reduced temperature $T/T_c = 0.99$ for either linear or quadratic temperature dependence of λ using $\lambda(0) \approx$ 150–200 nm. However in this case the condition for the two-dimensional screening length, $\Lambda = 2\lambda^2/d << 2a$, is fulfilled [108]. On the other hand the important assumption to apply the 2D BCSM to strip, $d << 2a$ [82, 89], is fulfilled. As mentioned previously, both cases $d < \lambda$ and $d > \lambda$ are allowed in case of strip model.

5.2.3. Mapping of model data to the experimental data

The fundamental AC susceptibility of the 2G HTS wire sample in a slowly varying perpendicular field as a function of temperature T at an AC field amplitude of $B_0 = 10\ \mu$T and frequency $f = 1.5625$ Hz is shown in Fig. 34. a. The Cole – Cole plot of χ_1'' versus χ_1' is depicted in Fig. 34. b. The transition region near T_c is shown in detail in Fig. 35. The fundamental, third and fifth harmonics of the AC susceptibility for the 2G HTS wire in a perpendicular applied magnetic field as a function of reduced temperature, $\chi(T/T_c)$, are demonstrated in Fig. 35. The data are fitted to the 2D Bean

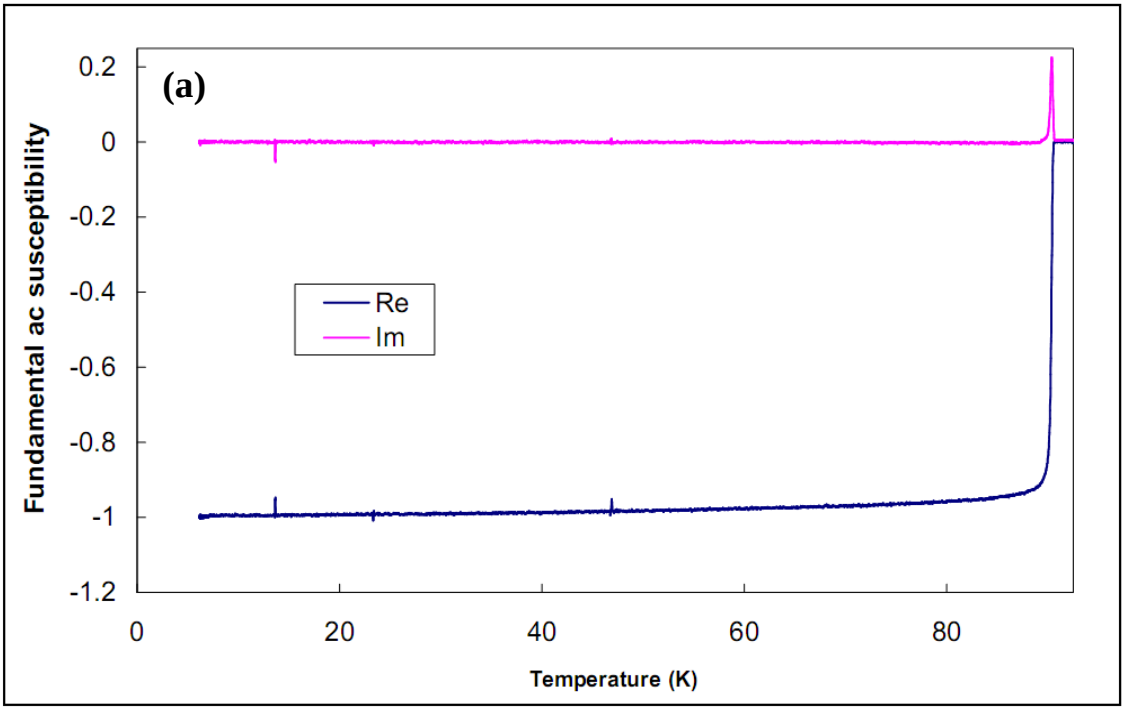

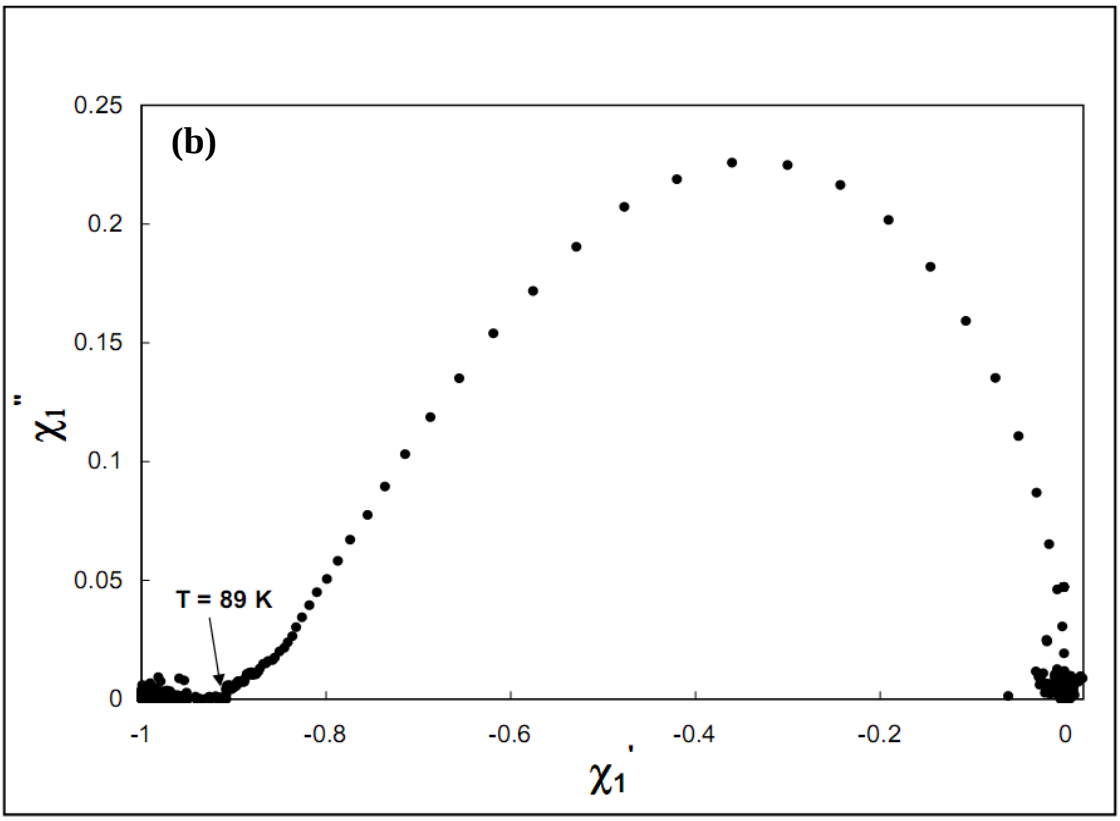

Fig. 34: *Fundamental AC susceptibility measured at B_0=10 μT, frequency of 1.5625 Hz, zero DC field and cooling rate of 2 K/min. (a) As a function of temperature. (b) The Cole – Cole plot of χ_1'' versus χ_1'. The transition is complete at T= 89 K, while the real part decreases slowly to –1.*

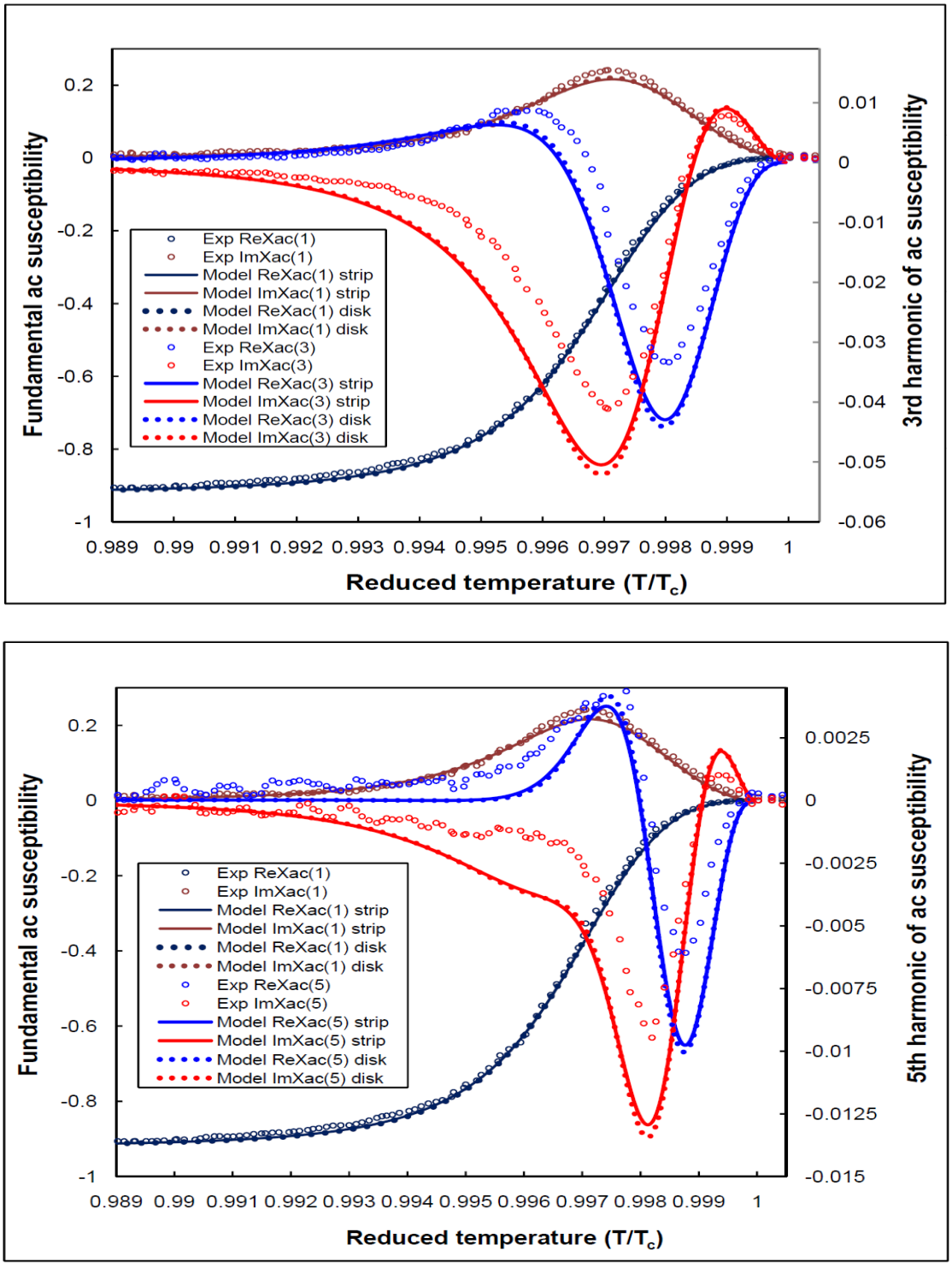

Fig. 35: *Fundamental AC susceptibility, third harmonic (top) and fifth harmonic (bottom) as a function of reduced temperature at B_0=10 μT, frequency of 1.5625 Hz, zero DC field, and cooling rate of 1 K/min. The marks are experimental data. The curves are susceptibilities calculated on the basis of the 2D Bean model to disk (dashed line) and strip (solid line) in a perpendicular applied magnetic field. The model susceptibility is scaled by a factor s=0.92, i.e. $\chi \rightarrow s\chi$.*

model for disk and strip. To fit the transition region the model susceptibility data were scaled by a factor s = 0.92, i.e. $\chi \rightarrow s\chi$. The temperature dependent real part of the fundamental susceptibility $\chi_1'(T)$ below the transition is evidently not related to the critical state, see Fig. 34. At $\chi_1' \sim 0.914$, i.e. $T \sim 89$ K, the imaginary part of the fundamental susceptibility, $\chi_1'' = 0$, results in no loss, which is an indication that the transition is completed. However, the real part of the fundamental susceptibility χ_1' decreases slowly to –1. It is not clear if this response is due to the temperature dependent flux penetration length. While its dependence is linear in pure YBCO crystals and quadratic when impurities and other defects are present [121], we have observed different temperature dependence. In the range of 4.2–85 K the temperature dependence may be approximated using a single term polynomial by $\chi_1'(T) = -1 + aT^{2.5}$, where $a \sim 6.4 \times 10^{-7}$, with residuals being less than 0.3% [108].

The frequency dependence of the AC susceptibility was measured for applied field frequencies of 0.78125, 1.5625, 3.125, 6.25, and 12.5 Hz at $B_0 = 10$ μT. With increasing AC field frequency the transition shifts weakly toward higher temperature. The shift in temperature is 0.1 K for frequencies of 0.78125 and 12.5 Hz, i.e., $\approx 10^{-3}$ of the reduced temperature.

Using Eq. (54), the best fit parameters are m = 1, n = 2, and T_c = 90.41 K (we note that our temperature sensor is not calibrated to such absolute accuracy even if the temperature resolution is on the order of ppm). For a model to disk, $c = 1.68 \times 10^{-5}$ and the estimated zero temperature critical current density is $J_c(0)_{\text{disk}} = B_0/\mu_0 cd \approx 9.47 \times 10^{11}$ A/m^2 at B_0 = 10 μT and d = 1 μm. The zero temperature current is $I_c(0)_{\text{disk}} = J_c(0)_{\text{disk}}\, 2a\, d \approx 3.8$ kA using a wire width of $2a$ = 4 mm. We have found that the critical current density has the temperature dependence, $J_c(T) = J_c(0)(1 - T/T_c)^2$, for both of models to disk and strip. Hence the calculated fundamental susceptibility of both models is plotted against $[1-(c/h_0)^{1/2}]$, where $h_0 = B_0/B_d$. Therefore the critical depinning current for a disk geometry at a temperature of 77 K or 0.85T is $I_c(77)$ = 83.4 A. While for a strip geometry the c parameter is given by, $c = 2.10 \times 10^{-5}$, results in zero temperature critical depinning current, $J_c(0)_{\text{strip}} = 1.19 \times 10^{12}$ A/m^2. The zero temperature current is given by, I_c (0) = 4.8 kA, while the critical depinning current at 77 K is given by $I_c(77)$ = 105 A. It is worth to mention here that the 2D Bean model to disk gives lower results

than the model to strip by nearly 18%. Since our sample is square, it is expected that the model to disk is more accurate than the model to strip as explained above.

5.2.4. AC field dependence of the susceptibility

The fundamental AC susceptibility as a function of temperature for different driving AC field amplitude is shown in Fig. 36. We note that measurements upon cooling and warming yield identical results. The experimental data are fitted to the 2D BCSM model to disk and strip (here we show only model to disk since the difference between both models is too small). With increasing AC field amplitude the transition extends toward lower temperatures accompanied by a corresponding broadening of the $\chi(T)$ transition as both models predict. The height of the absorption peak χ''_{1p} remains nearly unchanged unlike the case of Nb thin films. The best fit parameters found by linking the model curves to the experimental AC susceptibility are listed in Table 5.

The comparison with the complex AC susceptibility calculated for the model to the disk and strip shows that these models properly predict behaviour, particularly of harmonics as can be seen in Fig. 37 and Fig. 38 (here we show only the prediction of the model to disk, where the differences between both models are very small). The estimated critical current is between 77.8 A and 96.1 A for the model to disk while it is between 95.6 A and 118.3 A for the model to strip at 5 μT < B_0 < 20 μT in zero DC field and at 77 K. For this specific piece of the YBCO wire, the critical current estimated using a four probe method and 1 μV/cm criterion is 97 A at 77 K in self-field. This indicates that both models predict values close to the measured one. In case of the model to disk there is an error nearly from 19%, for B_0 = 5 μT, to 0.9% for B_0 = 20 μT. On the other hand, the model to strip gives an error between 1.4% for B_0 = 5 μT to -21% for B_0 = 20 μT. This indicates that the results in case of the model to disk are better as expected especially at high AC field amplitude, where the magnetic flux reaches to the centre of the sample and the moment saturates. The difference between the four probe method and the Bean model's data may result from the fact that the model assumes an infinite rise of resistance when the current density exceeds the critical depinning current density. On the other hand, a critical current estimated using a finite voltage criterion is influenced by a slope of the current-voltage characteristic [122].

The third and fifth harmonics for the same data shown in Fig. 36 are depicted in Fig. 37 and Fig. 38 respectively. Because of higher background noise, the data for

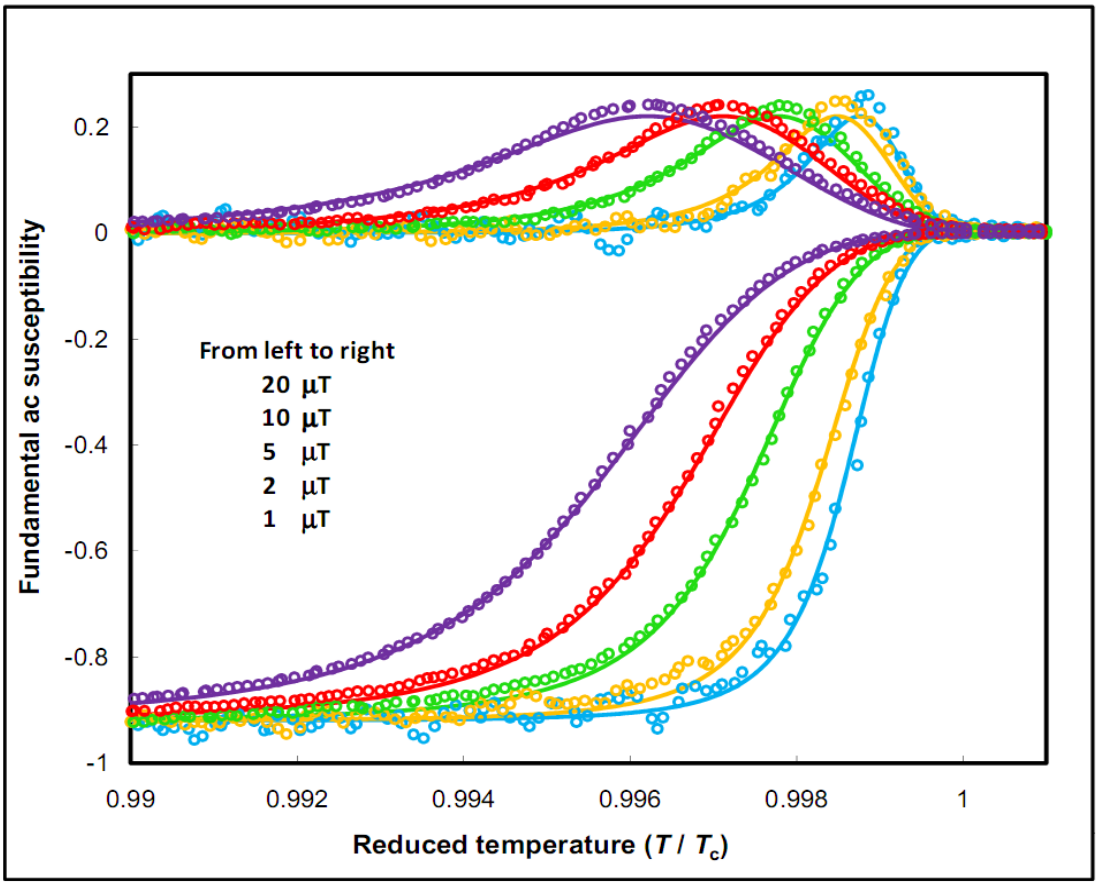

Fig. 36: *Temperature dependence of the fundamental AC susceptibility for different AC field amplitudes, frequency 1.5625 Hz, zero DC field, and cooling rate 1 K/min. The curves are susceptibility calculated on the basis of the 2D Bean model to disk, marks are the experimental data. The model susceptibility data are scaled by a factor s = 0.92, i.e.* $\chi \rightarrow s\chi$.

Table 5: *Parameters as a function of the AC applied field amplitude* B_0.

Bean model	B_0 (μT)	c	J_{c0} (A/m^2)	I_{c0} (KA)	I_c (77) (A)	T_P(K)
Disk	1	2.90×10^{-6}	5.49×10^{11}	22.0	48.2	90.30
	2	4.50×10^{-6}	7.07×10^{11}	28.3	62.2	90.27
	5	9.00×10^{-6}	8.84×10^{11}	35.4	77.8	90.21
	10	1.68×10^{-5}	9.47×10^{11}	37.9	83.4	90.14
	20	2.90×10^{-5}	1.10×10^{12}	43.9	96.1	90.03
Strip	1	3.50×10^{-6}	7.14×10^{11}	28.6	62.8	90.30
	2	5.40×10^{-6}	9.26×10^{11}	37.0	81.4	90.27
	5	1.15×10^{-5}	1.09×10^{12}	43.5	95.6	90.21
	10	2.10×10^{-5}	1.19×10^{12}	47.6	105	90.14
	20	3.70×10^{-5}	1.35×10^{12}	54.1	118	90.03

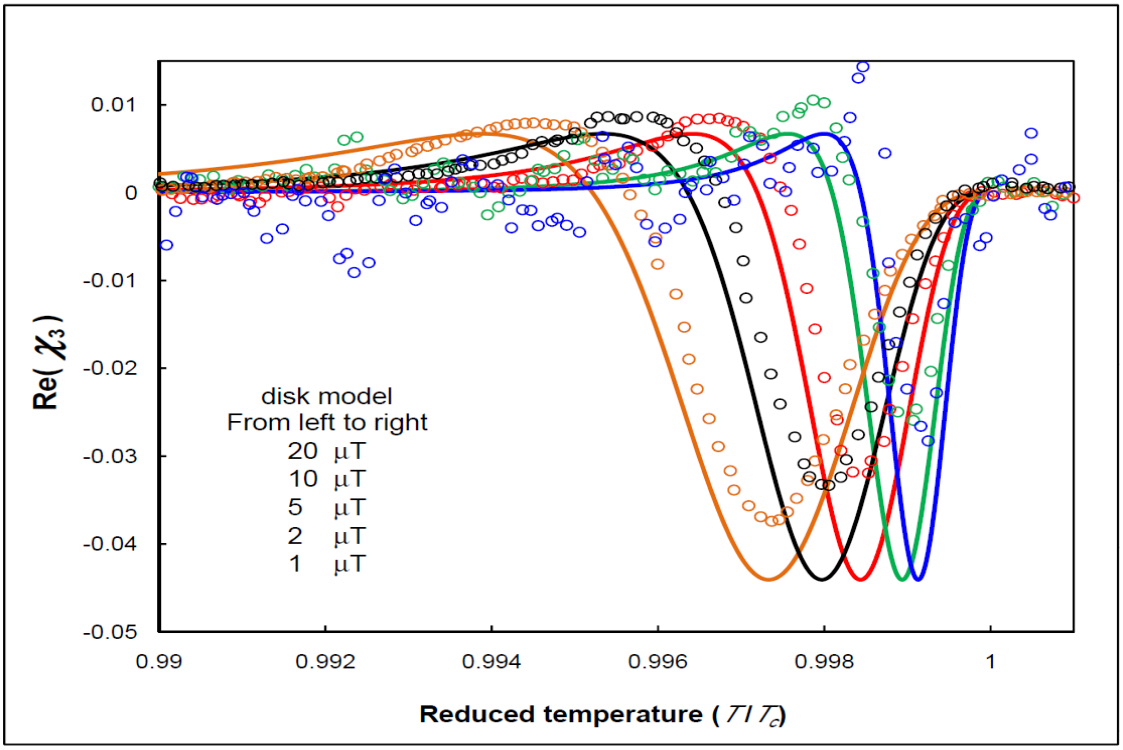

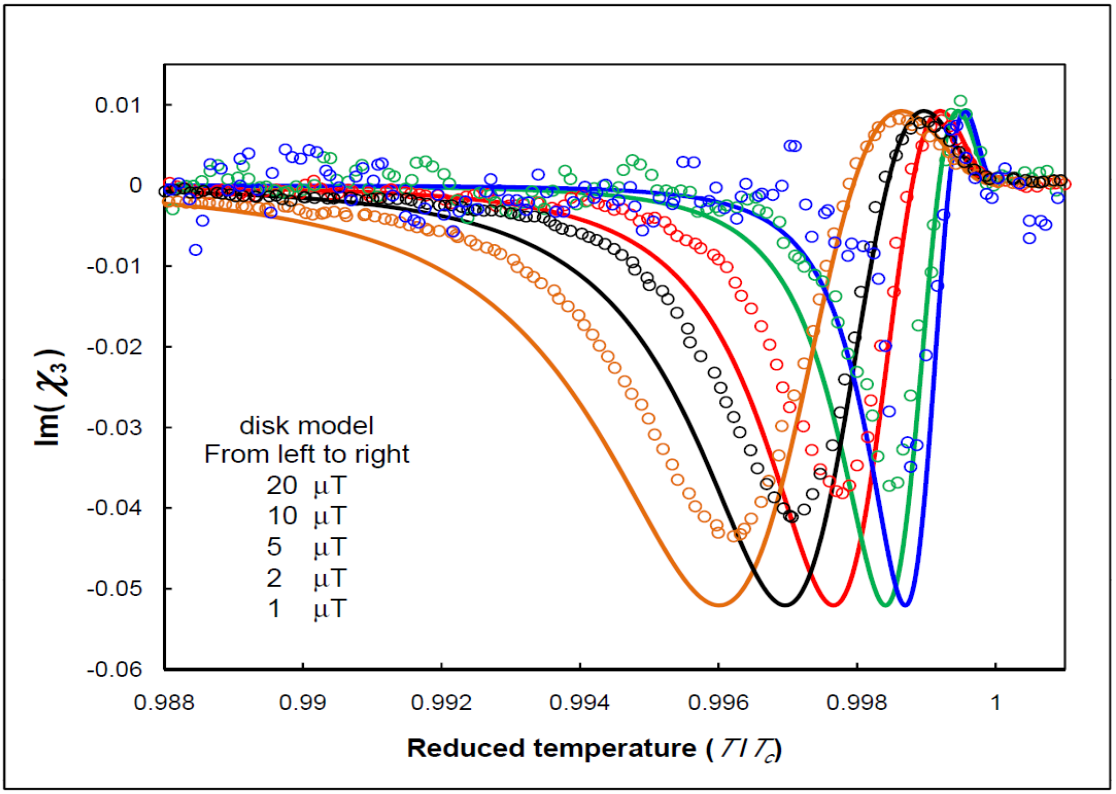

Fig. 37: *The temperature dependence of the third harmonic for different AC field amplitudes, frequency 1.5625 Hz, zero DC field and cooling rate 1 K/min. The curves are susceptibility calculated on basis of the 2D Bean model to disk, the marks are the experimental data. The model susceptibility is scaled by a factor s=0.92, i.e.* $\chi \rightarrow s\chi$.

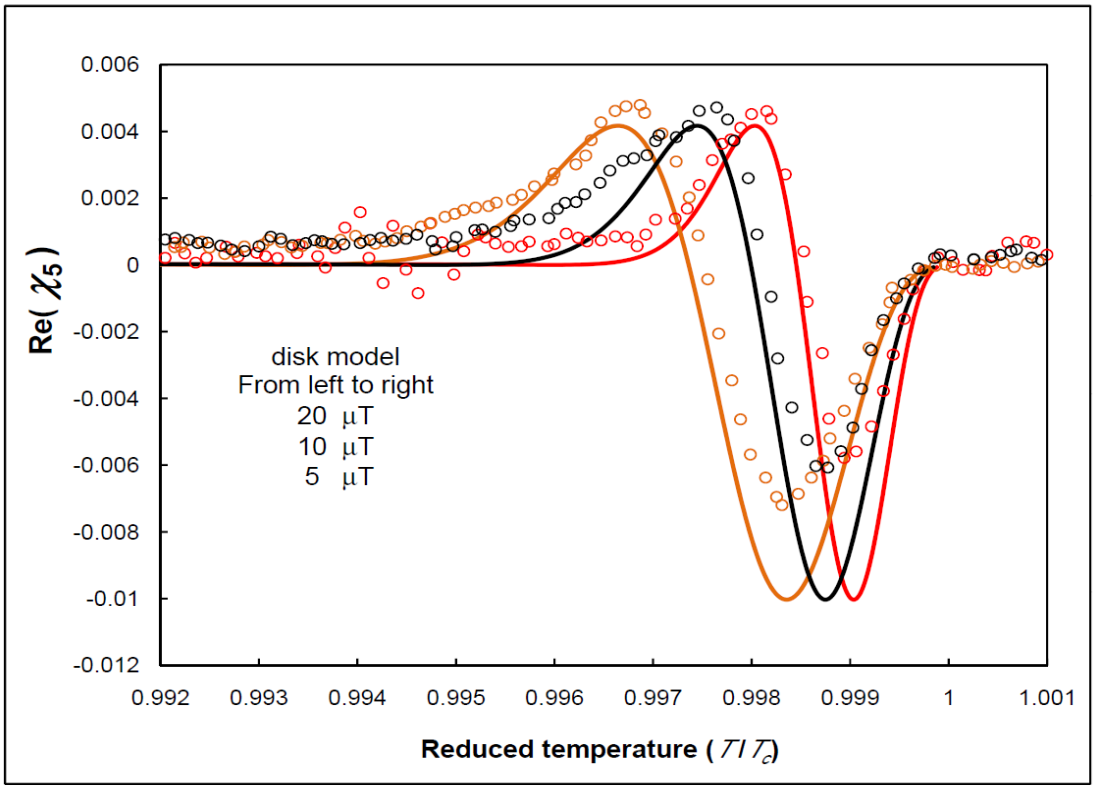

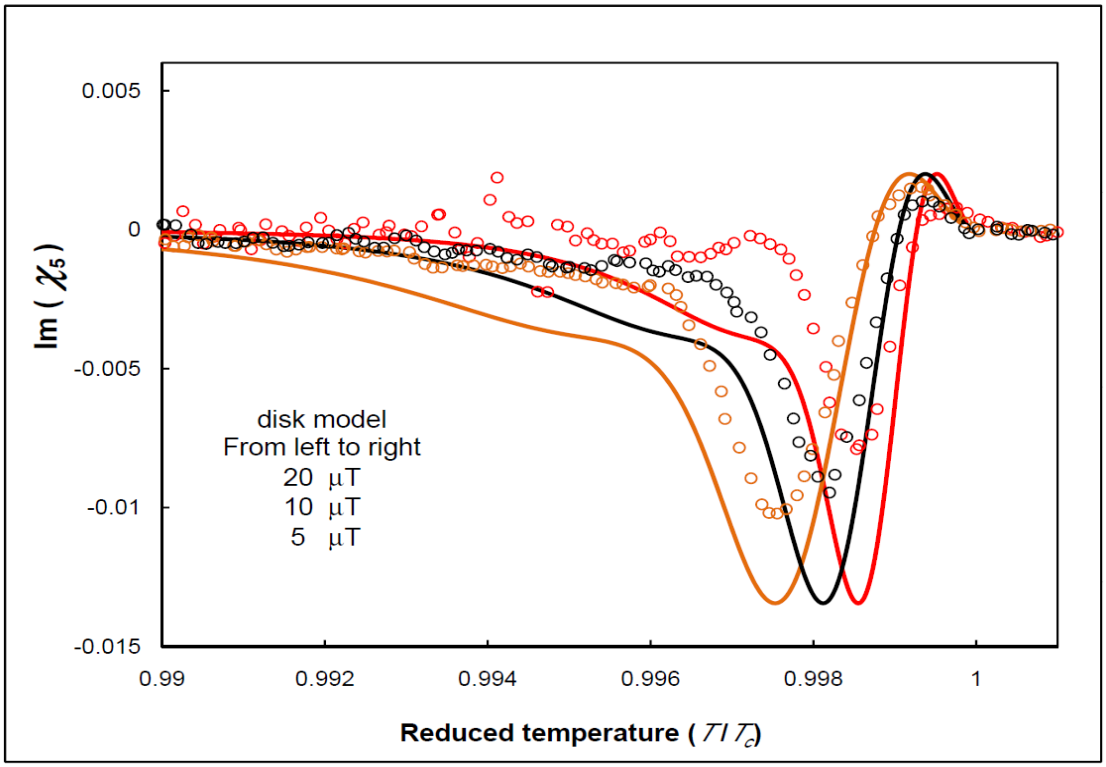

***Fig. 38**: The temperature dependence of the fifth harmonic for different AC field amplitudes, frequency 1.5625 Hz, zero DC field and cooling rate 1 K/min. The curves are susceptibility calculated on the basis of the 2D Bean model to disk, marks are the experimental data. The model susceptibility is scaled by a factor s=0.92, i.e. $\chi \rightarrow s\chi$.*

$B_0 < 5$ μT were removed in Fig. 38. The height of the positive peaks in both real and imaginary part of the third harmonic don't change with changing the AC field amplitude, while the depth of the negative peaks slightly increased with increasing the AC field amplitude. The behaviour of the real part on the fifth harmonic is similar, while the positive peak in χ_5'' decreases with decreasing the AC field amplitude. An inspection of AC magnetization loops proves that the magnetic flux does not reach saturation for small amplitudes, $B_0 < 5$ μT. Since the total displacement of the vortices in each cycle is proportional to the local amplitude of the AC field, the vortices will not be able to leave the pinning centres in small AC field, where the vortices oscillate inside their effective pinning potential wells rather than jump from one to another. Therefore the magnetic flux and critical current do not reach the centre of the sample. This can easily explain the increase of the zero critical current density with increasing AC field amplitude, which listed in Table 5. For more details see discussion above.

5.2.5. DC field dependence of the susceptibility

The effect of the DC magnetic field on the AC susceptibility can be seen in Fig. 39, where the measured χ_1' and χ_1'' as a function of temperature at various DC applied fields B_{dc} = 0, 0.5, 1, 2, 5 and 10 mT for f = 1.5652 Hz and AC field amplitude B_0 = 10 μT are plotted. The measurements in DC field were performed at field–cooling with subsequent field warming. Afterward, a DC field polarity was reversed and the DC field eventually changed. As the DC field increases, the transition in $\chi_1'(T)$ and $\chi_1''(T)$ becomes slightly broader and shifts toward lower temperature. The position of the absorption peak depends strongly on the DC field amplitude, B_{dc}. With increasing B_{dc} vortices are able to leave the flux pinning potential wells and move toward the centre of the sample [109]. Therefore the temperature where the dissipation peak occurs shifts to lower values, which is the case shown in Fig. 39. The peak height χ_{1p}'' in $\chi_1''(T)$ slightly increases with increasing the DC field. As the DC field amplitude further increases, χ_{1p}'' reaches saturation. The values of χ_{1p}'' can be found in Table 6. Experimentally, it has also been observed that with increasing DC fields, the peak height in $\chi_1''(T)$ increases to a certain value and remains constant for further increasing DC field amplitude B_{dc} [123]. Values of the T_c, c, J_{c0}, I_{c0}, $I_c(77)$, T_p and χ_{1p}'' as a function of the applied DC field B_{dc} are listed in Table 6. In the range of our applied DC and AC fields, the DC

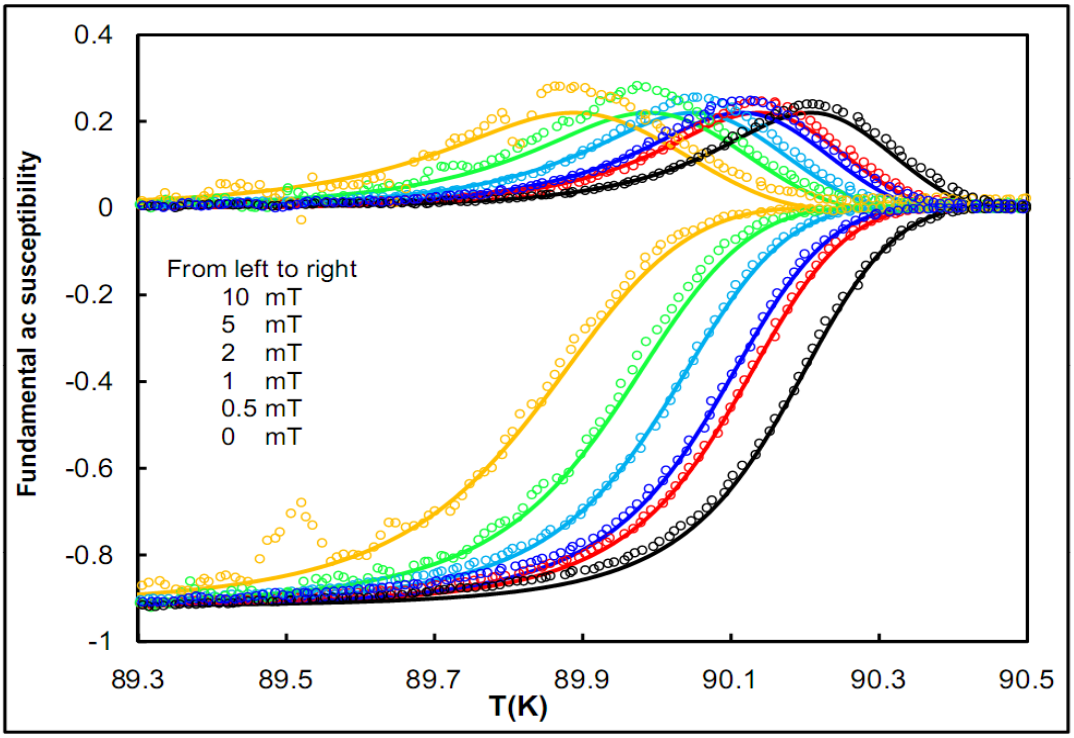

Fig. 39: *Fundamental AC susceptibility as a function of temperature for different DC fields* B_{dc} *= 0, 0.5, 1, 2, 5 and 10 mT (from right to left), AC field amplitude* B_0 *= 10 μT, frequency of 1.5625 Hz, and cooling rate of 1 K/min. Curves are susceptibility calculated based on 2D Bean model to disk. The model susceptibility is scaled by a factor s = 0.92, i.e.* $\chi \rightarrow s\chi$.

Table 6: *Parameters as a function of DC field amplitude* B_{dc}.

Bean model	B_{dc} (mT)	c	J_{c0} (A/m^2)	I_{c0} (KA)	I_c (77) (A)	T_c (K)	T_P(K)	χ''_{1p}
Disk	0	1.57×10^{-5}	1.01×10^{12}	4.05	89.8	90.46	90.21	0.241
	0.5	1.70×10^{-5}	9.36×10^{11}	3.74	82.3	90.4	90.14	0.247
	1	1.75×10^{-5}	9.09×10^{11}	3.64	79.8	90.38	90.13	0.249
	2	1.95×10^{-5}	8.16×10^{11}	3.26	71.1	90.33	90.05	0.256
	5	2.25×10^{-5}	7.07×10^{11}	2.83	61.3	90.29	89.97	0.282
	10	2.90×10^{-5}	5.49×10^{11}	2.20	47.2	90.23	89.89	0.2817
Strip	0	2.10×10^{-5}	1.19×10^{12}	4.76	106	90.46	90.21	0.241
	0.5	2.02×10^{-5}	1.24×10^{12}	4.96	109	90.40	90.14	0.247
	1	2.10×10^{-5}	1.19×10^{12}	4.76	104	90.38	90.13	0.249
	2	2.40×10^{-5}	1.04×10^{12}	4.17	90.7	90.33	90.05	0.256
	5	3.10×10^{-5}	8.06×10^{11}	3.23	70.0	90.29	89.97	0.282
	10	3.60×10^{-5}	6.94×10^{11}	2.78	59.6	90.23	89.89	0.2817

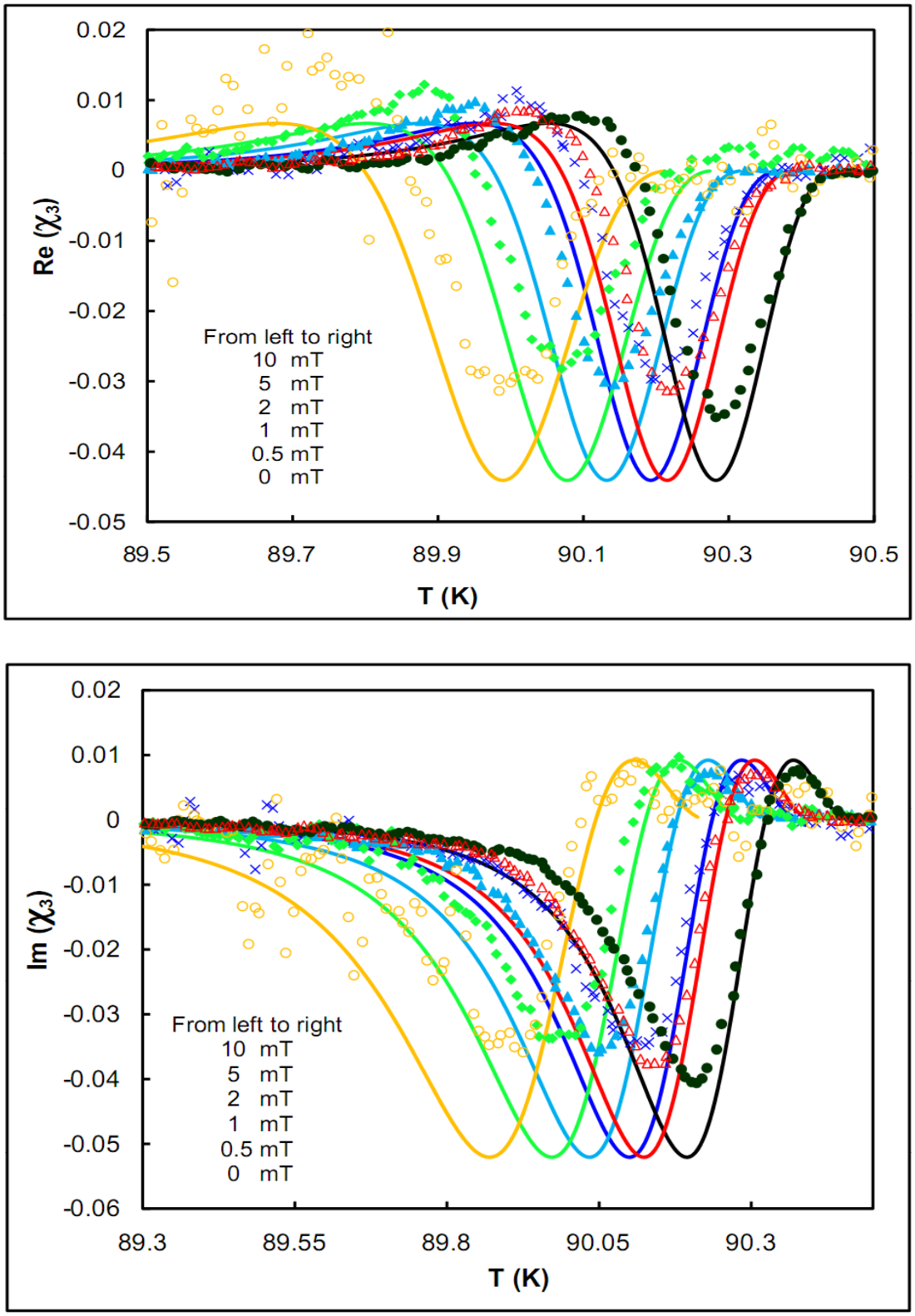

***Fig. 40**: Temperature dependence of the third harmonic of susceptibility of 2G YBCO wire for different DC field amplitudes, frequency 1.5625 Hz, B_0 =10 μT and cooling rate 1 K/min. Curves are the susceptibility calculated on basis of 2D Bean model to disk, while marks are the experimental data. The model susceptibility data are scaled by a factor s = 0.92, i.e. $\chi \rightarrow s\chi$.*

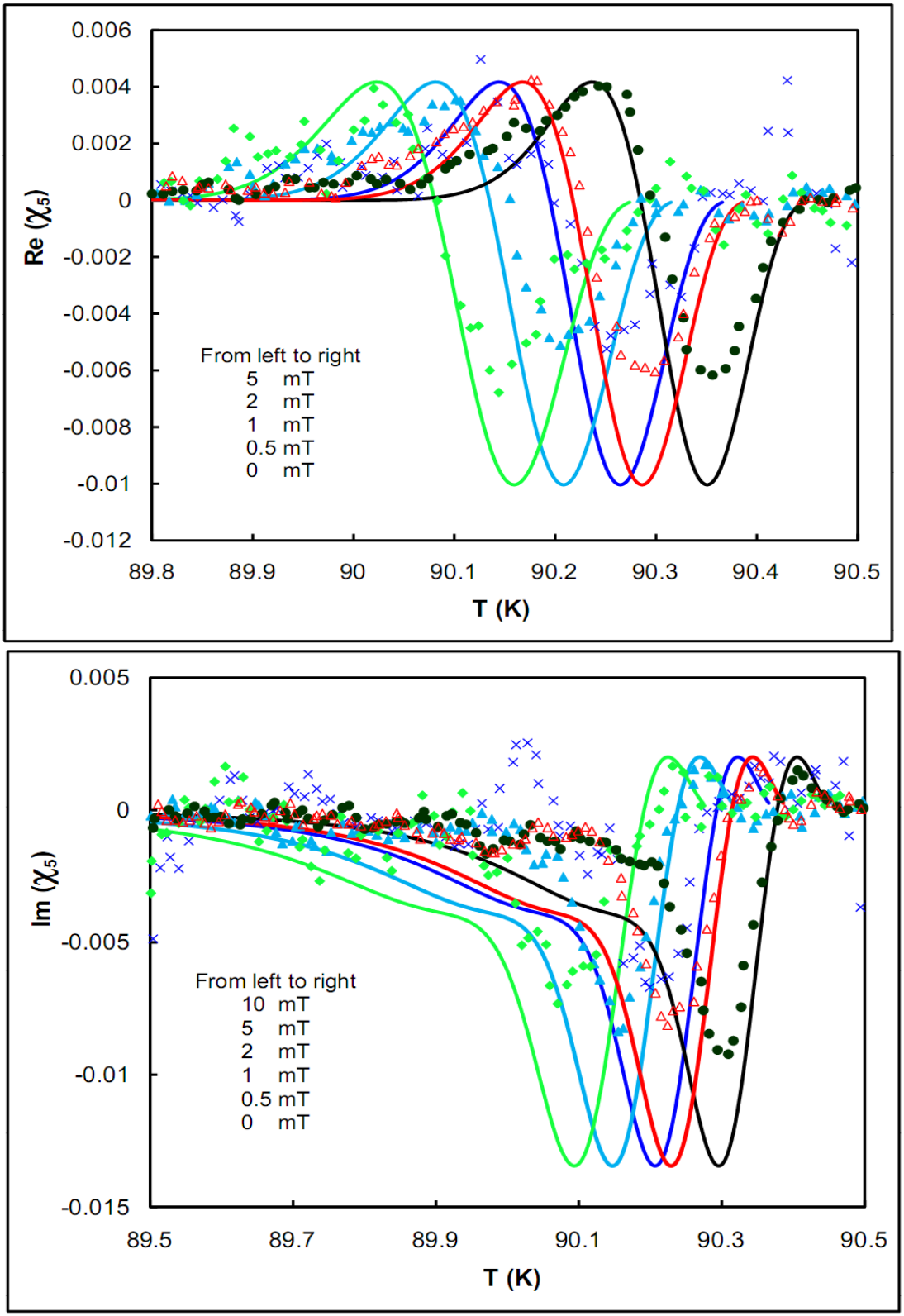

***Fig. 41**: Temperature dependence of the fifth harmonic of susceptibility of 2G YBCO wire for different DC field amplitudes, frequency 1.5625 Hz, B_0 =10 μT and cooling rate 1 K/min. Curves are the susceptibility calculated on basis of 2D disk mode, while marks are the experimental data. The model susceptibility is scaled by a factor s=0.92, i.e. $\chi \rightarrow s\chi$.*

field nearly does not affect the AC susceptibility, i.e. response to the applied AC field. It only reduces the critical current. The estimated critical current I_c = 47.2 A for disk geometry and 59.64 A for strip geometry, at 77 K and 0.01 T agrees with the value I_c = 16 A (Sm) and 32 A (Zr : Gd) at 77 K and 1 T estimated using a four probe method [124]. However it is expected that the 2D Bean model to disk should give better results as explained previously.

The effect of the DC applied magnetic field on the third and fifth harmonics can be seen in Fig. 40 and Fig. 41 respectively (these are the same data which were represented in Fig. 39). As the DC field increases the peaks shift to lower temperatures. The same trend was found by Shalove and Dorman [125]. They reported measurements of the third harmonic amplitude in a small constant AC field as a function of temperature for various DC fields ranging from 0 to 0.1 T. As they increased the DC field, the peak moved to lower temperatures. This is consistent with the result of critical state model since B_d, which is proportional to J_c, decreases as the DC field is increased. The same behaviour has been reported by other experimental groups, see reference [126] and the references within it.

5.3. Critical state response in bulk (Nd, Eu,Gd)-123 superconductors

The magnetic irreversibility observed under the quasi-static changes of magnetic field, or of temperature, has been explained using the critical state model. The Bean critical state model, BCSM, was solved for long samples, having a zero demagnetization factor, in parallel applied magnetic field such as long cylinder and slab. Also the model was solved for samples with finite thickness in perpendicular applied magnetic field such as 2D disk and strip, where the demagnetization factor is high.

The light rare earth (LRE) compounds of the 123 family, LRE = Sm, Nd, Eu, Gd, possess a significantly better pinning potential than Y-123. Thus, they could achieve high critical current and trap high magnetic field at a significantly higher temperature. These materials can soon become magnetic hearts of small mobile diagnostic and other devices. Their main advantages will be compactness and magnetic field strength. The dominance of the LRE-123 blocks in the field of bulk superconducting magnets lies in the ability of LRE elements to exchange positions with Ba atoms and form so called LRE/Ba solid solution. Clusters of such a locally varied composition represent very effective point-like pinning disorder. Excellence in this direction belongs to the compounds with two or three different LRE atoms mixed on the rare earth sites. The different atomic radii allow for a new degree of freedom in tailoring pinning properties of such superconductors. (Nd, Eu,Gd)-123 is the best-known example of this class. In this part we apply the BCSM to a thick (Nd, Eu,Gd)-123 sample.

5.3.1. Preparation and dimensions of the sample

The $(Nd_{0.33}Eu_{0.38}Gd_{0.28})Ba_2Cu_3O_y$ "NEG-123" pellet, doped by 0.035 mol% ZnO, 0.5 mol% Pt, 5 mol% Gd-211, and 1 wt.% Ag, was produced from high-purity commercial powders of Nd_2O_3, Eu_2O_3, Gd_2O_3, $BaCO_3$ and CuO mixed in nominal composition. The starting powders were three times thoroughly ground and calcined at 880 $^{\circ}$C for 24 hours with intermediate grinding. Sintering was carried out at 900 $^{\circ}$C for 15 hours at Ar/0.1% O_2. Platinum was added to help in refining the Gd-211 particles, ZnO to improve growth control of the compound, and silver to enhance mechanical strength of the material. The well-mixed powders were pressed into pellets 20 mm in diameter and 10 mm thick, and consolidated by cold isostatic pressing to 200 MPa. The sample was grown in Ar/0.1% O_2 atmosphere, at the gas flow of 300 ml/min [127]. The

structure was determined with a RINT2200 (Rigaku) high-resolution automated X-ray powder diffractometer. The sample was found to be single-phase with less than 3 mol% Gd-211[128].

For measurements a platelet of 1.5 mm thick was cut from the pellet (Fig. 42. a). From the platelet, three series of small samples for magnetic susceptibility measurements, each of $a \times b \times c$ = 1.5 mm × 1.5 mm × 0.4 mm in size, were sliced from three piles cut out in the pellet centre, periphery, and in-between, as indicated in Fig. 42. b. We have measured two samples, number 6 from the centre and number 15 from the periphery. The sample number 15 has been measured in two orientations, i.e. *c* axis is parallel and perpendicular to the applied magnetic field $\mathbf{B_a}$. In this section we show only the results of sample number 15 with c // $\mathbf{B_a}$.

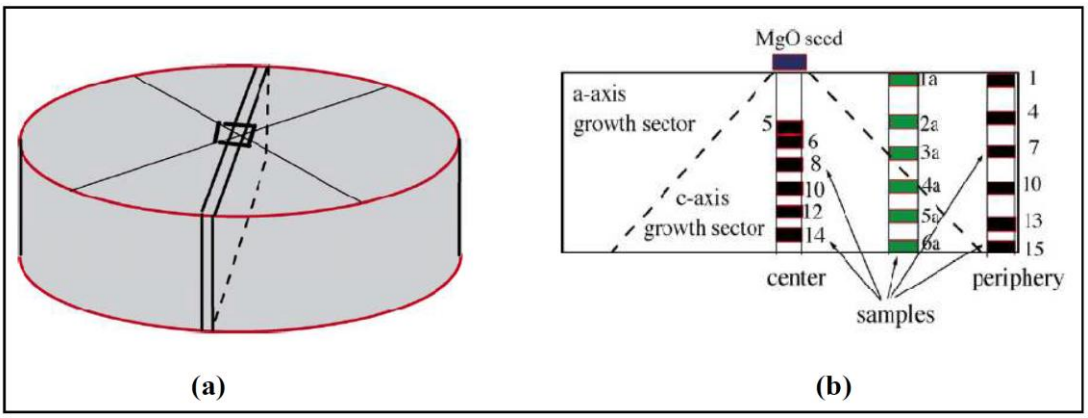

Fig. 42: *(a) Sketch of the investigated pellet with the marked position of the studied platelet. (b) Scheme of the platelet with marked positions of samples 1.5 mm ×1.5 mm × 0.4 mm in size, shown as small boxes [128].*

5.3.2. Results and discussion of NEG-123 bulk sample

The temperature dependence of the fundamental AC susceptibility of the bulk NEG-123 sample is shown in Fig. 43. The sample has been measured at warming rate of 1 K/min for AC field amplitude B_0 = 0.5 mT, frequency of 1.5625 Hz and zero DC field. The experimental data have been fitted to the BCSM to disk, strip, slab and cylinder (the fitting to model to strip is not shown here). We have found that the real part of the experimental fundamental susceptibility, χ_1', can be fitted well in case of the models to strip and disk, while the absorption peak in the imaginary part, χ_1'', is smaller than the value predicted by the models. The fitting parameters m, n, c and T_c can be found in Table 7. The absolute zero critical current density J_{c0} has been calculated with

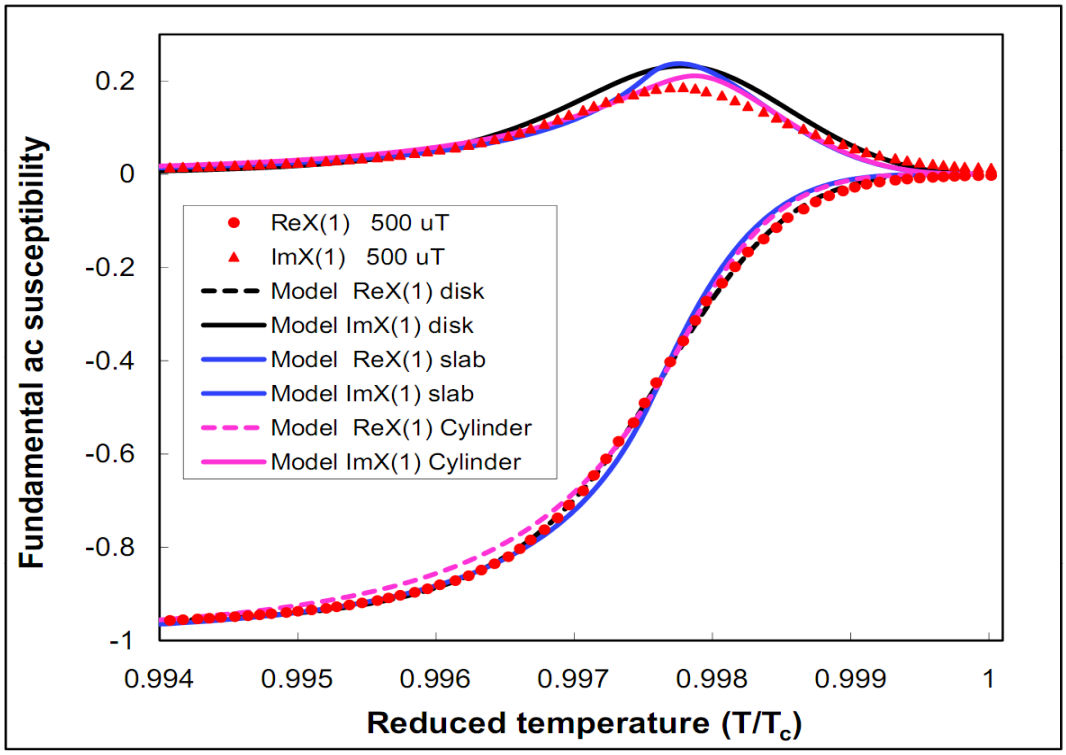

Fig. 43: *Temperature dependence of the fundamental AC susceptibility of NEG-123 bulk sample measured in AC magnetic field B_0 = 0.5 mT with frequency 1.5625 Hz and zero DC field in warming rate 1 K/min. Curves are the susceptibility calculated on basis of Bean model to disk, slab and cylinder. The susceptibility of Bean model to disk is reduced by a factor s = 0.97.*

the aid of Eq. (55) (see Table 7). Using Eq. (52) we have found that, the temperature dependence of the critical current density in case of the models to disk and strip is given by $J_c(T) = J_{c0}(1\text{-}T/T_c)^{5/2}$, while for the models to slab and cylinder it is given by $J_c(T) = J_{c0}(1\text{-}T/T_c)^3$. The values of the critical current density at 77 K are in between 4.60×10^{10} A/m^2 for the model to disk and 2.34×10^{11} A/m^2 for the model to cylinder respectively. These values are two to three orders of magnitude higher than J_c (77) ≈ 4×10^8 A/m^2, which was estimated in reference [128] for the same sample using the extended Bean's critical state model method [129].

Table 7: *Fit parameters and results of fitting to Bean model in different geometries.*

Model	*m*	*n*	*c*	J_{c0} (A/m^2)	J_c(77) (A/m^2)	I_{c0} (A)	I_c(77) (A)
Disk	1	2.5	4.70×10^{-7}	4.23×10^{12}	4.60×10^{10}	2.53×10^{6}	2.76×10^{3}
Strip	1	2.5	5.90×10^{-7}	5.29×10^{12}	5.76×10^{10}	3.17×10^{6}	3.45×10^{3}
Slab	1	3	1.56×10^{-8}	3.40×10^{13}	1.49×10^{11}	2.04×10^{7}	8.99×10^{4}
Cylinder	1	3	1.00×10^{-8}	5.30×10^{13}	2.34×10^{11}	3.18×10^{7}	1.40×10^{5}

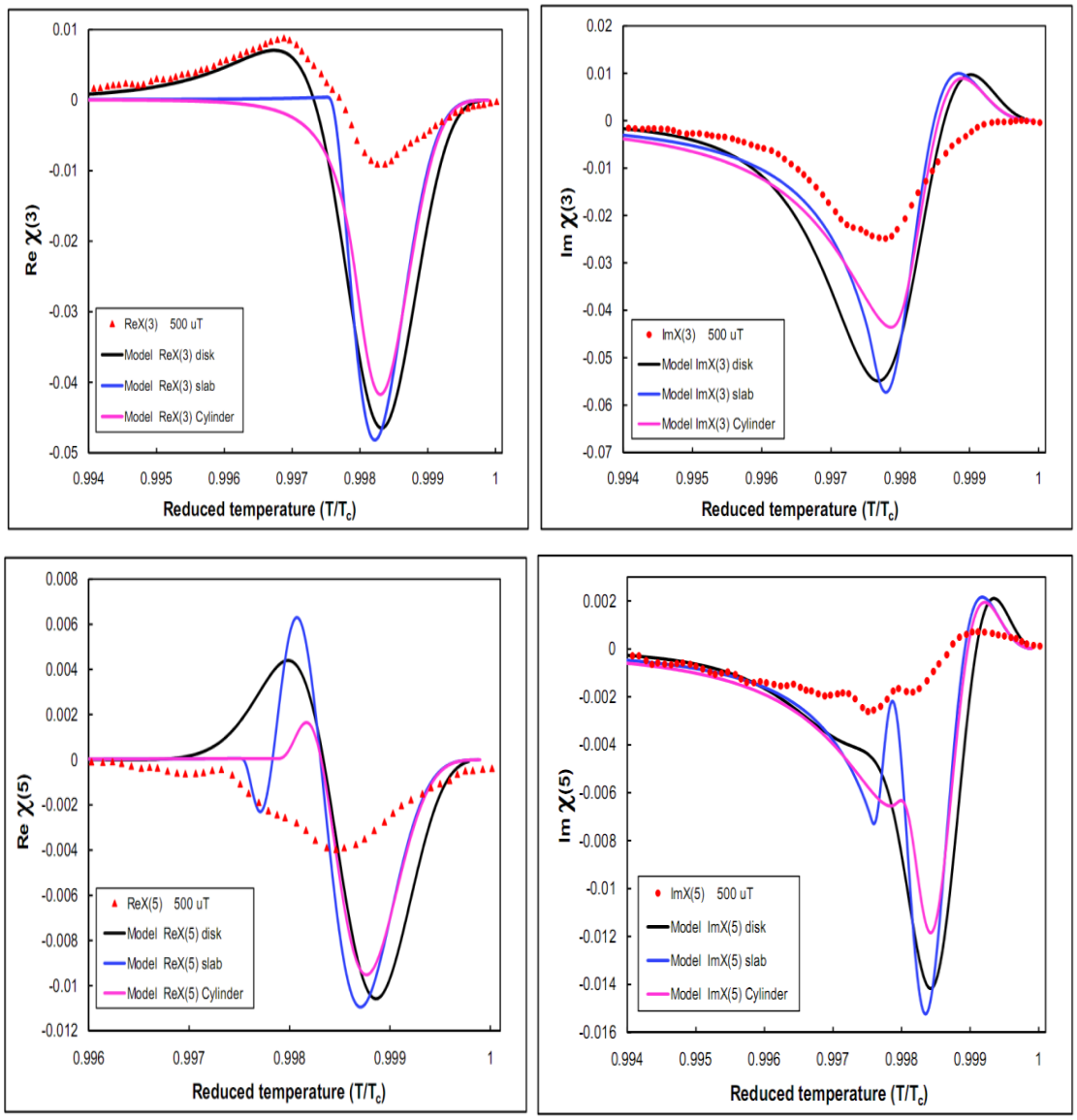

Fig. 44: *Temperature dependence of the third and fifth harmonics of the AC susceptibility of the bulk NEG-123 sample measured in AC magnetic field B_0 = 0.5 mT with frequency 1.5625 Hz and zero DC field in warming rate 1 K/min. Marks are experimental data while curves are model data.*

A crucial parameter in choosing a model of fitting is the behaviour of higher harmonics. At least it should agree qualitatively with the model. Fig. 44 depicts the third and fifth harmonics of the AC susceptibility of NEG-123 bulk sample with the theoretical Bean models data. For third harmonic all the models nearly fail to describe the imaginary part, χ_3'', where the positive hump which is predicted by the models does not exist. On the other hand the models to disk and strip predict the positive hump in the real part, χ_3', while the negative peak in the theoretical curves looks deeper than the experimental one. At the same time all models nearly fail to describe the behaviour of

the fifth harmonic in both the imaginary, χ_5'', and the real part, χ_5'.

The disagreement between the experimental data and the theoretical models can be attributed to the sample geometry. In case of 2D Bean critical state model to disk and strip, it is assumed that the sample has very low thickness, *d*, i.e. the ratio $d/2a \rightarrow 0$, where 2*a* is the width of the sample. On the other hand, for parallel geometries namely slab and cylinder, the ratio *d/2a* is assumed to be very high or infinite. The values of the ratio *d/2a* for different samples can be found in Table 8. From the table we can see that, the *d/2a* ratio for NEG-123 bulk sample is nearly 1000 times greater than the *d/2a* ratio for 2G HTS wire and more than 5000 times greater than the *d/2a* ratio for Nb thin film. From numerical calculations, Brandt [130] found that for $d/2a < 0.02$ the computed virgin magnetization $m(h)$ practically coincides with the thin strip result $m_{strip}(h) = \tanh(h)$, while the parallel limit (slab geometry) $m_{slab}(h) = h - h^2/4$ is reached only at relatively large side ratios $d/2a > 6$. For $d >> a$ the difference $m_{strip}(h) - h + h^2/4$ is proportional to $2a/d$. In case of our bulk sample the ratio, $0.02 < d/2a = 0.267 < 6$. This value is in between the two limits, which explains why the four analytical models to disk, strip, slab and cylinder do not fit the experimental data particularly higher harmonics and hence there is a need to use numerical methods to fit our data. However Brandt claims that, for different *d/2a* ratios, the normalized $m(h)$ magnetization curve differs by < 0.03 from some average curve $m_{av}(h)$. In other words the maximum difference between the virgin magnetization curve in the two limits (strip and slab) should be 6%.

Other thing that needs to be stressed in is that, although the difference between the model susceptibility curves and the experimental susceptibility in Fig. 43 is not so high, the error in calculation of the critical current density is high. This result indicates the importance of considering the behaviour of higher harmonics, when choosing the model to apply.

Table 8: *Comparisons between the dimensions of Nb, 2G HTS wire thin films and NEG-123 bulk sample.*

	NEG-123 bulk	**2G HTS wire**	**Nb**
a (m)	1.50×10^{-3}	4.00×10^{-3}	5.00×10^{-3}
d (m)	4.00×10^{-4}	1.00×10^{-6}	2.50×10^{-7}
d/2a	0.267	2.50×10^{-4}	5.00×10^{-5}

Conclusion

In the framework of this thesis, we have introduced a new contactless method to determine the critical current density and hence critical current in hard type II superconducting samples. This method is based on the analytical solutions of the Bean critical state model (BCSM), i.e. a slab in a parallel field, as originally studied by Bean [61, 62], the long cylinder in an axial field [41], the strip in transverse field [82, 89] and the disk in perpendicular field [84, 86]. Unlike others, our method is easier to use and the sample is not damaged during the measurements.

We have found that the model susceptibility calculated on the basis of the BCSM can fit our experimental data when the model susceptibility is plotted against $\left[1-\left(c\,B_0/B^*\right)^{1/n}\right]^{1/m}$ and the experimental susceptibility versus reduced temperature T/T_c, where B_0 is the amplitude of the applied field and B^* is the full penetrated field, B_p, for cylinder and slab or B_d for disk and strip. This enables us to match the experimental and model data using only four free parameters, c, n, m, and T_c, hence the critical depinning current density J_c can be easily calculated, since B^* is proportional to J_c.

We have measured temperature dependence of magnetization of Nb thin films in slowly varying perpendicular applied field. We have found that both fundamental-frequency and harmonics of the experimental AC susceptibility agree well with the AC susceptibility computed on basis of the Bean critical state model to disk and strip. We have found that the temperature dependence of the critical depinning current density can be expressed as; $J(T) = J_{c0}(1\text{-}T/T_c)^{3/2}$, where J_{c0} is the zero temperature critical current density. The estimated critical depinning current values using this contactless method sound reasonably. The measurements of the fundamental AC susceptibility as a function of temperature for set of amplitudes B_0 indicate that, as the field is increased, the T_c shifts down, in agreement with expected suppression of the superconductivity by the applied magnetic field. At the same time, the transition region broadens and the absorption peak shifts to lower temperature. An inspection of AC magnetization loops proves that the magnetic flux does not reach a saturation for $B_0 < 5\ \mu$T. Below this threshold field the vortices will not be able to leave the pinning centres [41]. In this situation each vortex will oscillate inside its effective pinning potential well rather than jumping from one to

another. This can easily explain the increase of the absolute critical current density and height of the imaginary peak χ''_{1p} with increasing AC field amplitude in our sample. This allows us to conclude that to apply BCSM, the amplitude of the applied magnetic field should be higher than a threshold amplitude, where the magnetic front and the critical current penetrate entire the sample to the centre.

We have checked out the validity of the BCSM on high temperature unconventional superconductors, i.e. 2G YBCO thin films. We have measured the response of the critical state in the HTS wire to a slowly varying AC field as a function of temperature. The comparison with a complex AC susceptibility calculated from models to disk and strip shows that these models properly predict behaviour, particularly of the harmonics. It has been found that the temperature dependence of the critical current density is $J_c(T) = J_{c0}(1- T/T_c)^2$ for both models, which allowed us to calculate the critical depinning current at temperature T. The estimated critical depinning current using this contactless method agrees well with the values estimated using a four probe contact measurement. However in case of the model to disk there is an error nearly from 19%, for $B_0 = 5\ \mu$T, to 0.9% for $B_0 = 20\ \mu$T. While for the model to strip the error is in-between 1.4%, for $B_0 = 5\ \mu$T, to –21% for $B_0 = 20\ \mu$T. It has been noticed that the values estimated using BCSM to disk is always lower than the model to strip and more accurate especially at higher amplitude of the AC applied magnetic field. Our measurements prove a strong pinning and quasi-static Bean critical state up to the critical temperature. The measurements in changing AC field amplitude show that the height of χ''_{1p} remains nearly unchanged with increasing B_0, unlike the case of Nb thin films. When a DC field is applied the transition shifts toward a lower temperature as the field increases, while the shape of the transition remains unchanged. In the range of our applied DC and AC fields, the DC field nearly does not affect the AC susceptibility, i.e. response to the applied field. It only reduces the critical current.

It is important to apply our contactless method, which is based on the BCSM to determine the critical depinning current, to other geometries rather than thin films to see the differences. For this purpose we have measured the response of the critical state in the bulk NEG-123 sample to a slowly varying AC field as a function of temperature. We have compared the experimental measured χ_{ac} data to theoretical χ_{ac} which were computed on the basis of the analytical BCSM model in case of models to disk, strip, slab and cylinder. We have found that none of these four analytical models correctly

predicts the behaviour of our bulk sample especially the higher harmonics. The disagreement between the experimental and theoretical data can be attributed to the sample geometry. The ratio $d/2a$, where d is the thickness of the sample and $2a$ is its width, is in between the two limits of thin films (strips and disks) and infinite long samples in parallel applied magnetic field (slabs and cylinders). However the temperature dependence of the critical current density for the models to disk and strip can be given by $J_c(T) = J_{c0}(1–T/T_c)^{5/2}$, while for the models to slab and cylinder is given by $J_c(T) = J_{c0}\ (1\text{-}T/T_c)^3$. Although there is small difference between the theoretical and experimental fundamental susceptibility, the error in the estimated critical current density is high, that suggests an importance of the finding of a behaviour of the higher harmonics when choosing a theoretical model to fit the experimental data.

Bibliography

[1] B. S. Deaver and W. M. Fairbank, Physical Review letters **7** (1961) 43.

[2] R. Doll and M. Nabauer, Physical Review letters **7** (1961) 51.

[3] D. Dew-Hughes, Low Temperature Physics **27** (2001) 713.

[4] B. D. Josephson, Physics Letters **1** (1962) 251.

[5] M. Cyrot, Reports on Progress in Physics **36** (1973) 103.

[6] M. Tinkham, Introduction to superconductivity, McGraw Hill, New York, 1996. ISBN 0070648786

[7] A. A. Abrikosov, Soviet Physics Jetp-USSR **5** (1957) 1174.

[8] M. R. Koblischka and R. J. Wijngaarden, Superconductor Science & Technology **8** (1995) 199.

[9] L. W. Shubnikov, W. I. Khotkevich, J. D. Shepelev, and J. N. Ryabinin, Soviet Physics Jetp-USSR **7** (1937) 221.

[10] U. Essmann and H. Trauble, Physics Letters A **24** (1967) 526.

[11] D. Saintjames and P. G. Gennes, Physics Letters **7** (1963) 306.

[12] B. J. Yuan and J. P. Whitehead, Physical Review B **44** (1991) 6943.

[13] I. A. Parinov, Microstructure and properties of high-temperature superconductors, Springer, Berlin ; New York, 2007. ISBN 9783540709763.

[14] T. Kobayashi, H. Hayakawa, and M. Tonouchi, Vortex electronics and squids, Springer, Berlin ; New York, 2003. ISBN 3-540-40231-4.

[15] I. Giaever, Physical Review letters **15** (1965) 825.

[16] H. Hashizume and S. Toda, Ieee Transactions on Magnetics **34** (1998) 3016.

[17] A. Buzdin and D. Feinberg, Journal De Physique **51** (1990) 1971.

[18] S. N. Artemenko and A. N. Kruglov, Physics Letters A **143** (1990) 485.

[19] J. R. Clem, Physical Review B **43** (1991) 7837.

[20] L. I. Glazman and A. E. Koshelev, Physical Review B **43** (1991) 2835.

[21] J. R. Clem and M. W. Coffey, Physical Review B **42** (1990) 6209.

[22] M. Tachiki and S. Takahashi, Solid State Communications **72** (1989) 1083.

[23] A. Brass, H. J. Jensen, and A. J. Berlinsky, Physical Review B **39** (1989) 102.

[24] M. W. Coffey, Physical Review B **46** (1992) 567.

[25] H. R. Glyde, L. K. Moleko, and P. Findeisen, Physical Review B **45** (1992) 2409.

[26] R. Wordenweber, Physical Review B **46** (1992) 3076.

[27] M. Martin, C. Kendziora, L. Mihaly, and R. Lefferts, Physical Review B **46** (1992) 5760.

[28] L. R. Tessler, J. Provost, and A. Maignan, Applied Physics Letters **58** (1991) 528.

[29] R. Labusch, phys. status solidi B **32** (1969) 439.

[30] A. I. Larkin and Y. N. Ovchinnikov, Journal of Low Temperature Physics **34** (1979) 409.

[31] D. S. Fisher, M. P. A. Fisher, and D. A. Huse, Physical Review B **43** (1991) 130.

[32] J. Z. Liu, Y. X. Jia, R. N. Shelton, and M. J. Fluss, Physical Review letters **66** (1991) 1354.

[33] S. Martin and A. F. Hebard, Physical Review B **43** (1991) 6253.

[34] T. Fukami, K. Hayashi, T. Yamamoto, T. Nishizaki, Y. Horie, F. Ichikawa, T. Aomine, V. Soares, and L. Rinderer, Physica C **184** (1991) 65.

[35] M. J. Goldstein and W. G. Moulton, Physical Review B **40** (1989) 8714.

[36] O. B. Hyun, D. K. Finnemore, L. Schwartzkopf, and J. R. Clem, Physical Review Letters **58** (1987) 599.

[37] R. Job and M. Rosenberg, Superconductor Science & Technology **5** (1992) 7.

[38] G. S. Park, C. E. Cunningham, B. Cabrera, and M. E. Huber, Physical Review letters **68** (1992) 1920.

[39] A. Wadas, O. Fritz, H. J. Hug, and H. J. Guntherodt, Zeitschrift Fur Physik B-Condensed Matter **88** (1992) 317.

[40] E. H. Brandt, Reports on Progress in Physics **58** (1995) 1465.

[41] A. M. Campbell and J. E. Evetts, Advances in Physics **21** (1972) 199.

[42] H. Ullmaier, Irreversible properties of type ii superconductors, Springer-Verlag, Berlin ; New York, 1975. ISBN 0-387-07424-4.

[43] R. P. Huebener, Superconductor Science & Technology **8** (1995) 189.

[44] H. Ikuta, N. Hirota, Y. Nakayama, K. Kishio, and K. Kitazawa, Physical Review letters **70** (1993) 2166.

[45] H. Ikuta, N. Hirota, K. Kishio, and K. Kitazawa, Physica C **235** (1994) 237.

[46] Y. Shapira and Neuringe.Lj, Physical Review **154** (1967) 375.

[47] E. M. Forgan and C. E. Gough, Physics Letters A **26** (1968) 602.

[48] P. Lemmens, P. Froning, S. Ewert, J. Pankert, G. Marbach, and A. Comberg, Physica C **174** (1991) 289.

[49] D. Dominguez, N. GronbechJensen, and A. R. Bishop, Physical Review Letters **78** (1997) 2644.

[50] F. C. Moon, M. M. Yanoviak, and R. Ware, Applied Physics Letters **52** (1988) 1534.

[51] P. N. Peters, R. C. Sisk, E. W. Urban, C. Y. Huang, and M. K. Wu, Applied Physics Letters **52** (1988) 2066.

[52] H. Kitaguchi, J. Takada, K. Oda, A. Osaka, Y. Miura, Y. Tomii, H. Mazaki, and M. Takano, Physica C **157** (1989) 267.

[53] G. Blatter, M. V. Feigelman, V. B. Geshkenbein, A. I. Larkin, and V. M. Vinokur, Reviews of Modern Physics **66** (1994) 1125.

[54] T. T. M. Palstra, B. Batlogg, L. F. Schneemeyer, and J. V. Waszczak, Physical Review letters **61** (1988) 1662.

[55] P. W. Anderson, Physical Review Letters **9** (1962) 309.

[56] M. Tinkham, Physical Review letters **13** (1964) 804.

[57] J. Bardeen and M. J. Stephen, Physical Review **140** (1965) A1197.

[58] P. W. Anderson and Y. B. Kim, Reviews of Modern Physics **36** (1964) 39.

[59] K. Fossheim and A. Sudbø, Superconductivity : Physics and applications, Wiley, Chichester, West Sussex, England ; Hoboken, NJ, 2004. ISBN 0-470-84452-3.

[60] W. Klose, Physics Letters **8** (1964) 12.

[61] C. P. Bean, Physical Review Letters **8** (1962) 250.

[62] C. P. Bean, Reviews of Modern Physics **36** (1964) 31.

[63] C. P. Poole, H. A. Farach, and R. J. Creswick, Superconductivity, Academic Press, San Diego, 1995. ISBN 0125614551

[64] Y. Yeshurun, A. P. Malozemoff, F. Holtzberg, and T. R. Dinger, Physical Review B **38** (1988) 11828.

[65] F. Irie and K. Yamafuji, Journal of the Physical Society of Japan **23** (1967) 255.

[66] D. Leblanc and M. A. R. Leblanc, Physical Review B **45** (1992) 5443.

[67] Y. B. Kim, C. F. Hempstead, and A. R. Strnad, Physical Review Letters **9** (1962) 306.

[68] Y. B. Kim, C. F. Hempstead, and A. R. Strnad, Physical Review **129** (1963) 528.

[69] W. A. Fietz, J. Silcox, M. R. Beasley, and W. W. Webb, Physical Review **136** (1964) A335.

[70] J. H. P. Watson, Journal of Applied Physics **39** (1968) 3406.

[71] H. Dersch and G. Blatter, Physical Review B **38** (1988) 11391.

[72] Q. H. Lam, Y. Kim, and C. D. Jeffries, Physical Review B **42** (1990) 4846.

[73] M. Xu, D. L. Shi, and R. F. Fox, Physical Review B **42** (1990) 10773.

[74] V. Sokolovsky, V. Meerovich, S. Goren, and G. Jung, Physica C **306** (1998) 154.

[75] M. Maslouh, F. Bouillault, A. Bossavit, and J. C. Verite, Ieee Transactions on Applied Superconductivity **7** (1997) 3797.

[76] E. H. Brandt, Physical Review B **52** (1995) 15442.

[77] E. H. Brandt and A. Gurevich, Physical Review Letters **76** (1996) 1723.

[78] V. M. Vinokur, M. V. Feigelman, and V. B. Geshkenbein, Physical Review letters **67** (1991) 915.

[79] B. Lehndorff, High-t_c superconductors for magnet and energy technology : Fundamental aspects, Springer, Berlin ; New York, 2001. ISBN 3-540-41231-X.

[80] E. H. Brandt, Physical Review Letters **74** (1995) 3025.

[81] D. Karmakar, Indian J. Phys. **79** (2005) 1107.

[82] E. H. Brandt and M. Indenbom, Physical Review B **48** (1993) 12893.

[83] P. N. Mikheenko and Y. E. Kuzovlev, Physica C **204** (1993) 229.

[84] J. Zhu, J. Mester, J. Lockhart, and J. Turneaure, Physica C **212** (1993) 216.

[85] H. Theuss, A. Forkl, and H. Kronmuller, Physica C **190** (1992) 345.

[86] J. R. Clem and A. Sanchez, Physical Review B **50** (1994) 9355.

[87] J. Z. Sun, M. J. Scharen, L. C. Bourne, and J. R. Schrieffer, Physical Review B **44** (1991) 5275.

[88] W. T. Norris, Journal of Physics D-Applied Physics **3** (1970) 489.

[89] E. H. Brandt, M. V. Indenbom, and A. Forkl, Europhysics Letters **22** (1993) 735.

[90] E. Zeldov, J. R. Clem, M. Mcelfresh, and M. Darwin, Physical Review B **49** (1994) 9802.

[91] Y. Yang, T. Hughes, C. Beduz, D. M. Spiller, R. G. Scurlock, and W. T. Norris, Physica C **256** (1996) 378.

[92] E. H. Brandt, Physical Review B **58** (1998) 6506.

[93] E. H. Brandt, Physical Review B **55** (1997) 14513.

[94] T. Herzog, H. A. Radovan, P. Ziemann, and E. H. Brandt, Physical Review B **56** (1997) 2871.

[95] Q. Y. Chen, in Magnetic susceptibility of superconductors and other spin systems (R. A. Hein, T. L. Francavilla, and D. H. Liebenberg, eds.), Plenum Press Div Plenum Publishing Corp, New York, 1991, p. 81. ISBN 0-306-44197-7.

[96] T. Ishida and R. B. Goldfarb, Physical Review B **41** (1990) 8937.

[97] M. J. Qin and C. K. Ong, Physica C **341-348** (2000) 1039.

[98] J. Clarke and A. I. Braginski, The squid handbook, Wiley-VCH, Weinheim, 2004. ISBN 3-527-40229-2.

[99] T. Van Duzer and C. W. Turner, Principles of superconductive devices and circuits, Prentice Hall, Upper Saddle River, N.J., 1999. ISBN 0132627426.

[100] T. P. Orlando and K. A. Delin, Foundations of applied superconductivity, Addison-Wesley, Reading, Mass., 1991. ISBN 0201183234.

[101] Z. Janu, Z. švindrych, A. Youssef, and B. Lucia, in Superconductivity - theory and applications (A. M. Luiz, ed.), InTech, Rijeka, 2011, p. 261. ISBN 978-953-307-151-0.

[102] Z. Janu, R. Tichy, F. Soukup, M. Novák, and M. Behenský, Czechoslovak Journal of Physics **46** (1996) 2811.

[103] Z. Janu, F. Soukup, and R. Tichy, International Journal of Materials & Product Technology **26** (2006) 388.

[104] G. Tsoy, Z. Janu, M. Novak, F. Soukup, and R. Tichy, Physica B **284** (2000) 2122.

[105] F. Gomory, Superconductor Science & Technology **10** (1997) 523.

[106] A. Youssef, Z. Svindrych, J. Hadac, and Z. Janu, in 16th Annual Conference of Doctoral Students WDS'07, Vol. **16**, 2007, p. 48.

[107] A. Youssef, Z. Svindrych, J. Hadac, and Z. Janu, Ieee Transactions on Applied Superconductivity **18** (2008) 1589.

[108] A. Youssef, Z. Svindrych, and Z. Janu, Journal of Applied Physics **106** (2009) 063901.

[109] M. J. Qin and X. X. Yao, Physical Review B **54** (1996) 7536.

[110] T. May, in Institute for Physical High Technology, Vol. **Thesis**, Jena, Germany, 1999.

[111] K. Yamamoto, H. Mazaki, H. Yasuoka, T. Terashima, and Y. Bando, Physica C **192** (1992) 47.

[112] L. Ji, R. H. Sohn, G. C. Spalding, C. J. Lobb, and M. Tinkham, Physical Review B **40** (1989) 10936.

[113] A. M. Campbell, Journal of Physics Part C Solid State Physics **2** (1969) 1492.

[114] A. M. Campbell, Journal of Physics Part C Solid State Physics **4** (1971) 3186.

[115] O. Ozogul, phys. status solidi A **202** (2005) 1793.

[116] O. Ozogul, Journal of Superconductivity **18** (2005) 503.

[117] K. A. Muller, M. Takashige, and J. G. Bednorz, Physical Review letters **58** (1987) 1143.

[118] D. W. Hazelton and V. Selvamanickam, P Ieee **97** (2009) 1831.

[119] J. C. Hernandez-Llambes and D. Hazelton, in 2009 Ieee Pulsed Power Conference, Vols 1 and 2, Ieee, New York 2009, p. 221.

[120] Y. Y. Xie, M. Marchevsky, X. Zhang, K. Lenseth, Y. M. Chen, X. M. Xiong, Y. F. Qiao, A. Rar, B. Gogia, R. Schmidt, A. Knoll, V. Selvamanickam, G. G. Pethuraja, and P. Dutta, Ieee Transactions on Applied Superconductivity **19** (2009) 3009.

[121] P. J. Hirschfeld and N. Goldenfeld, Physical Review B **48** (1993) 4219.

[122] D. W. Hazelton, V. Selvamanickam, J. M. Duval, D. C. Larbalestier, W. D. Markiewicz, H. W. Weijers, and R. L. Holtz, Ieee Transactions on Applied Superconductivity **19** (2009) 2218.

[123] C. Y. Lee and Y. H. Kao, Physica C **241** (1995) 167.

[124] V. Selvamanickam, Y. M. Chen, X. M. Xiong, Y. Y. Y. Xie, M. Martchevski, A. Rar, Y. F. Qiao, R. M. Schmidt, A. Knoll, K. P. Lenseth, and C. S. Weber, Ieee Transactions on Applied Superconductivity **19** (2009) 3225.

[125] A. Shaulov and D. Dorman, Applied Physics Letters **53** (1988) 2680.

[126] Y. Oda, I. Nakada, T. Kohara, and K. Asayama, Japanese Journal of Applied Physics Part 2-Letters **26** (1987) L608.

[127] M. Muralidhar, T. Kono, M. Jirsa, N. Sakai, M. Murakami, and I. Hirabayashi, Superconductor Science & Technology **19** (2006) S550.

[128] M. Jirsa, M. Rames, K. Jurek, M. Muralidhar, P. Das, M. R. Koblischka, and T. Wolf, Mater. Sci. Eng., B **151** (2008) 25.

[129] D. X. Chen and R. B. Goldfarb, Journal of Applied Physics **66** (1989) 2489.

[130] E. H. Brandt, Physical Review B **54** (1996) 4246.

List of Tables

Abbreviations

AC	alternating current
AD	analogue to digital
BCSM	Bean critical state model
CSM	critical state model
DA	digital to analogue
DC	direct current
EMF	electromotive force
FFT	fast Fourier transform
FLL	flux line lattice
FL	flux line
GL	Ginzburg-Landau
HS	high sensitivity magnetometer
HTSC	high temperature superconductors
LRE	light rare earth
SR	standard sensitivity magnetometer
SQUID	superconducting quantum interference devices
TAFF	thermally assisted flux flow

Author (co)publications and presentations

[1] **A. Youssef**, Z. Svindrych, J. Hadac, and Z. Janu, *Analysis of critical state response in thin films by AC susceptibility measurements*, IEEE Transactions on Applied Superconductivity, 2008, vol. 18, no. 2, p. 1589-1592.

[2]* **A. Youssef**, Z. Svindrych, and Z. Janu, *Analysis of magnetic response of critical state in second-generation high temperature superconductor YBa_2Cu_3Ox wire*, Journal of Applied Physics, 2009, vol. 106, no. 6, p. 063901-1-063901-6.

[3] **A. Youssef**, L. Banicova, Z. Svindrych, and Z. Janu, *Contactless Estimation of Critical Current Density and Its Temperature Dependence Using Magnetic Measurements*, Acta Physica Polonica A, 2010, vol. 118, no. 5, p. 1036-1037.

[4] Z. Svindrych, **A. Youssef**, and Z. Janu, *Link between Magnetic and Dielectric Properties in Magnetite*, Acta Physica Polonica, 2010, vol. 118, no. 5, p. 940-941.

[5] *Z.* Janu, *Z.* švindrych, **A. Youssef**, and B. Lucia, *Critical State Analysis Using Continuous Reading SQUID Magnetometer*. In A.M. Luiz. *Superconductivity - Theory and Applications.* Rijeka: InTech, 2011, p. 261-278, ISBN 978-953-307-151-0.

[6] **A. Youssef**, Z. Svindrych, J. Hadac, and Z. Janu, *Critical state in Nb thin film*, in 16th Annual Conference of Doctoral Students WDS'07, 2007, vol. 16, p. 48–53.

[7] **A. Youssef** and *Z.* Janů, *Study of noise in higher harmonics of AC magnetization on basis of critical state model in Nb thin film*, In proceedings of IEC 2008 6th International Engineering conference, Egypt, 2008, P. 200.

[8] **A. Youssef**, *Critical state in Nb thin films*, MFF–UK KFNT seminar in WDS'07 (2007).

[9] **A. Youssef**, *Critical state in Nb thin films*, MFF–UK KFNT seminar (2007).

[10] **A. Youssef**, *Critical state in superconductors*, MFF–UK KFNT seminar in Pec pod Sněžkou (2008).

* This article was selected for the October 1, 2009 issue of the Virtual Journal of Applications of Superconductivity. This Virtual Journal is published by the American Institute of Physics and the American Physical Society in cooperation with numerous other societies and publishers, covering a focused area of frontier research.

[11] **A. Youssef** and Z. Janů, *Study of noise in higher harmonics of AC magnetization on basis of critical state model in Nb thin films*, Mansoura University, seminar in Sharm –Elsheikh, Egypt (2008).

[12] **A. Youssef**, *Critical state in superconductors*, MFF–UK KFNT seminar in Pec pod Sněžkou (2009).

[13] **A. Youssef**, *Critical state in superconductors*, MFF–UK KFNT seminar (2010).